AFRL-AFOSR-VA-TR-2024-0153

Light Curve Inversion for Characterization of Objects with Concavities

Frueh, Carolin
PURDUE UNIVERSITY
2550 NORTHWESTERN AVE # 1100
WEST LAFAYETTE, IN, 47906
USA

02/13/2024
Final Technical Report

Air Force Research Laboratory
Air Force Office of Scientific Research
Arlington, Virginia 22203
Air Force Materiel Command

REPORT DOCUMENTATION PAGE

PLEASE DO NOT RETURN YOUR FORM TO THE ABOVE ORGANIZATION.

1. REPORT DATE	2. REPORT TYPE	3. DATES COVERED	
20240213	Final	START DATE 20180215	END DATE 20230214

4. TITLE AND SUBTITLE
Light Curve Inversion for Characterization of Objects with Concavities

5a. CONTRACT NUMBER	5b. GRANT NUMBER	5c. PROGRAM ELEMENT NUMBER
	FA9550-18-1-0154	61102F
5d. PROJECT NUMBER	**5e. TASK NUMBER**	**5f. WORK UNIT NUMBER**

6. AUTHOR(S)
Carolin Frueh

7. PERFORMING ORGANIZATION NAME(S) AND ADDRESS(ES)
PURDUE UNIVERSITY
2550 NORTHWESTERN AVE # 1100
WEST LAFAYETTE, IN 47906
USA

8. PERFORMING ORGANIZATION REPORT NUMBER

9. SPONSORING/MONITORING AGENCY NAME(S) AND ADDRESS(ES)	10. SPONSOR/MONITOR'S ACRONYM(S)	11. SPONSOR/MONITOR'S REPORT NUMBER(S)
Air Force Office of Scientific Research 875 N. Randolph St. Room 3112 Arlington, VA 22203	AFRL/AFOSR RTB1	AFRL-AFOSR-VA-TR-2024-0153

12. DISTRIBUTION/AVAILABILITY STATEMENT
A Distribution Unlimited: PB Public Release

13. SUPPLEMENTARY NOTES

14. ABSTRACT
In this contract, we explored new techniques for the light curve inversion for shape. In the course of the contract, two techniques were fully developed and led to successful results. Light curve inversion using the Extended Gaussian Image has been significantly extended to be fast and reliable for shape inversion in the presence of noise. Here, the work of Dr. Oliker was further developed. A new technique has been developed to invert light curves and find objects with a concavity. It is the first of its kind to find shapes with concavities. Independent of this first inversion approach, compressed sensing has been explored for inversion, not creating 3D shape models but resolved images from the light curve. It is also the first technique to explore light curve inversion under this approach.

15. SUBJECT TERMS

16. SECURITY CLASSIFICATION OF:			17. LIMITATION OF ABSTRACT	18. NUMBER OF PAGES
a. REPORT U	b. ABSTRACT U	c. THIS PAGE U	UU	88

19a. NAME OF RESPONSIBLE PERSON	19b. PHONE NUMBER *(Include area code)*
MICHAEL YAKES	00000000

Standard Form 298 (Rev.5/2020)
Prescribed by ANSI Std. Z39.18

Light Curve Inversion For Characterization Of Objects With Concavities

Dr. Carolin Frueh (PI), Dr. Vladimir Oliker (consultant)

AFOSR FA9550-18-1-0154
Final Report

Abstract

In this contract, we explored new techniques for the light curve inversion for shape. In the course of the contract, two techniques were fully developed and led to successful results. Light curve inversion using the Extended Gaussian Image has been significantly extended to be fast and reliable for shape inversion in the presence of noise. Here, the work of Dr. Oliker was further developed. A new technique has been developed to invert light curves and find objects with a concavity. It is the first of its kind to find shapes with concavities. Independent of this first inversion approach, compressed sensing has been explored for inversion, not creating 3D shape models but resolved images from the light curve. It is also the first technique to explore light curve inversion under this approach.

1 Section 1: Structured Survey Questions

1.1 Award Information

You will be asked for the following information in the survey. The majority of these fields will be sent pre-populated but can be edited if necessary. You will be able to manually edit any of these fields if information needs to be updated.

- Award Number (Federal Award Identification Number: AFOSR FA9550-18-1-0154)
- Report Type: Final Report
- Principal Investigator: Carolin Frueh
- Principal Investigator Email: cfrueh@purdue.edu

- Principal Investigator Phone: (765) 494-7436
- Project Title: Light Curve Inversion For Characterization Of Objects With Concavities
- Recipient Organization: Purdue University
- Business Office Email: spscontr@purdue.edu
- Report Due Date: 5/14/2023
- Report Period Start Date: Feb 15, 2018
- Report Period End Date: Feb 14, 2023
- Current Program Officer: Michael Yakes

1.2 Publications

V. Oliker, C. Frueh, Similarity of Convex Polyhedra for the Application of Space Object Noisy Light Curve Inversion, Journal of Celestial Mechanics and Dynamics, to be submitted Feb. 2024

D. Kobayashi, C. Frueh, Image Recovery of LEO Objects by Leveraging Optical Turbulence and Light Curves, Journal of Guidance, Control, and Dynamics, accepted 2023

S. Fan, C. Frueh, A Direct Light Curve Inversion Scheme in the Presence of Measurement Noise, Journal of Astronautical Science, doi:10.1007/s40295-019-00190-3, Aug 2019

A. Buzzoni, D. Koschny, G. Drolshagen, E. Perozzi, O. Hainaut, S. Lemmens, G. Altavilla, I. Foppiani, J. Nomen, N. Sánchez-Ortiz, W. Marinello, G. Pizzetti, A. Soffiantini, S. Fan, C. Frueh, The observing campaign on the deep-space debris WT1190F as a test case for short-warning NEO impacts, Icarus, Vol. 304, pp. 4-8, doi:10.1016/j.icarus.2017.10.006, Jul 2018

A. Buzzoni, G. Altavilla, S. Fan, I.Froppiani, C. Frueh, M. Micheli, J. Nomen, N. Sanchez Ortiz, Physical characterization of the deep-space debris WT1190F: a testbed for advanced SSA techniques, Advances in Space Research, Vol. 63, Issue 1, pp. 371-393, doi:10.1016/j.asr.2018.07.025, Jan 2019

D. Kobayashi, C. Frueh, Sparse Decoding for Resolving LEO Objects, Second International Conference on Orbital Debris, Houston, TX, Dec 2023

D. Kobayashi, C. Frueh, Reformulating Compressed Sensing to be used with Semi-Resolved Point Spread Function and Light Curves for Space Object Imaging: LEO, The Advanced Maui Optical and Space Surveillance Technologies (AMOS) Conference, Sep. 2022

L. Robinson, C. Frueh, Light Curve Inversion for Reliable Shape-Reconstruction of Human-Made Space Objects, AAS/AIAA Astrodynamics Specialist Conference, Charlotte, North Carolina, Aug. 2022

C. Frueh, V. Oliker, Quantifying the Effect of Uncertainty in the Brightness Measurements of a Light Curve on the Shape Inversion Diversity, AAS/AIAA Astrodynamics Specialist Conference, Charlotte, North Carolina, Aug. 2022

S. Fan, C. Frueh, Multi-Hypothesis Light Curve Inversion Scheme for Convex Objects with Minimal Observations, 8th European Conference on Space Debris, April 2021

S. Fan, A. Friedman, C. Frueh, Satellite Shape Recovery from Light Curves with Noise, Advanced Maui Optical and Space Surveillance Conference, Maui, Sep. 2019

S. Fan, C. Frueh, A Light Curve Inversion Scheme for Artificial Objects, AAS/AIAA Astrodynamics Specialist Conference, AAS-18-441, Snowbird, UT, Aug 2018

Daigo Kobayashi, Compressed Sensing for Satellite Characterization: Exhaustive Research in LEO and Higher Orbits, to be completed 2024

Liam Robinson, MS thesis, Light Curve Simulation And Shape Inversion For Human-Made Space Objects, School of Aeronautics and Astronautics, Purdue University, 2023 (about 50% of the thesis pertains to this contract)

Siwei Fan, The Light Curve Simulation and Its Inversion Problem for Human-Made Space Objects, 2020

1.3 Participants

You will be asked to provide the information below for: (1) PIs; and (2) each person who worked on and was funded by this grant during the current reporting period. Please

include all participants, including yourself.

- Carolin Frueh, PI
  - ORCID: 0000-0002-0240-5509
  - Project lead
  - Vladimir Oliker, Consultant
    - ORCID: 0000-0003-1352-6979
    - Project consultant on inversion mathematics
- Siwei Fan
  - PhD student, development of light curve inversion with noise, further development of Oliker's measure.
- Liam Robinson
  - PhD student, formerly MS student. Development of the inversion with a concavity.
- Daigo Kobayashi
  - PhD student, formerly MS student. Development of the compressed sensing approach.

2 Section 2: Technical Report

2.1 Accomplishments

Principal Discipline: Within the contract, several significant advances have been made in the principal discipline. For one, the method of light curve inversion for shape in the presence of attitude knowledge has been expanded. While using the Extended Gaussian image followed by using Minkowski closure has been established before, the method has been significantly expanded for using human-made satellites. With the flexible grouping and stronger convergence, no hard cut-off threshold values have to be selected anymore.

Secondly, a method has been developed for explicitly handling noisy data. Inspired by Dr. Oliker's geometric measure a way has been found to select the best shape from a variety of possible shapes within the noise, an equivalent to a mean shape. This extension allows the application of light curve inversion to realistic satellite light curves.

Thirdly, a first method has been involved for a shape inversion involving a concavity. Most human-made objects are not or not fully convex. Hence, previous methods were always limited in that sense. Within the contract, we made a huge step in being able to resolve the most significant concavity. However, further theoretical developments are needed to resolve multiple concavities. A limitation of all shape inversion is currently the assumption of perfect attitude knowledge and a uniform albedo of the object. Those should be the next steps in the further development of the light curve shape inversion.

Complementary to and independent of the shape inversion, a new method has been explored as part of this contract. In this approach, the light curve of a stabilized satellite is collected. Instead of aiming to invert for a three-dimensional shape, in this alternative approach, a resolved two-dimensional image of the object is sought. The method leverages compressed sensing as known from the JPEG format, for example. It was the first time that compressed sensing techniques were adapted for the light curve inversion problem. We needed to change the original compressed sensing method leveraging the Danzig selector in order to address the non-RIP distributed problem at hand. We could show that the atmospheric turbulence can be interpreted as a compressor. We showed that the method is theoretically feasible when wavefront sensing is available. The next step is the test with real data. A limitation of the method is that it is currently restricted to stabilized satellites; extensions can be made for non-stabilized ones. Furthermore, using the atmosphere as the compressor requires the satellites to be a low-Earth satellite. However, there are no restrictions on the actual camera optics, so a small-sized instrument is more than fine. For the compressed sensing light curve method to be feasible for high-altitude satellites, a different compressor has to be identified. It is the thrust of our next research steps. As part of this research, we have developed a wave-optics fully physics-based simulation pipeline.

Adjacent Disciplines: As by-products, Dr. Oliker's research led to a geometric measure of similarities of convex polytopes, which has the potential to be relevant to a wider range of disciplines.

The generalizability of the compressed sensing approach can be viewed as exemplary of adaptions of compressed sensing in very different fields.

Dissemination Dissemination took place through journal publications, conference presentations, and proceeding papers. Invited Keynote speaker at the 3rd IAA Conference on Space Situational Awareness, Apr. 4-6, 2022, Tres Cantos, Madrid, 2022. Outreach at the West Lafayette High School and the West Lafayette Astronomy Club.

2.2 Impacts

The research has overall impacted the view of light curve inversion in the community. For a while, it has been viewed as a dead topic, and I think it is fair to say that my research has contributed to spark new interest and confidence in the solvability of the problem. The first steps towards commercialization have been made with company partners Katalyst and Comspoc.

The research into compressed sensing has sparked a lot of attention. Together with MacGraw and Associates, the real-world applicability of the method is further explored.

We have been able to utilize our early results already to help identify the object WT1109F in an international attempt in 2018.

2.3 Changes

Beyond the original scope of the project, the line of research into compressed sensing was added to the original proposal. Some of the results provided by Dr. Oliker have been proven to be computationally expensive and have, in parts, been replaced by different, more computationally feasible methods offering the same or equally desirable results.

Technical Details and Showing off the Exciting Results

In the following, we want to showcase the exciting technical results obtained as part of this contract. First, the most recent journal publication on compressed sensing is attached.

The journal publication on shape inversion, including noise, is shown for the light curve inversion, followed by the latest extension on the noisy inversion approach. Furthermore, the paper outlining the improved inversion and inversion for objects with concavities is shown.

Image Recovery of LEO Objects by Leveraging Optical Turbulence and Light Curves

Daigo Kobayashi * and Carolin Frueh †
Purdue University, West Lafayette, Indiana 47906

This paper shows a novel method to characterize human-made objects in low Earth orbit (LEO) using compressed sensing on light curve measurements. The proposed approach minimizes total variation to recover a resolved object image from a fully-unresolved light curve and a so-called point spread function (PSF) map. The light curves are generated through numerical wave propagation, which considers atmospheric turbulence under anisoplanatic conditions. Subsequently, the light curve model is transformed into a linear measurement model to apply compressed sensing techniques. Notably, the sensing matrix is found to be a superposition of spatially variable PSFs, which significantly downsamples the ideal object image. The proposed approach robustly recovers clear images of objects in LEO, even with imperfect PSF map estimates and Poisson noise in the light curve measurement.

Nomenclature

a	=	circular aperture mask of a telescope
C_n^2	=	refractive index structure function, $\mathrm{m}^{-2/3}$
$C_{n_i}^2$	=	refractive index structure function of the i-th phase screen, $\mathrm{m}^{-2/3}$
$c_{n,m}$	=	Fourier coefficients of phase screen, rad
D	=	diameter of aperture mask, m
$\mathcal{F}, \mathcal{F}^{-1}$	=	Fourier transform operator and its inverse
$f_x,\ f_y$	=	X and Y components of spatial frequency, m^{-1}
g	=	gain of a sensor, e^{-1}/ADU
H	=	optical transfer function of a composite of free space and turbulence
H_{dif}	=	optical transfer function of free space
H_{atm}	=	optical transfer function of turbulence
h	=	point spread function
$h_{\Delta z_i}$	=	impulse response function of the free space

*Corresponding author, Research assistant, School of Aeronautics and Astronautics, dkobayas@purdue.edu
†Associate Professor, School of Aeronautics and Astronautics, cfrueh@purdue.edu

I_{Sun}	=	intensity of the Sun at 1 AU, Wm^{-2}
j	=	imaginary unit
K	=	number of nonzero pixels in a sparse coefficient vector
k	=	wave number
L	=	total propagation distance, km
$L_{\text{free}}, L_{\text{turb}}$	=	propagation distance through free space and turbulence, km
ℓ	=	effective focal length of a telescope, m
ℓ_0, L_0	=	inner and outer scale, m
m	=	length of a compressed image vector, pixels
mag_{Sun}	=	visual magnitude of Sun
N	=	side length of a local phase screen, pixels
N_{ext}	=	side length of an extended phase screen, pixels
$\mathcal{N}$	=	number of extended phase screens
n	=	length of an image vector, pixels
o	=	ideal object image
r_0	=	coherence diameter, m
r_{0_i}	=	coherence diameter of the i-th phase screen, m
t	=	time, s
u	=	complex amplitude of optical wave, $\sqrt{Wm^{-2}}$
$\mathbf{X}$	=	square matrix obtained by reshaping an image vector
$\mathbf{x}$	=	image in the form of a column vector
$\mathbf{y}$	=	compressed image in the form of a column vector
$x,\ y$	=	X and Y coordinates of a point in optical wave, m
y_j	=	j-th entry of a compressed image
z	=	turbulence-degraded image
α	=	switch parameter for the atmosephric optical transfer function
$\boldsymbol{\gamma}$	=	sparse coefficient vector of an image
Δz	=	propagation step in turbulence simulation, km
δ	=	Nyquist grid spacing of phase screen, m
δ_f	=	Nyquist grid spacing on focal plane, m
δ_{PSF}	=	Nyquist grid spacing of point spread function, m
δ_{sensor}	=	pixel pitch of a sensor, m

θ_0	=	isoplanatic angle, μrad
λ	=	wavelength, m
μ, ν	=	X and Y coordinates on focal plane, m
ρ	=	radial frequency coordinates, m^{-1}
ρ_c	=	cut-off frequency
σ_χ^2	=	log-amplitude variance
$\mathbf{\Phi}$	=	sensing matrix
$\mathbf{\Phi}_j$	=	square matrix obtained by reshaping the j-th row of a sensing matrix
$\boldsymbol{\phi}_j^T$	=	row of a sensing matrix
ϕ, ϕ_H, ϕ_L	=	phase screen and its high and low-frequency components, rad
$\mathbf{\Psi}$	=	dictionary

I. Introduction

Space surveillance is becoming increasingly important as the space environment becomes more crowded. The goal of space surveillance is to detect, track, and identify space objects to predict their orbits and to support future space missions, such as Active Debris Removal (ADR). Ground-based observations can provide astrometric observations allowing for orbit determination. However, due to non-conservative orbital perturbation forces, more accurate long-term orbit prediction requires a deeper understanding of the object's characteristics, such as its shape, rotation, and surface properties. One such characterization method is to analyze a light curve, time series of the brightness measurements, to obtain information beyond the center of mass.

Early studies of light curve inversion [1, 2] have focused on the shape and attitude inversion of asteroids. Most asteroids have a convex shape and uniform reflectivity, allowing researchers to recover the Extended Gaussian Image (EGI) from the light curve and invert the shape by solving the Minkowski problem. In addition, many asteroids have a single rotation axis, simplifying the attitude inversion problem.

In contrast, light curve inversion for artificial space objects presents a more challenging problem. Many assumptions about asteroids do not hold for these objects: they often have nonconvex shapes and nonuniform reflectivity, resulting in non-unique and high-dimensional solutions. Many studies have addressed this issue by making assumptions about the attitude or albedo shape to reduce the number of unknown states. Yanagisawa and Kurosaki [3] estimated the shape and motion of a Cosmos rocket body by fitting an ellipsoid model. Linares et al. [4, 5] used filtering methods for shape and attitude inversion while assuming a simple spin or simple shape. Linares and Crassidis [6] solved shape and attitude inversion using a Markov Chain model while assuming a simple shape. Fan and Frueh [7, 8] developed a multi-hypothesis scheme to rank candidate solutions for shapes. Robinson and Frueh [9] augmented EGI-based methods

by embedding a concavity creation algorithm. In recent years, several studies have utilized deep learning techniques for shape characterization [10–15]. Still, most of these studies do not explicitly recover the object shape, instead classifying it into several predefined classes. All of these approaches reconstructed a three-dimensional state and are plagued by the inherent ambiguity of the system and the curse of dimensionality. As an alternative, this study explores the option of reconstructing a two-dimensional image with a frozen attitude state using compressed sensing.

Compressed sensing (CS) [16–18] is a signal compression technique that significantly reduces sampling rates well below the limit of the Nyquist-Shannon theorem [19]. A high-dimensional signal is mapped to a lower-dimensional signal using a sensing matrix. The sensing matrix must satisfy the Restricted Isometry Property (RIP) and is typically designed with random entries. If the signal is sparse in a particular basis, the signal can be reconstructed by seeking the sparsest solution that explains the compressed signal.

Previous studies investigated the use of compressed sensing in reconstructing the two-dimensional geometry of an unknown space object. A preliminary study [20] discovered and provided the mathematical framework to exploit a similarity between CS-based image compression and light curve measurement under the influence of atmospheric turbulence. An image of an unknown space object was recovered with a simplified light curve model. A subsequent study [21] developed a more comprehensive physics-based model of the light curve. The atmospheric degradation of the light curve is modeled using point spread functions (PSFs) of the atmospheric turbulence. The modified light curve model resulted in a poor RIP condition of the sensing matrix, necessitating the modification of the recovery algorithm.

This study investigates the impact of noise in the light curve and point spread function (PSF) on image reconstruction. The PSF is degraded by adding white noise to model the estimation error. The light curve is degraded by Poisson noise to model the shot noise inherent to optical measurements. The combination of Poisson noise in the light curve and Gaussian noise in the PSF map makes image recovery more challenging. However, this study uses total variation (TV) minimization with a Dantzig selector constraint for robust image reconstruction. The image recovery performance is tested for various object brightness levels and Gaussian noise levels in the PSF map.

II. Compressed Sensing

A. Theory

The mathematical framework of compressed sensing (CS) is shown here in abbreviated form as relevant to the methods employed in this paper. CS works by jointly compressing and sampling a high-dimensional image $\mathbf{x} \in \mathbb{R}^n$ through a linear operation given by [16]:

$$\mathbf{y} = \mathbf{\Phi x}, \tag{1}$$

where $\mathbf{y} \in \mathbb{R}^m$ ($m \ll n$) is a compressed signal vector, and $\mathbf{\Phi} \in \mathbb{R}^{m \times n}$ is a so-called sensing matrix. Since the number of measurements is significantly smaller than the number of pixels in the image, the system in Eq.(1) is underdetermined.

However, the signal can be accurately recovered by considering the sparsity of the image of interest. Most signals possess a sparse representation, given by $\mathbf{x} = \mathbf{\Psi}\boldsymbol{\gamma}$, where a coefficient vector, $\boldsymbol{\gamma}$, has only $K(\ll n)$ nonzero pixels. The matrix $\mathbf{\Psi} \in \mathbb{R}^{n \times n}$ is called a dictionary, and its columns work as bases of the image $\mathbf{x}$. Popular choices for the dictionary in image compression includes a discrete cosine transform (DCT) matrix, a Gaussian matrix, and a Fourier transform matrix. This sparse representation provides an alternative formulation for the compressed image, as given by $\mathbf{y} = \mathbf{\Phi}\mathbf{\Psi}\boldsymbol{\gamma}$, and the sparse vector is recovered by seeking the sparsest solution that explains the compressed image [16–18], as given by:

$$\hat{\boldsymbol{\gamma}} = \arg\min_{\boldsymbol{\gamma}} \|\boldsymbol{\gamma}\|_1 \quad \text{subject to} \quad \|\mathbf{y} - \mathbf{\Phi}\mathbf{\Psi}\boldsymbol{\gamma}\|_2 \leq \varepsilon, \tag{2}$$

where $\mathbf{\Phi}\mathbf{\Psi}$ is called the equivalent dictionary. The high-dimensional image is recovered by multiplying the dictionary with the sparsest solution: $\hat{\mathbf{x}} = \mathbf{\Psi}\hat{\boldsymbol{\gamma}}$.

To obtain an accurate solution for Eq.(2), the equivalent dictionary is selected or designed to satisfy the Restricted Isometry Property (RIP) [22]. In essence, the RIP condition requires that the equivalent dictionary preserves meaningful information in any k-sparse vectors, thus enabling accurate reconstruction of the image $\mathbf{x}$. While confirming whether a general matrix satisfies the RIP condition is NP hard [23], most random matrices, such as a Gaussian matrix and Bernoulli random matrix, satisfy the RIP condition [24].

B. Single-Pixel Camera

In CS, a scalar entry y_j of the measurement vector is computed as the inner product between a row of the sensing matrix $\boldsymbol{\phi}_j^T$ and the image vector $\mathbf{x}$. By reshaping the vectors $\boldsymbol{\phi}_j^T$ and $\mathbf{x}$ into matrices: $\mathbf{\Phi}_j$ and $\mathbf{X}$, respectively, each entry

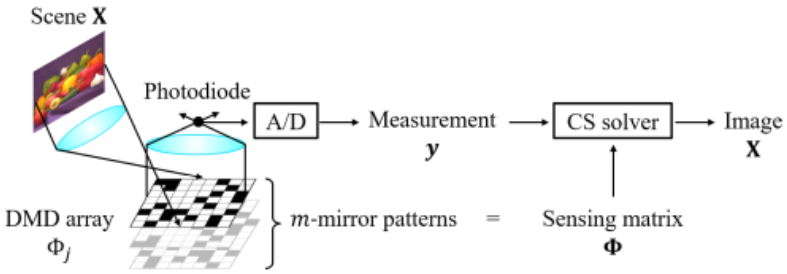

Fig. 1 Schematic of single-pixel camera

y_j can be computed as the element-wise product between these matrices [20]:

$$y_j = \boldsymbol{\phi}_j^T \mathbf{x} = \sum \boldsymbol{\Phi}_j \odot \mathbf{X}. \tag{3}$$

This idea is utilized in a single-pixel camera [25], where a scene is focused on a digital micromirror device (DMD) by a convex lens, and a photodiode collects the reflected light, as illustrated in Figure 1. The DMD works as a binary alternative of the sensing matrix, and by repeating the measurement m times with different mirror patterns in the DMD, the original scene can be reconstructed by a CS solver using the measurement vector $\mathbf{y}$. Thus, the single-pixel camera is capable of imaging a scene with only a single photodiode.

C. Analogy to Light Curve

In previous work [20], a qualitative and quantitative comparison was performed between a single-pixel camera and light curve measurement. A schematic diagram to illustrate the comparison is shown in Figure 2.

In the single-pixel camera, as depicted in Figure 2 (a), the pixel values of the scene are projected onto a DMD mirror pattern and randomly masked. Subsequently, the masked scene is focused by a positive lens on a photodiode, which measures the total brightness.

In contrast, light curve measurement, illustrated in Figure 2 (b), entails the reflection of sunlight from each point on a space object, followed by the propagation of light beams through atmospheric turbulence, leading to their attenuation. This random attenuation may be considered analogous to the random masking of image entries in the single-pixel camera. These attenuated light beams are then captured by a telescope and are recorded as an intensity of the light curve, which mirrors the summation of masked image entries.

Based on this analogy, this research leverages compressed sensing to recover a resolved image of an unknown space object based on its light curve measurement. The attenuation of the light curve due to atmospheric interference is computed using point spread functions (PSFs) computed by a rigorous wave propagation model through atmospheric turbulence. More details about the light propagation method can be found in Section III.

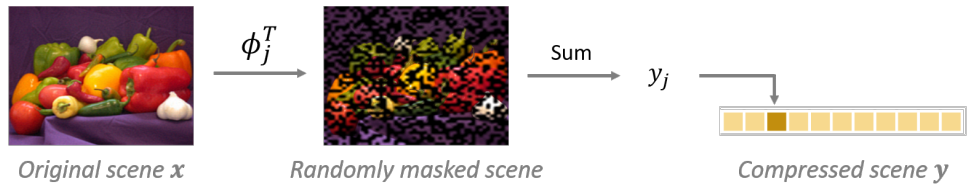

(a) Single-pixel camera measurement

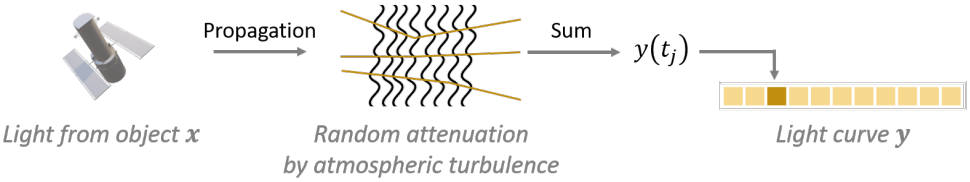

(b) Light curve measurement

Fig. 2 Comparison of single-pixel camera and light curve measurement

III. Light Propagation Modeling

A. Overview

The light curve measurements are simulated to fully explore the capabilities of the proposed method. This technique has the advantage of providing access to ground truth in evaluating the method. The light curve simulation method is purposely physics-based to be as representative of the real observations as possible.

Specifically, this research adopts an anisoplanatic imaging simulation method to model wave propagation through free space and turbulence for a low Earth orbit (LEO) object located at 550 km. The proposed method extends the framework developed by Hardie et al. [26], which has been validated for horizontal paths of short distances (up to 7 km).

First, a spherical wave is emitted from every point on the object plane and propagated over a distance L_{free} through the atmosphere-free space. The simplicity of the medium allows the propagated wave to be analytically computed via the Fresnel diffraction integral [27, Ch.6].

The optical wave is then propagated through the atmospheric turbulence from the upper atmosphere to the ground. First, the random phase fluctuations caused by the turbulence are modeled using a set of $\mathcal{N}$ extended phase screens, which are equally spaced over a distance, L_{turb}. The extended phase screens are then cropped to create local phase screens of size $N \times N$ ($< N_{\text{ext}}$) within a predetermined distance of the optical path from each point on the object. This two-step procedure is employed to model the spatial correlation of the local turbulence. Figure 3 shows the extended phase screens and two sets of local phase screens depicted as blue and green squares.

The propagated wave is then used to compute a PSF for each point on the object. Ideally, the PSFs are calculated for all pixels on the object plane, but the PSFs are instead calculated at sample points spaced by small pixel values on the object plane to save computational time. The PSF values at non-sample points are calculated using bilinear

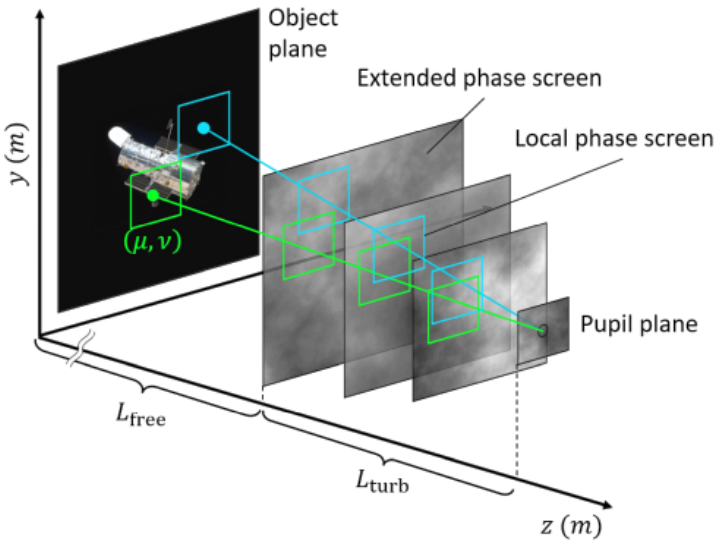

Fig. 3 Geometry of the optical wave propagation of a LEO object.

interpolation, which preserves the spatial correlation of the atmospheric turbulence.

After calculating the spatially-varying PSFs, the degraded image of the object is calculated as a spatially weighted average of the true object. This degraded image represents the theoretical image measured on a PSF sensor, which may or may not be the same as the ground-based telescope used for imaging. The ground-based sensor is assumed to have an aperture and resolution, resulting in a degraded, noise-affected light curve formed by an entirely unresolved image. The degraded light curve is calculated as the pixel summation of the degraded image. Therefore, the light curve measurement is a linear mapping of the true object due to the linearity of the spatially weighted average calculation. This linear light curve model is interpreted as a linearly compressed image in compressed sensing with a sensing matrix whose row represents the superposition of the PSFs.

More details are described in the following subsections. In Section III.B and III.C, the theories and procedures to generate the extended phase screens are explained. In Section III.D, a spherical wave is propagated through the phase screens to compute its complex amplitude at the pupil plane. In Section III.E, the method to compute PSF is detailed. In Section III.F, the method to compute degraded image and light curve are explained. In Section III.G, the degraded image model is adapted to the compressed image model in compressed sensing. Finally, in Section III.H, noise in the PSF map and light curve is modeled.

B. Coherence Diameter of Each Phase Screen

The extended phase screens are computed by Fourier Transform (FT) method [28] based on the implementations by Schmidt [27, Ch.9].

First, the refractive index structure function $C_n^2(z)$ is chosen to characterize the atmospheric transparency over

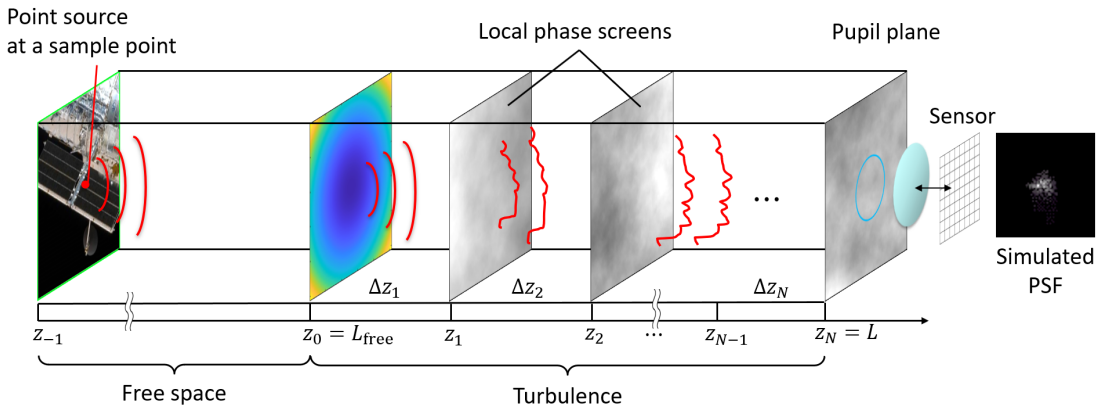

Fig. 4 Split-step propagation of a spherical wave from a sample point of an object.

distance z from the space object to the observer. The $C_n^2(z)$ function may be estimated by a number of methods including a numerical weather prediction simulations [29], empirical models [30], and measurement-based methods [31]. In this study, the $C_n^2(z)$ function is simplified as zero in free space over $0 \le z < L_{\text{free}}$ and modeled as a positive constant C_n^2 over turbulence located at $L_{\text{free}} \le z \le L$ $(= L_{\text{free}} + L_{\text{turb}})$ because the atmosphere contributes to refraction only up to a certain altitude [30].

Subsequently, three statistical measures of the turbulence strength: the coherence diameter r_0, isoplanatic angle θ_0, and log-amplitude variance σ_χ^2, are computed by integrating the $C_n^2(z)$ function multiplied by some weight functions:

$$r_0 = \left[0.423k^2 \int_0^L C_n^2(z) \left(\frac{z}{L}\right)^{5/3} \mathrm{d}z\right]^{-3/5} \tag{4}$$

$$\theta_0 = \left[2.91k^2 L^{5/3} \int_0^L C_n^2(z) \left(1 - \frac{z}{L}\right)^{5/3} \mathrm{d}z\right]^{-3/5} \tag{5}$$

$$\sigma_\chi^2 = 0.563k^{7/6} L^{5/6} \int_0^L C_n^2(z) \left(\frac{z}{L}\right)^{5/6} \left(1 - \frac{z}{L}\right)^{5/6} \mathrm{d}z \tag{6}$$

where $k = 2\pi/\lambda$ is the wavenumber, λ is the wavelength, and L is the propagation distance. The coherence diameter r_0 is introduced by Fried [32] and is a diameter for which the turbulence starts to seriously distort the optical field. The isoplanatic angle θ_0 is an angular separation with which two point sources will have approximately the same point spread function (PSF). Finally, the log-amplitude variance σ_χ^2 is a measure that is related to the fluctuation of optical wave amplitude.

The next step is to discretize the turbulence volume into $\mathcal{N}$ phase screens that are equidistant over distance L_{turb}. The position of the i-th phase screen is denoted by $z = z_i$ for $i = 1, ..., \mathcal{N}$ as shown in Figure 4. Each phase screen represents the turbulence-induced phase disturbance at each position. The number of phase screens are set larger than the minimum value that avoids the aliasing problem, based on the conditions in [27, Ch.8]. To compute the phase

screens, the coherence diameters of the local turbulence, r_{0_i}, are computed such that as a whole, they still satisfy the statistics in Eq.(4) - (6). Using the r_{0_i} value, each phase screen is simulated by Monte Carlo method based on the modified von Karman statistics. More details are explained below.

The local coherence diameter, z_{0_i}, is defined to approximate Eq.(4) by its discrete counterpart:

$$\hat{r}_i = \left[\sum_{i=1}^{\mathcal{N}} \left(\frac{z_i}{L} \right)^{5/3} \left(r_{0_i} \right)^{-5/3} \right]^{-3/5} \tag{7}$$

which is obtained by eliminating C_n^2 term by introducing a definition of the coherence diamter of the i-th phase screen:

$$r_{0_i} = \left[0.423 k^2 C_{n_i}^2 \Delta z_i \right]^{-3/5} \tag{8}$$

Solving Eq.(8) in terms of $C_{n_i}^2$ and substituting in the discrete versions of Eq.(5) and (6), the isoplanatic angle and log-amplitude variance are also expressed as in terms of r_{0_i}:

$$\hat{\theta}_0 = \left[6.8794 L^{5/3} \sum_{i=1}^{\mathcal{N}} \left(1 - \frac{z_i}{L} \right)^{5/3} \left(r_{0_i} \right)^{-5/3} \right]^{-3/5} \tag{9}$$

$$\hat{\sigma}_\chi^2 = 1.331 \left(\frac{L}{k} \right)^{5/6} \sum_{i=1}^{\mathcal{N}} \left(\frac{z_i}{L} \right)^{5/6} \left(1 - \frac{z_i}{L} \right)^{5/6} \left(r_{0_i} \right)^{-5/3} \tag{10}$$

Equating Eqs.(7), (9), and (10) gives a linear matrix equation as below:

$$\underbrace{\begin{bmatrix} (\hat{r}_0)^{-5/3} \\ \frac{\hat{\sigma}_\chi^2}{1.331 k^{-5/6} L^{5/6}} \\ \frac{(\hat{\theta}_0)^{-5/3}}{6.8794 L^{5/3}} \end{bmatrix}}_{\hat{\mathbf{b}}} = \underbrace{\begin{bmatrix} \left(\frac{z_1}{L} \right)^{5/3} & \left(\frac{z_2}{L} \right)^{5/3} & \cdots & \left(\frac{z_\mathcal{N}}{L} \right)^{5/3} \\ \left(\frac{z_1}{L} \right)^{5/6} \left(1 - \frac{z_1}{L} \right)^{5/6} & \left(\frac{z_2}{L} \right)^{5/6} \left(1 - \frac{z_2}{L} \right)^{5/6} & \cdots & \left(\frac{z_\mathcal{N}}{L} \right)^{5/6} \left(1 - \frac{z_\mathcal{N}}{L} \right)^{5/6} \\ \left(1 - \frac{z_1}{L} \right)^{5/3} & \left(1 - \frac{z_2}{L} \right)^{5/3} & \cdots & \left(1 - \frac{z_\mathcal{N}}{L} \right)^{5/3} \end{bmatrix}}_{\mathbf{A}} \underbrace{\begin{bmatrix} r_{0_1}^{-5/3} \\ \vdots \\ r_{0_\mathcal{N}}^{-5/3} \end{bmatrix}}_{\mathbf{s}} \tag{11}$$

The vector $\hat{\mathbf{b}}$ and matrix $\mathbf{A}$ in Eq.(11) are already known given the positions of phase screens and the values of $\hat{r}_0$, $\hat{\sigma}_\chi^2$, and $\hat{\theta}_0$ parameters obtained earlier. The coherence diameter of the phase screens can be obtained by solving a constrained least squares problem:

$$\min_{\mathbf{s}} \quad \|\hat{\mathbf{b}} - \mathbf{A}\mathbf{s}\|_2^2 \tag{12a}$$

$$\text{s.t.} \quad 1.331 k^{-5/6} L^{5/6} \left(\frac{z_i}{L} \right)^{5/6} \left(1 - \frac{z_i}{L} \right)^{5/6} \leq 0.2 \hat{\sigma}_\chi^2 \tag{12b}$$

$$0 \leq r_{0_i}, \quad \forall i = 1, \ldots, \mathcal{N} \tag{12c}$$

where two constraints are imposed to ensure the validity of the coherence diameter values, following the Schmidt's method [27, Ch.8]. The first constraint is that the log-amplitude variances of the phase screens must be less than 20% of the value obtained from Eq.(6). The second constraint is that the coherence diameter of the phase screens must be non-negative.

C. Phase Screen Realization

After computing the coherence diameters of phase screens, the extended phase screens are computed by Monte Carlo method. The high-frequency component of the phase screen is written as a Fourier series:

$$\phi_H(x,y) = \sum_{n=-\infty}^{\infty} \sum_{m=-\infty}^{\infty} c_{n,m} \exp\left[j2\pi(f_{x_n}x + f_{y_m}y)\right], \tag{13}$$

where f_{x_n} and f_{y_m} are the spatial frequencies in the x and y directions respectively, and $c_{n,m}$ are the Fourier series coefficients. The Fourier series coefficients $c_{n,m}$ have a Gaussian distribution with a zero mean and a variance given by [27]:

$$\langle |c_{n,m}|^2 \rangle = S_\phi^{mvK}(f_{x_n}, f_{y_m}) \Delta f_{x_n} \Delta f_{y_m}, \tag{14}$$

where $\langle \cdot \rangle$ denotes the ensemble average, and Δf_{x_n} and Δf_{y_m} are the grid pitch sizes in x and y directions in the frequency domain. The term S_ϕ^{mvK} is a modified von Karman phase power spectral density (PSD). The PSD for the i-th phase screen is given by [27]:

$$S_{\phi_i}^{mvK}(\rho) = \frac{0.023 e^{-\rho^2/\rho_m^2}}{r_{0_i}^{5/3}(\rho^2 + \rho_0^2)^{11/6}}, \tag{15}$$

where $\rho = \sqrt{f_x^2 + f_y^2}$ is the radial spatial frequency, and $\rho_m = 5.92/(2\pi\ell_0)$ and $\rho_0 = 1/L_0$ are the coefficients with respect to the outer scale L_0 and the inner scale ℓ_0, respectively. Turbulent eddies are randomly-distributed pockets of air due to the non-uniform velocity distribution. The outer and inner scales are the average sizes of the largest and smallest turbulent eddies.

The low-frequency component of the phase screen is computed by the subharmonic method [33] to improve the fidelity of the phase screens. It is generated as a sum of N_p different screens, given by:

$$\phi_L(x,y) = \sum_{p=1}^{N_p} \sum_{n=-1}^{1} \sum_{m=-1}^{1} c_{n,m} \exp\left[i2\pi(f_{x_n}x + f_{y_m}y)\right] \tag{16}$$

The random draws of the Fourier coefficients are generated at N_p times with different grid spacings of $\Delta f_p = 1/(3^p W)$,

where W is the width of the sampling grid. This sampling allows generating a screen with varieties of frequency components. The final phase screen is a sum of the high and low frequency components:

$$\phi(x, y) = \phi_H(x, y) + \phi_L(x, y) \tag{17}$$

D. Numerical Wave Propagation

The split-step propagation method, as depicted in Fig. 4, is utilized to generate a PSF that corresponds to a single sample point of the object. This method involves the use of a spherical wave and a set of $\mathcal{N}$ local phase screens, which is selected from the extended phase screens based on the geometry depicted in Fig. 3.

This study considers the wave propagation through free space over a distance L_{free} and the subsequent propagation through turbulence of a distance L_{turb}. The point source, u_{pt}, is modeled by a Dirac delta function, and the wave field after free-space propagation is computed using the Fresnel diffraction integral [27, Ch.6]:

$$u_0(x, y) = \frac{e^{jkL_{\text{free}}}}{j\lambda L_{\text{free}}} \int_{-\infty}^{\infty}\int_{-\infty}^{\infty} u_{\text{pt}}(x_{\text{pt}}, y_{\text{pt}}) e^{j\frac{k}{2L_{\text{free}}}\left[(x_{\text{pt}}-x)^2+(y_{\text{pt}}-y)^2\right]} dx_{\text{pt}} dy_{\text{pt}} = \frac{e^{jkL_{\text{free}}}}{j\lambda L_{\text{free}}} e^{j\frac{k}{2L_{\text{free}}}(x^2+y^2)} \tag{18}$$

To model the propagation through turbulence, the wave field is propagated through a series of phase screens and free space, sequentially applying the following equation:

$$u_i(x, y; t) = \left[u_{i-1}(x, y; t) * h_{\Delta z_i}(x, y)\right] e^{j\phi_i(x,y;t)}, \tag{19}$$

for $i = 1, 2, \ldots, \mathcal{N}$. Here, $u_i(x, y; t)$ and $u_{i-1}(x, y : t)$ are the wave fields at the i-th and $(i-1)$-th phase screen respectively. The last term in Eq.(19) corresponds to the phase disturbance where $\phi_i(x, y; t)$ is the turbulence-induced random phase fluctuation that is modeled by the i-the phase screen. It is a function of time t depending on a wind function. The operation $A * B$ represents a 2D convolution of A and B. The term $h_{\Delta z_i}(x, y)$ is the impulse response of free-space propagation for Fresnel diffraction between the $(i-1)$-the and i-the phase screens, which is given by:

$$h_{\Delta z_i}(x, y) = \frac{e^{jk\Delta z_i}}{j\lambda\Delta z_i} e^{j\frac{k}{2\Delta z_i}(x^2+y^2)} \tag{20}$$

Eq.(19) is implemented by angular spectrum method described by Schmidt [27], which utilizes the fast Fourier transform (FFT) to compute the 2D convolution. To optimize the performance of the FFT, the number of discrete sample points of phase screens, N is chosen to be a power of two. The sampling grid spacing of phase screens is determined based on the

critical sampling size proposed by Voelz [34]:

$$\delta = \left(\frac{\lambda L_{\text{turb}}}{N}\right)^{1/2} \tag{21}$$

This grid spacing maximizes the use of bandwidth for Fresnel propagation simulation while avoiding the aliasing problem.

E. Point Spread Function

A PSF, $h(x, y; t)$, is computed based on the complex amplitude at the pupil plane, $u_N(x, y; t)$, obtained above. First, the complex amplitude is multiplied by an aperture mask and an exponential term that models a collimation by telescope. The product is then subjected to Fourier transform, which gives a Fourier spectrum in frequency domain, (f_x, f_y). Finally, the squared magnitude of the spectrum is computed, and it is transformed into a spatial domain by change of variables, $f_x = x/(\lambda\ell)$ and $f_y = y/(\lambda\ell)$.

$$h(x, y; t) = \left| \mathcal{F}\left\{ a(x, y)\, u_N(x, y; t)\, e^{-\frac{j\pi(x^2+y^2)}{\lambda L}} \right\} \right|^2_{f_x = \frac{x}{\lambda\ell}, f_y = \frac{y}{\lambda\ell}} . \tag{22}$$

Here, $\mathcal{F}$ denotes the Fourier transform operation, ℓ is the effective focal length of the PSF sensor, and $a(x, y)$ is the circular aperture mask of diameter D. This result gives a speckle image of PSF measured in extremely short exposure time (i.e., $\sim 10^1$ μs). The simulation is repeated for all the sample points spaced by 2 pixels, which gives a set of 65^2 speckle images of PSFs.

The obtained PSFs serve two purposes in this study. The first usage is for computing a degraded image that would be observed by a sensor at the focal plane, which will be detailed in Section III.F. The PSF works as a kernel that determines the blurriness of the image that would be observed with a large aperture.

The second usage is for testing the validity of the anisoplanatic imaging simulation by comparing the average of the speckle images with the analytical shape of the PSF. First, the numerical value of the average PSF is computed from the speckle images for 100 frames in long- and short-exposure cases. The key distinction between the two exposure times is the correction of the atmospheric tilt effect [27]. If the tilt effect caused by the optical aberrations is not corrected, the resulting PSF will be representative of a long-exposure PSF. Conversely, if the tilt effect is corrected before the summation, the resulting PSF will approximate a short-exposure image. These procedures give a numerical result of average PSF for long and short exposures.

Second, the analytical result of the average PSF is computed. The Fourier spectrum of the PSF, referred to as the optical transfer function (OTF), H, is given by the product of the diffraction-limited OTF, H_{dif}, and the atmospheric

OTF, H_{atm} [35]:

$$H(\rho) = H_{\text{dif}}(\rho) H_{\text{atm}}(\rho), \tag{23}$$

$$H_{\text{dif}}(\rho) = \begin{cases} \frac{2}{\pi}\left[\cos^{-1}\left(\frac{\rho}{\rho_c}\right) - \frac{\rho}{\rho_c}\sqrt{1-\left(\frac{\rho}{\rho_c}\right)^2}\right], & \rho \le \rho_c \\ 0, & \text{otherwise} \end{cases}, \tag{24}$$

$$H_{\text{atm}}(\rho) = \exp\left\{-3.44\left(\frac{\lambda \ell \rho}{r_0}\right)^{5/3}\left[1 - \alpha\left(\frac{\lambda \ell \rho}{D}\right)^{1/3}\right]\right\}. \tag{25}$$

Here, $\rho_c = D/(\lambda\ell)$ is the cut-off frequency of the diffraction-limited OTF. The parameter α is a switch parameter to distinguish between long- and short-exposure cases, with $\alpha = 0$ representing a long-exposure PSF and $\alpha = 1$ representing a short-exposure PSF. Finally, the analytical result of the average PSF is computed by applying the inverse Fourier transform to the computed OTF: $h(x, y) = \mathcal{F}^{-1}\{H(\rho)\}$ and will be compared with the numerical result to validate the anisoplanatic imaging simulation.

F. Image and Light Curve

The pixel value of the image at point (μ, ν) at time t in anisoplanatic imaging is denoted as $z(\mu, \nu; t)$. It is computed by a sum of the object image spatially weighted by PSFs, as opposed to a 2D convolution between a true object image and the PSF in isoplanatic imaging, which is given by:

$$z(\mu, \nu; t) = \sum_k \sum_l o(\mu - k, \nu - l)\; h_{\mu,\nu}(k, l; t), \tag{26}$$

where $o(\mu, \nu)$ is the true object image and $h_{\mu,\nu}(k, l; t)$ is the space-variant PSF associated with the point source at the point (μ, ν) of the true object image at time t.

To accurately compute Eq.(26), it is necessary to adjust the grid spacing of the PSF to match the counterpart of the object model. The smallest pixel pitch size to satisfy the Nyquist-Shannon theorem is referred to as the Nyquist grid spacing. The object, o, is imaged on the PSF detector as a 2D array with a Nyquist grid spacing on the focal plane, δ_f while the PSF obtained from Eq.(22) has a grid spacing, δ_{PSF}. These two grid spacings are given by:

$$\delta_f = \frac{\lambda \ell}{2D},\ \delta_{PSF} = \frac{\lambda \ell}{\delta N}, \tag{27}$$

Since these two values are different, the result of Eq.(22) is resampled to the grid spacing of δ_f prior to the implementation of Eq.(26).

The computed image z is measured on a pixel grid of an optical sensor. In this study, the sensor grid size is assumed to be δ_{sensor} =2.69 μm, approximately the same size as the Nyquist pixel size on the focal plane, δ_f. Thus, it is assumed

that there is no information loss due to the limited resolution of the sensor. The Poisson noise inherent to the image measurement will be addressed in Section III.H. At this stage, it is assumed that the image has been corrected for background noise, which can be readily accomplished in practice.

The light intensity is the brightness of a non-resolved telescope image, corresponding to an image captured using a small aperture. It is computed by summing the pixel values of the image z:

$$y_j = \sum_{\mu} \sum_{\nu} z(\mu, \nu; t_j) \tag{28}$$

which is measured in W/m^2. The light curve is influenced by atmospheric degradation because of z in Eq.(28). By convention [36], the brightness of the light curve is also represented as an apparent magnitude given by:

$$\text{mag} = \text{mag}_{\text{Sun}} - 2.5 \log_{10} \left(\frac{y_j}{I_{\text{Sun}}} \right), \tag{29}$$

where $\text{mag}_{\text{Sun}} = -26.74$ and $I_{\text{Sun}} = 1360.8$ W/m^2 are the magnitude and intensity of the Sun at 1 astronomical unit from the Earth, respectively. A smaller magnitude corresponds to a brighter light curve.

G. Adaptation to Compressed Sensing

The degraded image model in Eq.(26) and the light intensity model in Eq.(28) are adapted for use in compressed sensing. As the spatially-weighted summation in Eq.(26) is a linear operation, a flattened image model $\mathbf{z}(t_j)$ is linear in terms of a flattened object model $\mathbf{x}$, which is given by:

$$\mathbf{z}(t_j) = \left[\mathbf{h}_1(t_j), \ \ldots \ , \mathbf{h}_{65^2}(t_j) \right]^T \mathbf{x}. \tag{30}$$

Here, $\left\{ \mathbf{h}_l(t_j) \right\}_{l=1,\ldots,p^2}$ is formed by shifting the centroid of each PSF sample to the corresponding source location and then flattening the resulting array. The parameter p denotes the number of PSF samples per side. The term "flattening" refers to the process of converting a 2D array into a column vector by slicing it into columns and concatenating them.

As in Eq.(28), the light intensity at time t_j is the sum of the entries in the degraded image, z. The summation of the entries can be achieved by multiplying an all-1's vector, $\mathbf{1}$, with the image model:

$$y_j = \mathbf{1}^T \mathbf{z}(t_j) = \boldsymbol{\phi}_j^T \mathbf{x}. \tag{31}$$

By forming a vector $\boldsymbol{\phi}_j^T$, which is a superposition of all the spatially-variant PSF samples, the light intensity can be written as a linear transformation of the ideal object image, $\mathbf{x}$. In this research, $\boldsymbol{\phi}_j^T$ is referred to as a PSF map, which will be used as a sensing matrix in compressed sensing.

H. Noise in PSF Map and Light Curve

This study analyzes the noise present in the PSF map and the light curve independently.

The PSF map is influenced by estimation noise caused by the imperfection of the PSF determination techniques used, such as those found in the adaptive optics community [37]. The estimation noise of the PSF map is modeled as additive white Gaussian noise with variance σ^2. The noisy PSF map, $\tilde{\boldsymbol{\phi}}_j{}^T$, is given by:

$$\tilde{\boldsymbol{\phi}}_j{}^T = \boldsymbol{\phi}_j^T + \mathbf{v}^T, \quad \text{subject to} \quad \mathbf{v}^T \sim \mathcal{N}(0, \sigma^2) \tag{32}$$

In Section VI, various levels of Gaussian noise is added to the PSF map to evaluate the impact on the image reconstruction.

The light curve is influenced by noise inherent to the measurement process using a CCD or CMOS sensor. The degraded image that accounts for the information loss and the Poisson noise is modeled as $\tilde{z}$, which is given by:

$$\tilde{z}(\mu, \nu; t_j) = \text{Poisson}\left\{\text{uint}\left\{\frac{\pi\,(D/2)^2\,\lambda/(\hbar c)}{g} \cdot z(\mu, \nu; t_j)\right\}\right\}, \tag{33}$$

where $\hbar$ is the Planck constant, c is the speed of light, and g is the gain of the sensor. The operator uint$\{\cdot\}$ converts the intensity of the binned image to an unsigned 32-bit integer value to model the number of bits in the sensor's ADC. The operator Poisson$\{\cdot\}$ generates a Poisson random variable with the value in the bracket as the mean.

The light curve affected by the finite sensor resolution and Poissonian measurement noise is then computed by summing the entries of the image, $\tilde{z}$, and then converting the unit from ADU into W/m^2 by known physical parameters. The resulting noisy light curve model, $\tilde{y}_j$, is given by:

$$\tilde{y}_j = \text{adu\_to\_irr}\left\{\sum_{\mu}\sum_{\nu}\tilde{z}(\mu, \nu; t_j)\right\}, \tag{34}$$

where adu_to_irr is an operator for the unit conversion.

IV. Image Recovery

A. Image Recovery by TV Minimization

Utilizing the light curve measurement and the PSF map obtained from the sensor, the proposed method reconstructs a two-dimensional image by applying the principles of compressed sensing. The light curve model discussed in Section III.G can be written in the form of Eq.(1) by concatenating Eq.(31) for $j = 1, ..., m$. Each row of the sensing matrix corresponds to the PSF map at each time step, t_j for $j = 1, \ldots, m$. In a traditional approach, the image $\mathbf{x}$ can be obtained by solving Eq.(2).

There are two primary challenges associated with directly solving Eq.(2): computational cost and the design of the

sensing matrix.

Firstly, traditional reconstruction methods entail a high computational cost due to the large size of the image vector, which typically exceeds $n > 10^5$. Even for small values of m, determining $\hat{\boldsymbol{\gamma}}$ can be computationally demanding. While fast solvers exist for this problem, they often compromise reconstruction accuracy.

Another challenge lies in the design of the sensing matrix, $\boldsymbol{\Phi}$. As discussed in Section II, the equivalent dictionary must satisfy the RIP condition to accurately reconstruct the image $\mathbf{x}$. However, in LEO imaging, the PSF map, which is solely determined by atmospheric turbulence, serves as the sensing matrix. One of the popular metrics to measure the RIP condition is a mutual coherence [38, Ch.2], which ranges from 0 to 1. Roughly speaking, the smaller value means the better RIP condition. While a popular sensing matrix (e.g. a Gaussian matrix) gives a mutual coherence of around 0.5, the PSF map gives 1.0. Therefore, the PSF map does not satisfy the RIP condition, resulting in inaccurate reconstruction using Eq.(2).

The first challenge is overcome by narrowing the region of interest. The location of the object is estimated using a combination of Airy disk imaging of the light curve and background correction and removal. Hereinafter, the pixel indices of the region of interest is denoted as an ordered sequence of indices $I = (i_1, \ldots, i_k)$. Using this index notation, $\mathbf{M}_I = [\mathbf{m}_{i_1} | \ldots | \mathbf{m}_{i_k}]$ denotes a sub-matrix of $\mathbf{M}$ that consists of the columns indexed by I, in the order in which they appear in I. Similarly, a vector $\mathbf{v}_I = (v_{i_1}, \ldots, v_{i_k})^T$ denotes a sub-vector of $\mathbf{v}$ that includes the elements indexed by I.

The second challenge is overcome by the use of a more robust mathematical formulation, the total variation minimization. The total variation (TV) is a measure of the roughness of the image [39]. It is defined as the sum of gradient of the adjacent pixel values in an image:

$$TV(\mathbf{X}) \triangleq \sum_i \sum_j \sqrt{(X_{i+1,j} - X_{i,j})^2 + (X_{i,j+1} - X_{i,j})^2}. \tag{35}$$

Eq.(1) can be solved by minimizing the TV while regularizing the solution with Dantzig selector constraint [40]:

$$\hat{\mathbf{X}} = \arg\min_{\mathbf{X}} TV(\mathbf{X}) \quad \text{subject to} \quad \|\boldsymbol{\Phi}_I^T(\mathbf{y} - \boldsymbol{\Phi}_I \mathbf{x}_I)\|_\infty \leq \varepsilon. \tag{36}$$

This method uses a fact that the signal to be recovered is a two-dimensional image, as opposed to Eq.(2). The TV minimization promotes the smoothness in the solution by suppressing high frequency intensity variations. Moreover, the Dantzig selector constraint requires that the sparse representation error ($= \mathbf{y} - \boldsymbol{\Phi}_I \mathbf{x}_I$) is not significantly correlated with any of the columns of $\boldsymbol{\Phi}_I$. This constraint encourages the error to be a white noise, leaving no traces of the columns of $\boldsymbol{\Phi}_I$. The problem in Eq.(36) is recast as a second-order cone program (SOCP) and solved with a log-barrier algorithm [41].

B. Image Evaluation

The recovered image is evaluated by an image quality metric called structural similarity (SSIM) index [42], which is defined by

$$SSIM(\hat{X}, X) = l(\hat{X}, X) \cdot c(\hat{X}, X) \cdot s(\hat{X}, X) \tag{37}$$

where $l(\hat{X}, X)$, $c(\hat{X}, X)$, and $s(\hat{X}, X)$ are the luminance, contrast, and structural term:

$$l(\hat{X}, X) = \frac{2\mu_{\hat{X}}\mu_X + C_1}{\mu_{\hat{X}}^2 + \mu_X^2 + C_1}, \quad c(\hat{X}, X) = \frac{2\sigma_{\hat{X}}\sigma_X + C_2}{\sigma_{\hat{X}}^2 + \sigma_X^2 + C_2}, \quad s(\hat{X}, X) = \frac{\sigma_{\hat{X}X} + C_2/2}{\sigma_{\hat{X}}\sigma_X + C_2/2} \tag{38}$$

where $\hat{X}$ is the recovered image, X is the true object image, μ is the mean, and σ is the standard deviation or covariance. C_1 and C_2 are some small constants to avoid singularity. The SSIM matches the human-perceived visual quality and is hence superior to other traditional image quality metrics, such as the mean squared error (MSE) and the peak signal-to-noise ratio (PSNR). The SSIM represents the image quality in the range $(-1, 1]$, where 1 denotes the perfect similarity, 0 denotes no similarity, and -1 denotes the perfect anti-correlation.

V. Simulation of Light Curve and PSF Map

A. Validation

The anisoplanatic imaging in Section III has been implemented to simulate a realistic light curve of the Hubble Space Telescope (HST) [43] located in low Earth orbit. The ground truth object is modeled as a static image shown in Figure 5 by assuming that the imaging of the space object takes place so rapidly that the stabilized object's scene does not significantly change during the measurement, which can readily be accomplished by Complementary Metal-Oxide-Semiconductor (CMOS) sensor. The simulation parameters are provided in Table 1. The chosen propagation distance is a mean altitude of HST, $L = 550$ km, with $L_{\text{free}} = 500$ km and $L_{\text{turb}} = 50$ km for free space and turbulence propagation distances, respectively.

The strength of the turbulence, or the refractive index structure parameter [44], is modeled as a step function with $C_n^2 = 1.0 \times 10^{-16}$ m$^{-2/3}$ over L_{turb} and nil over L_{free}. The coherence diameter, isoplanatic angle, and log-amplitude variance for the entire optical path are found to be 3.36 cm, 0.368 μrad, and 2.20.

A set of 21 extended phase screens are computed using constrained least squares optimization. They are located equidistant over $L_{\text{turb}} = 50$ km. The coherence diameter of each phase screen is shown in Figure 6. The majority of the screens have coherence diameters of around 20 cm, which is significantly larger than that of the entire optical path, 3.36 cm. This discrepancy can be attributed to the influence of free-space propagation. The last extended phase screen is constrained to have $r_{0_N} = \infty$ to avoid the excessive tilt correlation [26].

Table 1 Simulation Parameters

Parameter	Value
Aperture diameter PSF sensor	$D = 0.61$ m
Focal length PSF sensor	$\ell = 6.25$ m
Wavelength	$\lambda = 525$ nm
Gain of sensor	$g = 12\ e^-$/ADU
Nyquist pixel spacing of phase screens	$\delta = 16.8$ mm
Nyquist pixel spacing of PSFs	$\delta_f = 2.69\ \mu$m
Nyquist pixel spacing of object plane	$\delta_o = 0.237$ m
Pixel spacing of sensor	$\delta_{\text{sensor}} = 2.5\ \mu$m
Propagation distance through free space	$L_{\text{free}} = 500$ km
Propagation distance through turbulence	$L_{\text{turb}} = 50$ km
Propagation step in turbulence	$\Delta z = 2.5$ km
Number of phase screens	$\mathcal{N} = 21$
Extended phase screen samples	$N_{\text{ext}} = 1472$ pixels
Local phase screen samples	$N = 1024$ pixels
Refractive index structure parameter	$C_n^2 = 1.0 \times 10^{-16}$ m$^{-2/3}$
Inner scale	$\ell_0 = 0.01$ m
Outer scale	$L_0 = 300$ m
Object model samples	129×129 pixels
Object plane side length	30.5 m
Pixel skip	2 pixels (65×65 PSF arrays)

Subsequently, numerical wave propagation through free space and turbulence is implemented by the angular spectrum method [27]. The spherical waves are propagated from sample points spaced by two pixels on the object plane of 129×129 pixels, resulting in 65×65 propagated spherical waves.

Figure 7 shows one example of the propagated wave. The irradiance and phase of the propagated wave are well-sampled on the sampling grid. The smallest local phase screen sample size to avoid an aliasing problem is 1024 pixels. This large phase screen size slows down the computation of the angular spectrum method, which needs to be repeated 65^2 times in one simulation. The bottleneck of the computation, the FFT computation, is parallelized on an NVIDIA A100 Tensor Core GPU. As a result, the average computation time for obtaining an image is around 2.4 minutes.

Finally, the simulations are validated through a comparison between the numerical and analytical PSF, as detailed in Section III.E. The numerical PSF is computed by averaging 100 speckle images generated through simulations that utilize distinct sets of extended phase screens to ensure randomness. The analytical PSF is computed based on Eqs.(23)-(25). The results of this validation are presented in Figure 8. The numerical PSF exhibits good agreement with the analytical PSF in both the long- and short-exposure cases.

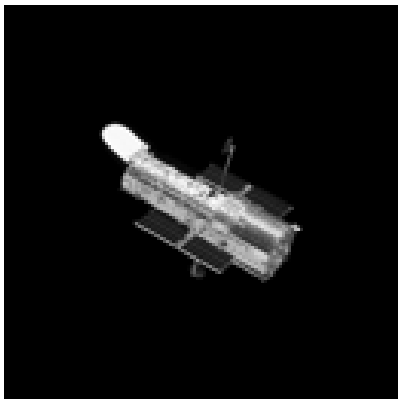

Fig. 5 True object image [43].

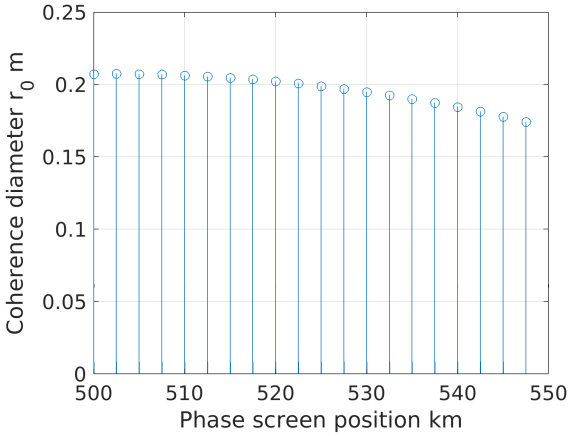

Fig. 6 Atmospheric coherence diameter values for phase screens

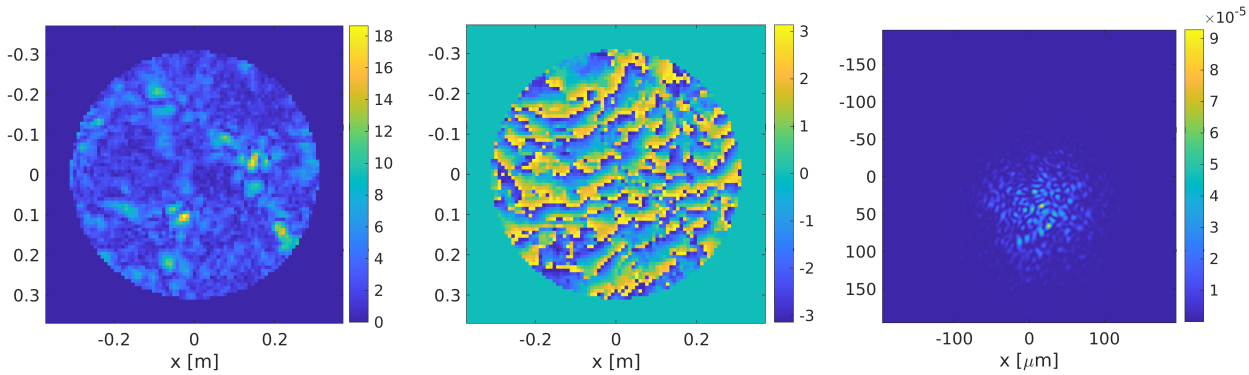

(a) **(b)** **(c)**

Fig. 7 Example of the propagated wave and PSF: (a) Irradiance of the propagated wave, (b) Phase of the propagated wave, (c) Point spread function (PSF).

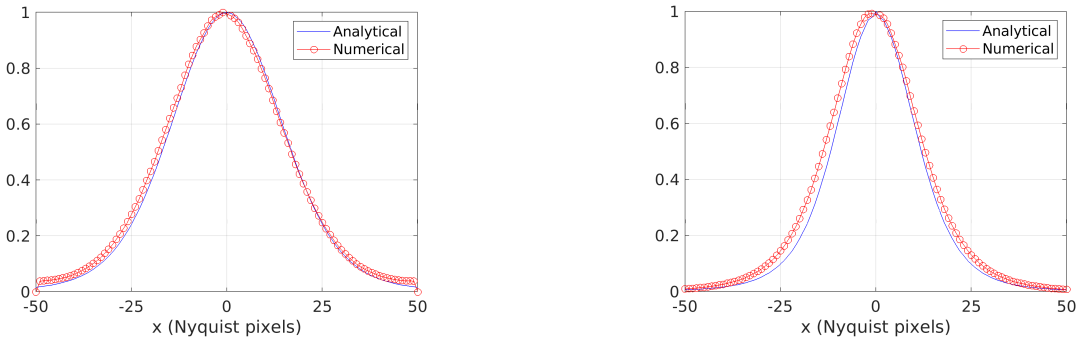

(a) **(b)**

Fig. 8 Validation of average PSF for various exposure times: (a) Long-exposure case ($\alpha = 1$), (b) Short-exposure case ($\alpha = 0$)

B. Illustration

To illustrate the impact of object size on image resolution, a simulation has been performed using four distinct object sizes: 15 m, 10 m, 6 m, and 1 m for the actual Hubble Space Telescope. The simulation results are shown in Figure 9, which shows the images observed by the PSF sensor in the absence of any Poisson noise. The top row of Figure 9 displays the results of numerical wave propagation through free space, while the bottom row exhibits the results when atmospheric turbulence is considered. It is worth noting that the total propagation distance is fixed at $L = 300$ km for a fair comparison. As depicted, the presence of turbulence leads to significant image blurring and distortion, while the free space propagation has minimal impact on the object's appearance. Furthermore, the shape of the object remains recognizable in (e) and (f), but it is rendered nearly unrecognizable in (g) and (h), where it is relegated to the non-resolved regime.

The temporal change of optical turbulence can be also simulated by shifting the extended phase screens by several pixels for 50 frames. The magnitude of the screen shift is determined based on the wind speed of 1 m/s and the frame rate of 40 fps. The object size is kept fixed at 13.2 m for this particular illustration. The results of the images and corresponding PSF maps at four distinct times are presented in Figure 10. The wind blows from the bottom to the top of the images. The results reveal that the warping and brightness of the object are subject to random fluctuations due to the temporal change of the PSFs. Consequently, the observed light intensity also fluctuates over time. Figure 12 (a) displays the normalized light curve obtained from this simulation, where the intensity is normalized by the light curve intensity at the initial frame. Given the slow wind speed, the light curve fluctuates almost continuously. However, in reality, wind speeds are on the order of 10 m/s, which would cause the light to pass through new sets of turbulence layers that are independent of the previous layers. This phenomenon is considered in Figure 11, which displays the images and corresponding PSF maps for higher wind speeds. Although the differences on the PSF maps appear negligible, the corresponding light curve presented in Figure 12 (b) exhibits significant variations. Since the phase screens are temporally uncorrelated, the light curve shows more pronounced and discontinuous fluctuations of the intensity.

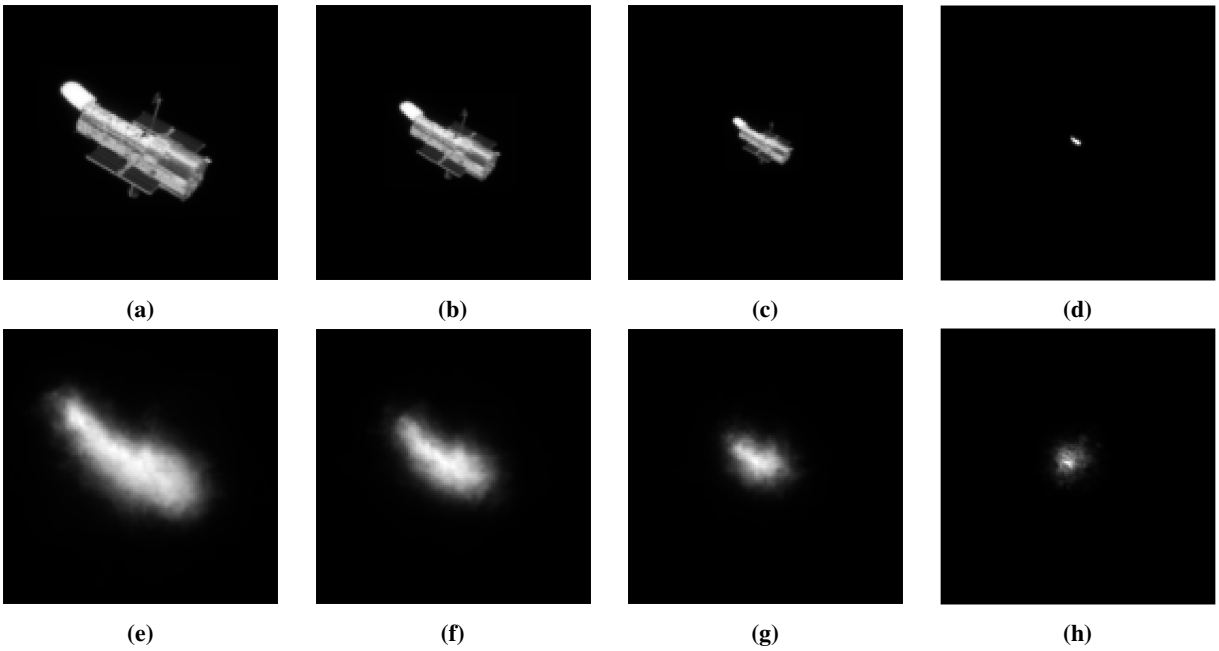

Fig. 9 Comparison of degraded images with and without atmosphere. Top row: without atmosphere, bottom row: with atmosphere. Columns vary by object size: 15 m, 10 m, 6 m, and 1 m from left to right.

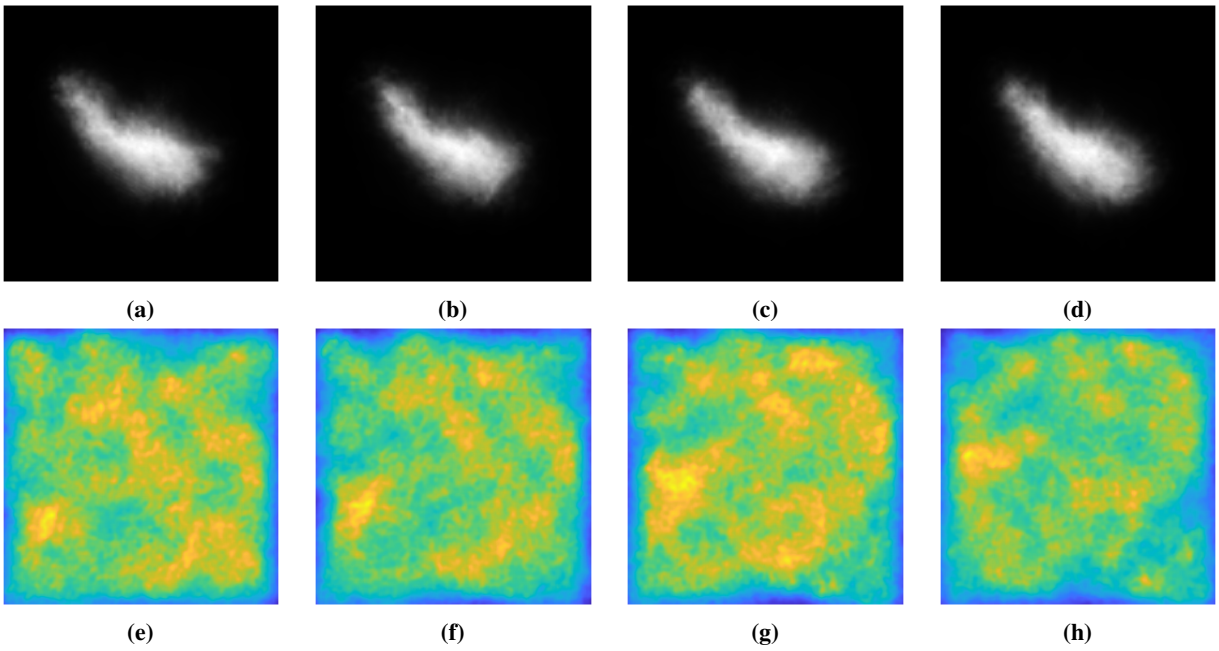

Fig. 10 Impact of slow wind speeds on the degraded image and PSF map. (a)-(d): Images at frame 1, 10, 20, and 30. (e)-(h): PSF map at frame 1, 10, 20, and 30.

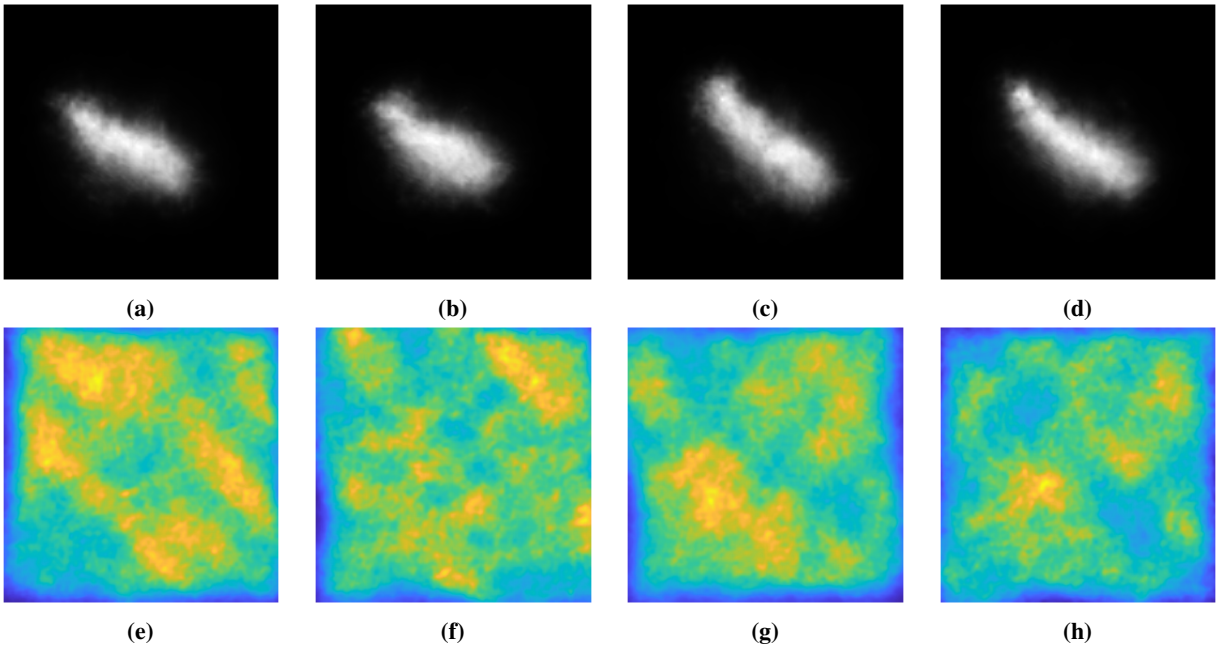

Fig. 11 Impact of high wind speed on the degraded image and PSF map. (a)-(d): Images at frame 1, 10, 20, and 30. (e)-(h): PSF map at frame 1, 10, 20, and 30.

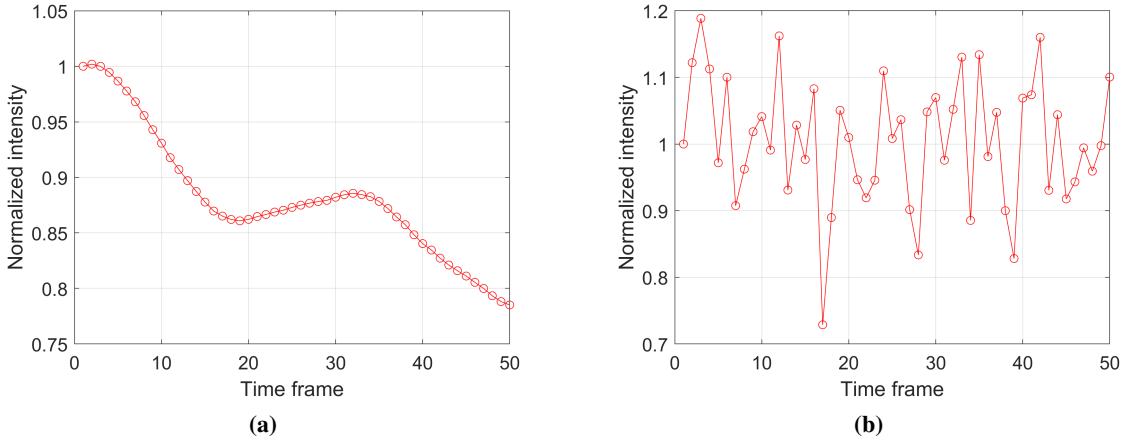

Fig. 12 Normalized light curve obtained by the anisoplanatic imaging simulation : (a) results with wind speed 1m/s, (b) results with temporally-uncorrelated phase screens, which corresponds to a faster wind speed.

VI. Simulation of Image Recovery

A. Perfect PSF Map and Light Curve

To demonstrate the power and potential of the two-dimensional image reconstruction method developed in this paper, several realistic scenarios have been simulated. In the first scenario, the image of the HST is reconstructed solely based on its light curve and PSF maps in the absence of any noise: no Poisson noise in the light curve and perfect knowledge of the PSF map. Fast wind speeds of 20 m/s are assumed for greater realism. The light curve is assumed to be measured by a ground-based optical sensor that has the same or smaller aperture than the PSF sensor, resulting to a completely non-resolved measurement of brightness.

The simulation parameters are shown in Table 1. The object is represented in an image of size 129×129 pixel^2, shown in Figure 5 as before. The HST is scaled to have an axial length of 13.2 m.

The simulation of the light curve and PSF maps is implemented in the following ways. First, a set of phase screens is generated. These phase screens are identical and independent from the other frames to account for fast wind speeds. The non-resolved light curve is computed by summing up the pixel values of degraded image at each time frame. Using the phase screens, the degraded images of the HST and PSF maps are simulated for 2000 frames. Since the pixel spacing of the simulated PSFs, δ, is approximately the same as that of the focal plane, δ_f, the sensor preserves the size of the PSF map to be 129×129 pixels^2. The PSF maps are reshaped into row vectors and concatenated to form a sensing matrix of size 2000×129^2. The region of interest is also computed to limit the number of pixels in the recovery.

Using the light curve and the PSF maps, the image recovery simulation is conducted. The image of HST is recovered through the minimization of the total variation subject to a Dantzig selector constraint. The residual tolerance of the Dantzig selector is tuned by testing five values that are logarithmically spaced between 1e-5 and 1e-4 and by choosing the best value based on visual inspection. Figure 13 (a) shows the recovered image, while the true image is shown in Figure 5. The images are color-coded for better visibility. The recovered image has the SSIM index of 0.971 and clearly shows the main body and aperture door of the HST. This result demonstrates that the PSF maps serve as a nearly perfect sensing matrix, even with only 2000 measurements, which is around 12% of the total number of unknown pixels.

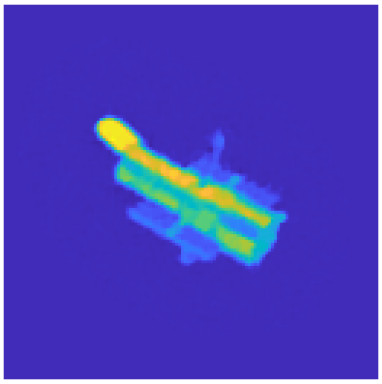

Fig. 13 Image recovery by TV minimization with perfect PSF map and light curve. SSIM=0.971.

B. Noisy PSF Map and Light Curve

In the following subsections, the performance of the proposed method is evaluated under more realistic conditions by reconstructing the HST image based on noisy light curve and PSF maps. The noisy PSF map is simulated by introducing white Gaussian noise to the PSF map, as described in Eq.(32). In contrast, the noisy light curve is computed using Poisson random variables to model noise inherent in photon-limited imaging, as described in Eq.(34).

Two scenarios are investigated to assess the impact of these two types of noise separately. In the first scenario, various levels of Gaussian noise are introduced to the PSF map while maintaining a constant level of Poisson noise in the light curve. In the second scenario, various levels of Poisson noise are introduced to the light curve while maintaining a constant level of Gaussian noise in the PSF map.

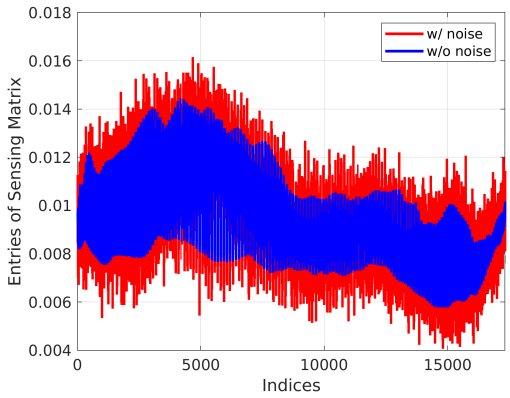

Fig. 14 Comparison of a slice of sensing matrix with (shown in red) and without (shown in blue) Gaussian noise. The noise level is 25%.

1. Various Gaussian Noise in PSF Map

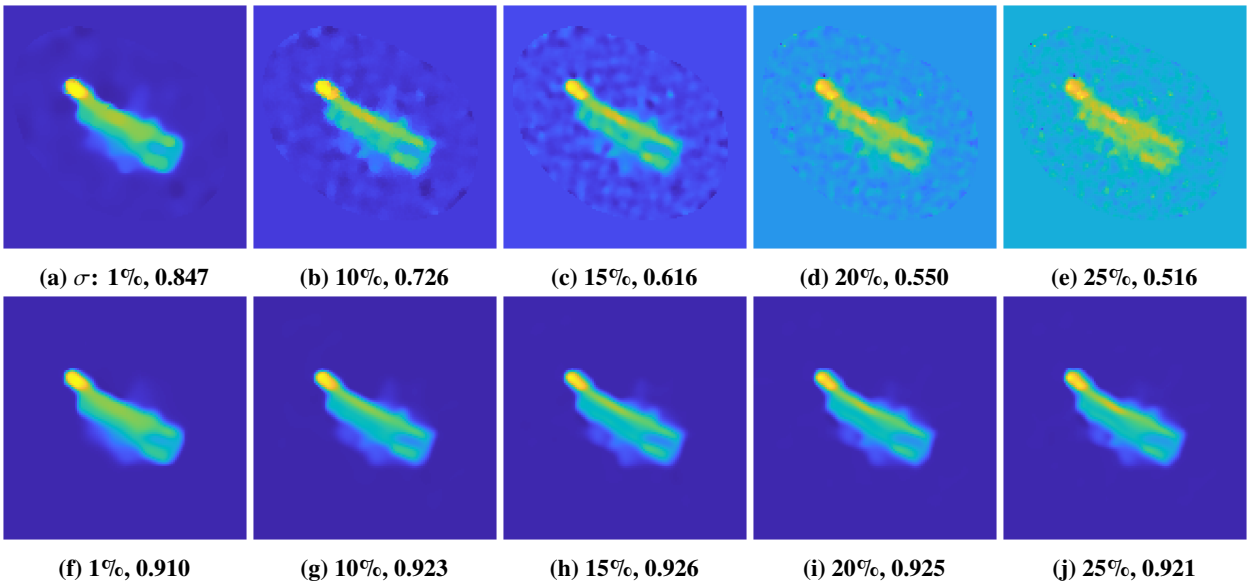

(a) σ: 1%, 0.847 **(b) 10%, 0.726** **(c) 15%, 0.616** **(d) 20%, 0.550** **(e) 25%, 0.516**

(f) 1%, 0.910 **(g) 10%, 0.923** **(h) 15%, 0.926** **(i) 20%, 0.925** **(j) 25%, 0.921**

Fig. 15 Recovered (top) and denoised (bottom) images for the HST with a PSF degraded by five levels of Gaussian noise. Each caption shows the noise level and SSIM.

The performance of the proposed method is evaluated under various levels of Gaussian noise in the PSF map. The noise level in the PSF map is defined in terms of the standard deviation σ in Eq.(32) in the following manner. It is assumed that the three-sigma bound of Gaussian white noise is smaller than the smallest entry of the PSF map since the entries of PSFs are positive. Therefore, the noise level is expressed as a percentage of the smallest entry, and five levels of noise have been simulated: 1%, 10%, 15%, 20%, and 25%. For each noise level, 2000 noisy PSF maps are generated and upscaled to create a sensing matrix of size 2000×129^2. Figure 14 compares the first row of the sensing matrix with and without the additive white Gaussian noise. The added noise level is 25%, which is the highest tested.

In addition, a constant level of Poisson noise is introduced to the light curve. The image intensity is rescaled to a magnitude of 12 to represent a typical brightness of an artificial space object in LEO. The rescaled image is measured by a 32-bit ADC and converted into ADUs. A Poisson random variable is then generated based on the resulting mean value to model an image degraded by Poisson noise, as described in Eq. (33). This procedure is repeated for 2000 frames, with the light curve computed by summing entries of each noisy image.

Using the five noise levels of the PSF map and a single Poisson-degraded light curve, the image reconstruction of the HST at an altitude of 550 km is performed. The recovered HST images are shown in the top row in Figure 15, while the true object image is displayed in Figure 5. The image quality of the results for all the noise levels is degraded in comparison to the results reconstructed with the perfect PSF map displayed in Figure 13. The SSIM values of the recovered images are 0.847, 0.726, 0.616, 0.550, and 0.516 when the PSF map is degraded by a Gaussian noise level of 1%, 10%, 15%, 20%, and 25%, respectively. There is a clear trend that the increased noise in the PSF map degrades the

reconstruction results.

The quality of the reconstructed result is improved by applying the Block Matching and 3D filtering (BM3D) algorithm [45]. The threshold for the noise level required by the BM3D algorithm is adjusted through trial and error. The bottom row in Figure 15 shows the images after applying the BM3D algorithm to the images directly above. The SSIM values are improved by 0.0630, 0.197, 0.310, 0.375, and 0.405 for the noise level of 1%, 10%, 15%, 20%, and 25%, respectively. The denoising is necessary to identify the solar panels and antenna of the HST especially when the PSF map is subject to a larger noise.

2. Various Poisson Noise in Light Curve

This simulation studies the effect of different levels of Poisson noise in the light curve on the reconstruction results while keeping a constant level of Gaussian noise in the PSF map. Like in the previous simulation, the noisy PSF map is modeled using Eq.(32) but the noise level is fixed to 10 %.

Four levels of Poisson noise in the light curves are modeled using Eq.(34). Initially, the image intensity of the HST is scaled to a magnitude of M. The image is subsequently degraded by the light propagation method and measured using a 32-bit ADC. A Poisson variable is then generated based on the resulting mean value. The light curve intensity at a single frame is computed by summing the entries of the noisy image. This procedure is repeated for 2000 frames for four magnitudes: $M = 12$, 13, 14, and 15, resulting in four light curves. A larger magnitude results in darker object and a greater impact of Poisson noise on the light curve.

Figure 16 shows the effect of Poisson noise on the object images and light curves. The columns represent relative magnitudes of 12, 13, 14, and 15 from left to right. The first row displays the random electron counts generated by drawing samples from Poisson distribution. The second row shows the Poisson-degraded light curve obtained by summing the electron counts and by converting it into the relative magnitude. The third row shows the relative error of the light curve in relation to the noiseless light curve. . The impact of Poisson noise on the images and light curves is not evident for relative magnitudes of 12 and 13. In these two cases, the relative error of the light curve is below 1%, as shown in Figure 16 (i) and (j). However, the impact becomes more significant for objects with relative magnitudes of 14 and 15, as shown in Figure 16 (c), (d), (k), and (l).

Given the Poisson-degraded light curves shown in Figure 16 (e)-(h) and a sensing matrix with a noise level of 10%, the image reconstruction of the HST at an altitude of 550 km is performed. The results are shown in Figure 17. The images in the top row are reconstruction results, and the ones in the bottom row are the images after applying the BM3D algorithm. There is a clear trend that the darker objects result in lower image quality in the reconstruction results. For objects with a relative magnitude of 12 , the recovered result has the SSIM of 0.726, and the details of the HST are recognizable even without denoising.

For darker cases, the reconstructed images become noisier and the details are hard to recognize by human eyes,

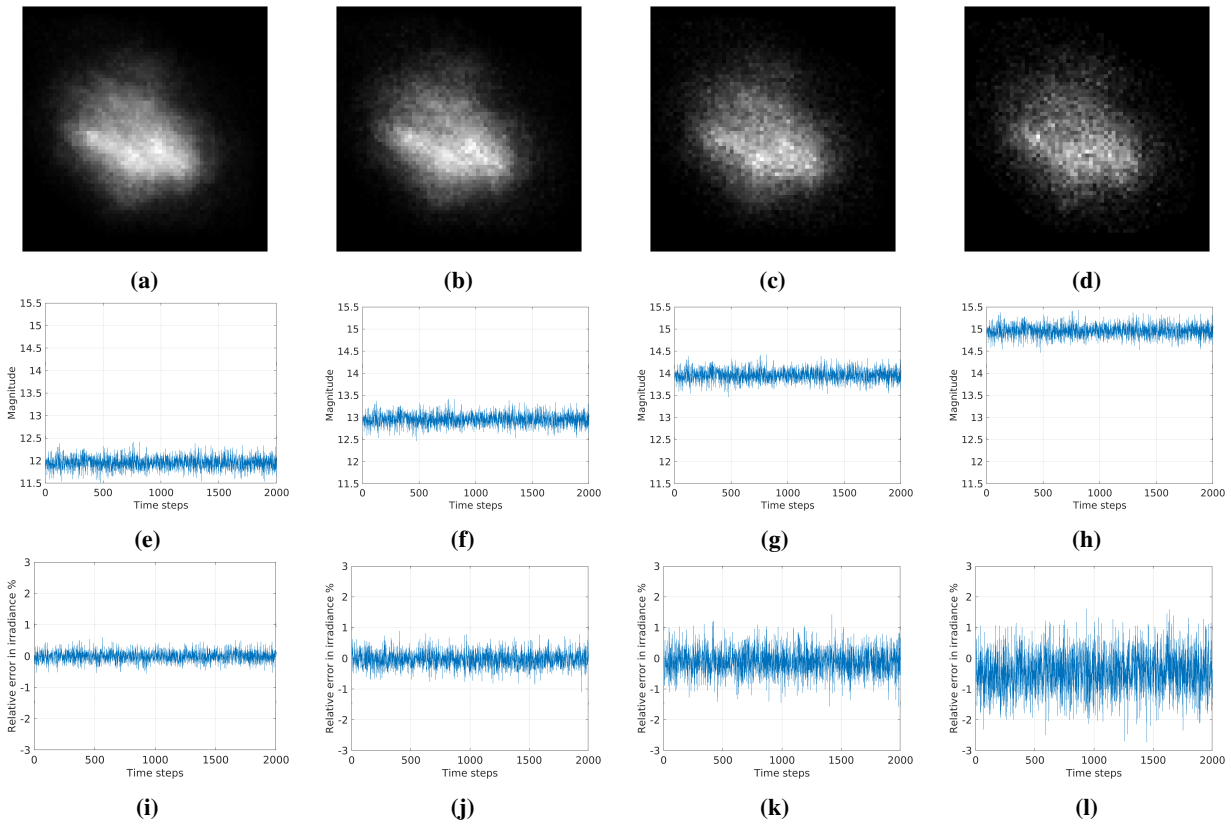

Fig. 16 Poisson noise on image measurement and its effect on light curve intensity. First row: Electron counts with Poisson noise. Second row: Light curve with Poisson noise. Third row: Relative error of light curve. Columns vary by image brightness: magnitude of 12, 13, 14, 15 from left to right.

but they still have the similar structure as the true HST image. As in Eq.(38), the SSIM is a product of the luminance, contrast, and structural terms. The SSIM of Figure 17 (d) has a high structural term of 0.827, but low luminance and contrast terms of 0.522 and 0.406. Therefore, denoising is needed to improve the luminace and contrast quality. The BM3D algorithm can reveal the solar panels for the relative magnitude of 13 with a high SSIM of 0.914. For the relative magnitudes of 14 and 15, the HST details are lost after denoising, but the contrast is restored well, resulting in a high value of SSIM. For example, the contrast term of the SSIM is 0.947 in Figure 17 (h).

Several studies [46, 47] have highlighted the negative impact of Poisson noise in compressed sensing. The TV minimization method with the Dantzig selector constraint assumes that the noise in the light curve is linearly mapped to the measurement residual. However, since the Poisson noise is non-additive and signal-dependent, this method may not be ideal. Despite this, given the low brightness conditions considered in this study, the proposed algorithm demonstrates sufficient robustness for practical applications.

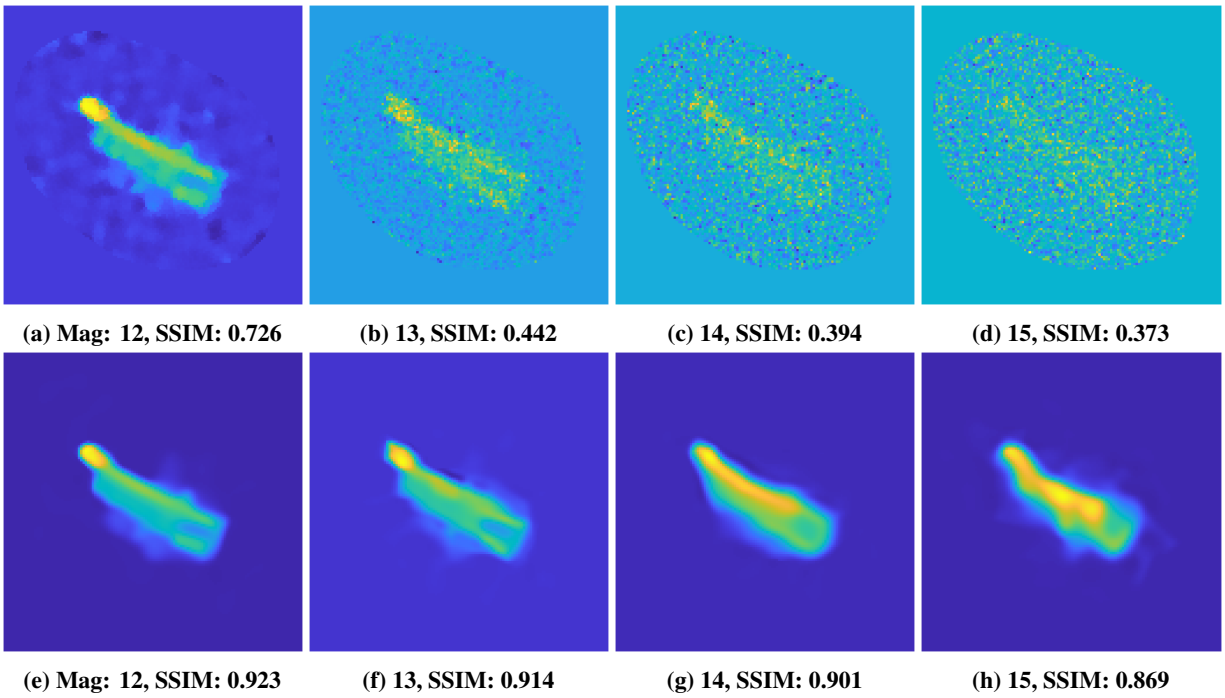

(a) Mag: 12, SSIM: 0.726 **(b) 13, SSIM: 0.442** **(c) 14, SSIM: 0.394** **(d) 15, SSIM: 0.373**

(e) Mag: 12, SSIM: 0.923 **(f) 13, SSIM: 0.914** **(g) 14, SSIM: 0.901** **(h) 15, SSIM: 0.869**

Fig. 17 Recovered (top) and denoised (bottom) images for the HST with various brightness. Each label shows the relative magnitude and SSIM.

VII. Conclusions

This paper presents a method for characterizing a stabilized object in Low Earth Orbit (LEO) by reconstructing a resolved two-dimensional image at a frozen attitude. The inputs for the method are a point spread function (PSF) map and an entirely unresolved light curve. The PSF map is a superposition of spatially-varying PSFs of the atmospheric turbulence, which is assumed to be measurable using PSF determination techniques.

Traditional light curve inversion methods are hindered by high dimensionality and uncertainties in the solution. The proposed method adapts the compressed sensing paradigm commonly employed in image compression. This method overcomes these challenges by recovering a two-dimensional projection of the object of interest rather than reconstructing a three-dimensional shape with additional dimensionality encompassing area-albedo.

Light curves and PSFs are simulated using light propagation through free space and atmospheric turbulence to provide the best realism. Optical perturbation due to atmospheric turbulence is modeled by Monte Carlo phase screens. Illustrations of the resulting degraded imaging for various object sizes are presented.

An image of a space object in LEO is reconstructed based on the simulated light curve and PSFs without any a priori information. The incoherent PSFs obtained from the simulations are superposed to generate a PSF map, which serves as the sensing matrix. However, the sensing matrix does not fulfill the Restricted Isometry Property required for accurate signal recovery in compressed sensing. This problem is alleviated by employing the total variation (TV) minimization with the Dantzig selector constraint for image recovery. Given the PSF map and the light curve without

noise, nearly-perfect image recovery is achieved.

The image recovery is also considered for noisy PSF maps and light curves in two cases. The first scenario involves the presence of five levels of Gaussian noise in the PSF map, with noise levels up to 25% in standard deviation, while assuming a constant level of Poisson noise in the light curve with a magnitude of 12. The larger Gaussian noise in the PSF map degrades the quality of the results. However, after denoising the image by Black-Matching and 3D-filter (BM3D) algorithm, the details of the object becomes discernible. The second scenario involves four levels of object brightness ranging from 12 to 15 in relative magnitude, resulting in various levels of Poisson noise in the light curve while maintaining a noise level of 10% in the PSF map. Since the Poisson noise has a greater impact on the light curve for a darker object, the larger magnitude leads to a lower quality of the recovered image. However, Based on the results of these two scenarios, the proposed method is robust to noise in both the light curve measurement and PSF estimation.

Acknowledgement

This research was made possible by the generous support of the AFOSR (FA9550-19-1-0407 and FA9550-18-1-0154).

References

[1] Kaasalainen, B., and Torpa, J., "Optimization Methods for Asteroid Lightcurve Inversion I. Shape Determination," *Icarus*, Vol. 153, 2001, pp. 24 – 36. https://doi.org/https://doi.org/10.1006/icar.2001.6673.

[2] Kaasalainen, B., Torpa, J., and Muinonen, K., "Optimization Methods for Asteroid Lightcurve Inversion II. The Complete Inverse Problem," *Icarus*, Vol. 153, 2001, pp. 37 – 51. https://doi.org/https://doi.org/10.1006/icar.2001.6674.

[3] Yanagisawa, T., and Kurosaki, H., "Shape and motion estimate of LEO debris using light curves," *Advances in Space Research*, Vol. 50, No. 1, 2012, pp. 136–145. https://doi.org/https://doi.org/10.1016/j.asr.2012.03.021.

[4] Linares, R., Jah, M., and Crassidis, J., "Inactive space object shape estimation via astrometric and photometric data fusion," *Advances in the Astronautical Sciences*, Vol. 143, 2012, pp. 217–232.

[5] Linares, R., Jah, M. K., Crassidis, J. L., and Nebelecky, C. K., "Space object shape characterization and tracking using light curve and angles data," *Journal of Guidance, Control, and Dynamics*, Vol. 37, No. 1, 2014, pp. 13–25. https://doi.org/10.2514/1.62986.

[6] Linares, R., and Crassidis, J. L., "Space-Object Shape inversion via Adaptive Hamiltonian Markov Chain Monte Carlo," *Journal of Guidance, Control, and Dynamics*, Vol. 41, No. 1, 2018, pp. 47–58. https://doi.org/https://doi.org/10.2514/1.G002296.

[7] Fan, S., and Frueh, C., "A Direct Light Curve Inversion Scheme in the Presence of Measurement Noise," *The Journal of the Astronautical Sciences*, Vol. 67, 2019. https://doi.org/10.1007/s40295-019-00190-3.

[8] Fan, S., and Frueh, C., "Multi-Hypothesis Light Curve Inversion Scheme for Convex Objects with Minimal Observations," *Proceedings of the 8th European Conference on Space Debris*, ESA Space Debris Office, 2021, pp. 1–7.

[9] Robinson, L., and Frueh, C., "Light Curve Inversion for Reliable Shape Reconstruction of Human-Made Space Objects," *Proceedings of the 32nd AIAA/AAS Astrodynamics Specialist Conference*, 2022, pp. 1–19.

[10] Linares, R., and Furfaro, R., "Space Object Classification Using Deep Convolutional Neural Networks," *19th International Conference on Information Fusion*, 2016, pp. 1–8.

[11] Furfaro, R., Linares, R., and Reddy, V., "Space Objects Classification via Light-Curve Measurements: Deep Convolutional Neural Networks and Model-based Transfer Learning," *Proceedings of the 19th Advanced Maui Optical and Space Surveillance Technologies Conference*, 2018, p. 17.

[12] Furfaro, R., Linares, R., and Reddy, V., "Shape Identification of Space Objects via Light Curve Inversion Using Deep Learning Models," *Proceedings of the 20th Advanced Maui Optical and Space Surveillance Technologies Conference*, edited by S. Ryan, 2019, p. 17. https://doi.org/https://doi.org/10.1007/s40295-019-00208-w.

[13] Allworth, J., Windrim, L., Bennett, J., and Bryson, M., "A transfer learning approach to space debris classification using observational light curve data," *Acta Astronautica*, Vol. 181, 2021, pp. 301–315. https://doi.org/10.1016/j.actaastro.2021.01.048.

[14] McNally, K., Ramirez, D., Anton, A. M., Smith, D., and Dick, J., "Artificial Intelligence For Space Resident Objects Characterisation With Lightcurves," *Proceedings of the 8th European Conference on Space Debris*, ESA Space Debris Office, 2021, pp. 1–12.

[15] Kerr, E., Elisabeth, G. P., Talon, P., and Petit, D., "Using AI to Analyse Light Curves for GEO Object Characterisation," *Proceedings of the 22nd Advanced Maui Optical and Space Surveillance Technologies Conference*, 2021, pp. 1–9.

[16] Candès, E. J., et al., "Compressive sampling," *Proceedings of the international congress of mathematicians*, Vol. 3, Madrid, Spain, 2006, pp. 1433–1452. URL https://api.semanticscholar.org/CorpusID:2269521.

[17] Candes, E. J., Romberg, J. K., and Tao, T., "Stable signal recovery from incomplete and inaccurate measurements," *Communications on Pure and Applied Mathematics: A Journal Issued by the Courant Institute of Mathematical Sciences*, Vol. 59, No. 8, 2006, pp. 1207–1223. https://doi.org/https://doi.org/10.1002/cpa.20124.

[18] Donoho, D. L., "Compressed sensing," *IEEE Transactions on information theory*, Vol. 52, No. 4, 2006, pp. 1289–1306. https://doi.org/https://doi.org/10.1109/TIT.2006.871582.

[19] Nyquist, H., "Certain topics in telegraph transmission theory," *Transactions of the American Institute of Electrical Engineers*, Vol. 47, No. 2, 1928, pp. 617–644. https://doi.org/https://doi.org/10.1109/T-AIEE.1928.5055024.

[20] Kobayashi, D., and Frueh, C., "Compressed Sensing for Satellite Characterization," *Proceedings of the 20th AAS/AIAA Astrodynamics Specialist Conference*, 2020.

[21] Kobayashi, D., and Frueh, C., "Reformulating Compressed Sensing to be used with Semi-Resolved Point Spread Function and Light Curves for Space Object Imaging: LEO," *Proceedings of AMOS technical conference*, 2022.

[22] Candes, E., and Tao, T., "Decoding by linear programming," *IEEE Transactions on Information Theory*, Vol. 51, No. 12, 2005, pp. 4203–4215. https://doi.org/10.1109/TIT.2005.858979.

[23] Bandeira, A., Dobriban, E., Mixon, D., and Sawin, W., "Certifying the restricted isometry property is hard," *IEEE Transactions on Information Theory*, Vol. 59, No. 6, 2013, pp. 3448–3450. https://doi.org/10.1109/TIT.2013.2248414.

[24] Baraniuk, R., Davenport, M., DeVore, R., and Wakin, M., "A simple proof of the restricted isometry property for random matrices," *Constructive Approximation*, Vol. 28, No. 3, 2008, pp. 253–263. https://doi.org/10.1007/s00365-007-9003-x.

[25] Takhar, D., Laska, J. N., Wakin, M. B., Duarte, M. F., Baron, D., Sarvotham, S., Kelly, K. F., and Baraniuk, R. G., "A new compressive imaging camera architecture using optical-domain compression," *Computational Imaging IV*, Vol. 6065, International Society for Optics and Photonics, 2006, p. 606509. https://doi.org/10.1117/12.659602.

[26] Hardie, R. C., Power, J. D., LeMaster, D. A., Droege, D. R., Gladysz, S., and Bose-Pillai, S., "Simulation of anisoplanatic imaging through optical turbulence using numerical wave propagation with new validation analysis," *Optical Engineering*, Vol. 56, No. 7, 2017, p. 071502. https://doi.org/10.1117/1.OE.56.7.071502.

[27] Schmidt, J. D., "Numerical simulation of optical wave propagation: With examples in MATLAB," SPIE, 2010. https://doi.org/10.1117/3.866274.

[28] McGlamery, B. L., "Restoration of Turbulence-Degraded Images*," *Journal of the Optical Society of America*, Vol. 57, No. 3, 1967, pp. 293–297. https://doi.org/10.1364/JOSA.57.000293, URL https://opg.optica.org/abstract.cfm?URI=josa-57-3-293.

[29] Frehlich, R., Sharman, R., Vandenberghe, F., Yu, W., Liu, Y., Knievel, J., and Jumper, G., "Estimates of Cn2 from Numerical Weather Prediction Model Output and Comparison with Thermosonde Data," *Journal of Applied Meteorology and Climatology*, Vol. 49, No. 8, 2010, pp. 1742 – 1755. https://doi.org/https://doi.org/10.1175/2010JAMC2350.1, URL https://journals.ametsoc.org/view/journals/apme/49/8/2010jamc2350.1.xml.

[30] Hufnagel, R. E., and Stanley, N. R., *Propagation through atmospheric turbulence*, SPIE Press, 1985. Chapter 6.

[31] Quatresooz, F., Vanhoenacker-Janvier, D., and Oestges, C., "Computation of Optical Refractive Index Structure Parameter from its Statistical Definition Using Radiosonde Data," *Radio Science*, Vol. 58, No. 1, 2023. https://doi.org/10.1029/2022RS007624, URL https://agupubs.onlinelibrary.wiley.com/doi/10.1029/2022RS007624.

[32] Fried, D. L., "Statistics of a geometric representation of wavefront distortion," *Journal of the Optical Society of America*, Vol. 55, No. 11, 1965, pp. 1427–1435. https://doi.org/10.1364/JOSA.55.001427.

[33] Lane, R., Glindemann, A., and Dainty, J., "Simulation of a Kolmogorov phase screen," *Waves in random media*, Vol. 2, No. 3, 1992, p. 209. https://doi.org/10.1088/0959-7174/2/3/003.

[34] Voelz, D. G., *Computational fourier optics: a MATLAB tutorial*, SPIE, 2011. https://doi.org/10.1117/3.858456.ch5, chapter 5.

[35] Goodman, J. W., *Statistical optics*, John Wiley & Sons, 2015. ISBN: 978-1-119-00945-0.

[36] Pogson, N., "Magnitudes of Thirty-six of the Minor Planets for the first day of each month of the year 1857," *Monthly Notices of the Royal Astronomical Society*, Vol. 17, 1856, pp. 12–15. https://doi.org/10.1093/mnras/17.1.12.

[37] Beltramo-Martin, O., Ragland, S., Fétick, R., Correia, C., Dupuy, T., Fiorentino, G., Fusco, T., Jolissaint, L., Kamann, S., Marasco, A., et al., "Review of PSF reconstruction methods and application to post-processing," *Adaptive Optics Systems VII*, Vol. 11448, SPIE, 2020, pp. 22–36. https://doi.org/10.1117/12.2560805.

[38] Elad, M., *Sparse and redundant representations: from theory to applications in signal and image processing*, Vol. 2, Springer, 2010. https://doi.org/https://doi.org/10.1007/978-1-4419-7011-4.

[39] Rudin, L. I., Osher, S., and Fatemi, E., "Nonlinear total variation based noise removal algorithms," *Physica D: nonlinear phenomena*, Vol. 60, No. 1-4, 1992, pp. 259–268. https://doi.org/https://doi.org/10.1016/0167-2789(92)90242-F.

[40] Candes, E., and Tao, T., "The Dantzig selector: Statistical estimation when p is much larger than n," *The annals of Statistics*, Vol. 35, No. 6, 2007, pp. 2313–2351. https://doi.org/10.1214/009053606000001523.

[41] Boyd, S., and Vandenberghe, L., *Convex optimization*, Cambridge university press, 2004. https://doi.org/https://doi.org/10.1017/CBO9780511804441.

[42] Wang, Z., Bovik, A. C., Sheikh, H. R., and Simoncelli, E. P., "Image quality assessment: from error visibility to structural similarity," *IEEE transactions on image processing*, Vol. 13, No. 4, 2004, pp. 600–612. https://doi.org/10.1109/TIP.2003.819861.

[43] NASA, "About the Hubble Space Telescope," , 2009. URL https://www.nasa.gov/mission_pages/hubble/story/index.html.

[44] Roggemann, M. C., and Welsh, B. M., *Imaging through turbulence*, CRC press, 1996. ISBN: 978-1-119-00945-0.

[45] Mäkinen, Y., Azzari, L., and Foi, A., "Collaborative filtering of correlated noise: Exact transform-domain variance for improved shrinkage and patch matching," *IEEE Transactions on Image Processing*, Vol. 29, 2020, pp. 8339–8354. https://doi.org/10.1109/TIP.2020.3014721.

[46] Raginsky, M., Willett, R. M., Harmany, Z. T., and Marcia, R. F., "Compressed sensing performance bounds under Poisson noise," *IEEE Transactions on Signal Processing*, Vol. 58, No. 8, 2010, pp. 3990–4002. https://doi.org/10.1109/TSP.2010.2049997.

[47] Raginsky, M., Jafarpour, S., Harmany, Z. T., Marcia, R. F., Willett, R. M., and Calderbank, R., "Performance bounds for expander-based compressed sensing in Poisson noise," *IEEE Transactions on Signal Processing*, Vol. 59, No. 9, 2011, pp. 4139–4153. https://doi.org/10.1109/TSP.2011.2157913.

The Journal of the Astronautical Sciences
https://doi.org/10.1007/s40295-019-00190-3

ORIGINAL ARTICLE

A Direct Light Curve Inversion Scheme in the Presence of Measurement Noise

Siwei Fan[1] · **Carolin Frueh**[1]

Published online: 29 August 2019

Abstract
Shape and attitude of resident space objects directly affect the orbit propagation via drag and solar radiation pressure. Obtaining information beyond an object state is integral to identifying an object, aid in tracing its origin and its capabilities. For objects that have a significant distance to the observer, only non-resolved imaging is available, which does not reveal any details of the object. So-called non-resolved light curve measurements, i.e. brightness measurements over time, can be used to determine the shape of convex space objects using an inversion scheme. The inversion process starts by first determining the Extended Gaussian Image and then solving Minkowski problem to obtain the closed shape result. In this paper, the effect of measurement noise on the shape inversion and the influence of the measurement geometry is investigated. Despite the presence of measurement noise, in a new methodology, expanding upon established inversion techniques, almost perfect inversion results can be obtained in a two-step process: first, an initial light curve is used for shape hypothesis creation, and then, a second (potentially very short) light curve is used for selection of the best hypothesis. Results are shown for two standard shapes of a cuboid and a house shape.

Keywords Space situational awareness · Light curve · Inversion · Extended Gaussian Image · Measurement noise

Introduction

Space situational awareness focuses on obtaining extensive knowledge of the object of interest, usually in the near-Earth regime. The object state, which traditionally consists of position and velocity, is of the interest. Recently, it has come to the attention

✉ Siwei Fan
fan11@purdue.edu

[1] School of Aeronautics and Astronautics, Purdue University, West Lafayette, IN 47906, USA

that the information beyond the object state is also crucial. The so-called characterization information includes the information on attitude motion, shape, and material of the space object. The characterization information can aid the object identification process, but also has a direct influence on the state propagation via non-conservative orbital perturbations such as solar radiation pressure and atmospheric drag.

One way to access the characterization information is via the light curves, which are brightness measurements over time. The reflected brightness that is received by an observer is dependent upon the observation geometry: the location of the observer, the object, and the Sun. The brightness is also affected equally by the object properties: the object's surface properties including shape, materials and its attitude motion. The shape inversion problem is determining an object's shape given its light curve(s). The problem is heavily under-determined: only one-dimensional brightness measurements as a function of time are available, whereas the desired state of the complete shape information can require easily several hundred to several thousand entries. Furthermore, the dependencies, such as attitude and materials, also directly influence the results. Lastly, no measurement process is perfect, and measurement noise can significantly influence the results, especially in under-determined problems.

Light curves have been studied extensively for asteroids and various techniques exist [13, 15–17] to retrieve the asteroid shape information. Asteroids usually have a main axis rotation and smooth surfaces made of a single surface material, which allows for simplifying assumptions in the shape inversion process. Human-made space objects, such as satellites and space debris, generally expose various surface materials and exhibit sharp edges. While many active objects have a controlled attitude, simplifying the problem, it has been shown that in general [4, 7, 27], no main axis attitude motion can be assumed for non-controlled space objects.

Light curve research for artificial space objects can be divided in three categories. The first approach focuses on information about materials. Lynch et al. [26] analyzed the surface material properties closely on 3 GEO satellites using the AEOS telescope. Hejduk [11] also analyzed the specular and diffuse reflection and concluded that albedo distribution on a sphere is not sufficient in modeling satellites. Cowardin et al. [2] established a laboratory setup for measuring photometric brightness by mounting different pieces of materials on a robot arm and concluded that reflectivity reduces significantly after a collision. Seitzer et al. [36] analyzed the survey data obtained using MODEST as well as SMARTS and categorized the GEO debris according to its magnitude and color. Schildknecht et al. [32–34] used ground-based optical telescopes to perform color photometry and distinguish GEO debris by material types and potential origins.

The second set of approaches, is focusing on tracing signatures of space objects and correlating with *a priori* knowledge. Cowardin et al. [3] compared optical measurement of Titan fragments with laboratory results to obtain the best match result. Scott et al. [35] established a light curve catalog based on satellite bus types, and made the comparison to differentiate objects. Payne et al. [30] who developed a ray-tracing approach for a multi-facet model on GEO, focused on comparing the signature of objects on a single pass. Armstrong et al. [1] suggested from glint observation and image analysis on a GEO satellite, that optical interferometry could capture such objects directly.

In the third approach, the focus is laid directly on shape inversion. Hall et al. [10] presented various methods for retrieving rough shapes and attitude of space objects, where different conditions may apply. He also concluded that the NASA IMAGE satellite has stopped responding based purely on the photometric data. In the hope to find more conclusive results, shape inversion has been combined with orbit propagation, combining light curve measurements and orbit propagation, as the problems are coupled [18]. This comes at the cost of having a problem with a high number of parameters, which is not readily solved and still exhibits ambiguities. Furfaro et al. [8] took the inversion problem into a complete problem of characterization and behavior analysis of any objects in space through the use of machine learning where Bayesian Networks are formed. By using unscented Kalman filter, Linares et al. [21, 22] proposed a data fusion technique to estimate object shape by combining the brightness and angle data, with successful simulation scenarios.

Additionally, the structure of incorporating multiple hypothesis have been proven to be useful in solving the object characterization problem. Gaylor et al. [9] proposed a complete Hierarchical Mixtures of Experts (HME) architecture that is designed to fully characterize resident space objects by using multiple layers of experts and gating networks, where results have been shown for the attitude characterization. Linares et al. [20] used multiple-model adaptive estimation (MMAE) to achieve a similar function of selecting most probable shapes out of several candidate shapes in addition to its states. The most significant advantage of those frameworks is that a conclusive statement can be made in terms of the best candidate for object shape, however both approaches have significant limitations. As for realistic scenarios with unbearably many experts, that is input shape models are required such as *similar* shapes, do not lead to similar light curve traces in this highly non-linear regime, whereas similar light curves may stem from vastly different shapes. The problem is also not additive, such that easy combinations of simple generic shapes could be formed based on several input experts.

Embracing the presence of measurement errors, Linares [19] evaluated Bayes rule directly for the shape inversion problem, and, under simplifying assumptions, an output distribution could be shown at significant computational cost without leading to output shapes.

In the approach presented in this paper, first the influence of measurement noise and measurement geometry on the shape inversion is shown, following a classical scheme [13, 15–17] of Extended Gaussian Image estimation and subsequent shape determination as a solution to Minkowski theorem. Secondly, in the tradition of MMAE and HME filters, a two step light curve shape inversion scheme is developed. The first light curve is used to generate equally weighted, equally possible shape hypotheses based on the aforementioned approach. In a second step, a much shorter light curve is sufficient to select, the highest weighted shape hypothesis. It is shown, that the selected shape is very close to the original one, evaluating differences in area, normal directions, and support functions. For the sake of comparison, it is explicitly shown that the two step process outperforms a single inversion, taking the combined data (light curve one and two) together without using the two step process. It also

circumvents that the need of other HME and MMAE architectures [9, 20] to define *a priori* shapes.

Methodology

The inversion scheme for a single light curve consists of the determination of its Extended Gaussian Image (EGI), followed by a Minkowski minimization and dual transform to find a closed shape. If the light curve noise affected, a non-perfect inversion result is expected. In order to explore the solution space, the noise is populated in a Monte-Carlo approach leading to shape hypotheses. In a second step, the shape hypotheses are correlated with an additional light curve, in order to find the best hypothesis.

Extended Gaussian Image (EGI)

As shown by Minkowski [29] in 1909, a polytope can be described via its EGI, which maps the surface areas and associated normal directions onto a unit sphere [12, 23, 25, 28]. The discrete representation of an EGI for a polytope with n surface facets and associated normal directions $\mathbf{n_i}$ with associated areas A_i in those normal directions can be expressed as the following for a unit sphere S with m discrete normal directions $\mathbf{n}_s$:

$$\text{EGI} = \left\{ A_s = \sum A_i | \mathbf{n}_s = \mathbf{n}_i : 1 \leq s \leq m, 1 \leq i \leq n \right\}, \{\mathbf{n}_s : 1 \leq s \leq m\} \quad (1)$$

Usually $m \neq n$. The area A_i of the i-th flat facet will be registered to the unit sphere of the EGI as the s^{th} entry. When multiple facets satisfy the condition, the sum of those areas will be registered instead. Minkowski showed that the EGI is unique for a given convex polytope up to rotations. The reference origin of the EGI is specified in the center of the unit sphere, by definition, for a convex object. The EGI representation of a shape has the significant advantage that it is independent of the viewing angle. In our case, a complication with optical observations is that only albedo-area, that is the product of area and the reflectivity of the given surface, is available. Therefore, the EGI used in this research consists of the surface normal vector and the associated albedo-area instead. Figure 1 shows three examples of EGI representations, two of them are used in the simulation result section.

One difficulty in practice using EGI representation is the realization of the discrete sphere with equal or near equal areas associated with each normal direction. In this paper, the quad-cube method [37] has been adopted, leading to nearly uniform distribution of normal directions over the unit sphere. In Fig. 1 the EGI direction sampling is constructed with $m = 150$ and 294 tessellation facets on the unit sphere. The color indicates the associated area (albedo-area). Figure 1c, f, i are the exact same representation of Fig. 1b, e, h except all the *gaps* between the normal directions are completely patched for illustration purposes. It is obvious that the more densely the EGI vector list is sampled or the larger the m number, the more accurate the discrete

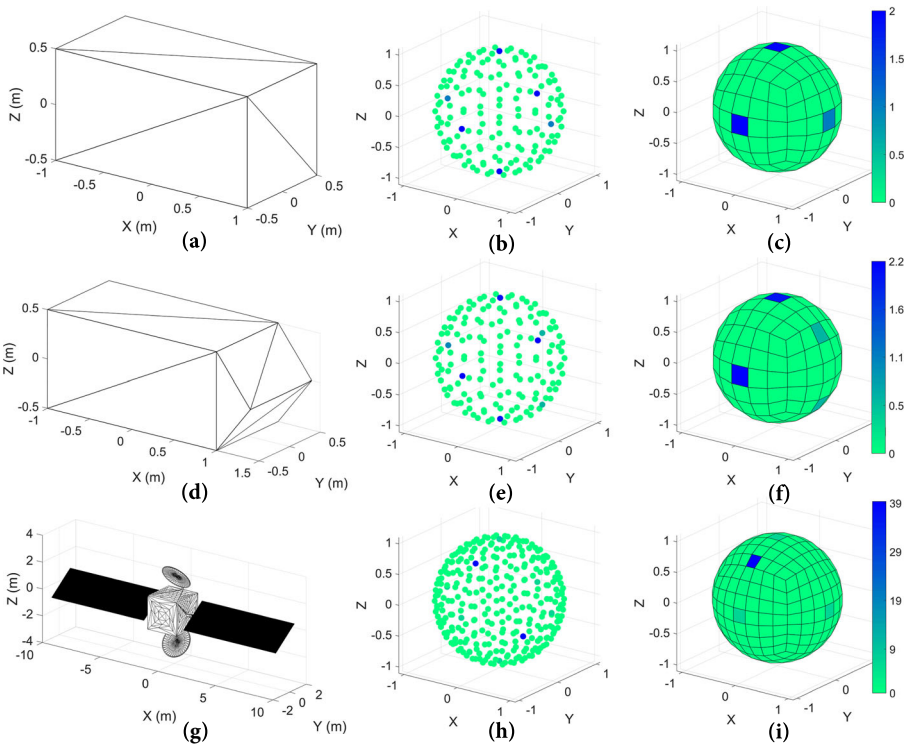

Fig. 1 Extended Gaussian Image example: **a** 2x1x1 Cuboid, **b** Dot representation of EGI ($m = 150$) corresponding to Cuboid, **c** Facet representation of EGI corresponding to Cuboid, **d** House shape with roof tip at $x = 1.4$, **e** Dot representation of EGI ($m = 150$) corresponding to House, **f** Facet representation of EGI corresponding to House, **g** Sample box-wing satellite model, **h** Dot representation of EGI ($m = 294$) corresponding to the box-wing satellite model, **i** Facet representation of EGI corresponding to the box-wing satellite model

EGI representation can be. An EGI representation of $m = 150$ leads to a tolerance of about 6 degrees on the normal direction, and about 4 degrees for $m = 294$.

EGI Optimization Problem

For the scope of this paper, we adopted similar practice by Kaasalainen [14] forming the first optimization problem based on the classic Lambertian reflection model, which takes the brightness data (simulated or measured data) vector $\mathbf{L}$ as input and the albedo-area vector $\mathbf{a}$ as output. The linear least squares cost function is:

$$J = |\mathbf{L} - G\mathbf{a}|^2, \tag{2}$$

$$\text{with } \mathbf{a} = [a_1, ..., a_s, ...a_m]^T \text{ under the constraint } a_s \geq 0 \ \forall s. \tag{3}$$

G is the reflection matrix, mapping the albedo-areas in a given normal direction with the reflection response that is received. It contains the relationship that happens

among the Sun, the observer, and the viewing object, and it is of the size l by m. The column size m is unanimous with the EGI sampling setting. The row size l is in time domain, determined by the resolution of measurement data. The constraint is introduced such that all areas are positive. Mathematically, this means that the Gaussian curvature could be negative, which leads to the existence of concavities in the inversion process.

The elements of the reflection matrix G are computed modeling the object surface as a mixture of specular C_s, Lambertian reflection C_d, and absorption C_a of a distant point source. Each row of G corresponds to one time instance t_i, each element in the row to one normal direction $\mathbf{n}_s$:

$$\begin{aligned} G(t_i)_s = \; & I_0 \frac{1}{\pi (r_{\text{topo}}(t_i))^2} \cdot [\hat{\mathbf{o}}_s(t_i) \cdot \hat{\mathbf{n}}_s \\ & + \lambda \cdot \delta(\hat{\mathbf{o}}_s(t_i) \cdot \hat{\mathbf{n}}_s - \hat{\mathbf{n}}_s \cdot \hat{\mathbf{s}}_s(t_i)) \cdot \delta(\hat{\mathbf{s}}_s(t_i) \times \hat{\mathbf{n}}_s - \hat{\mathbf{n}}_s \times \hat{\mathbf{s}}_s(t_i))] \\ & s = 1, ..., mi = 1, ..., l \end{aligned} \tag{4}$$

I_0 is the irradiance of the Sun, $r_{\text{topo}}(t_i)$ is the observer-object distance at the time t_i. The two vectors, $\hat{\mathbf{o}}_s(t_i)$, and $\hat{\mathbf{s}}_s(t_i)$ are the unit vectors from the object position towards the observer and the Sun, respectively. The elements of the corresponding albedo-area vector **a** are:

$$a_s = \; C_d A_s \qquad s = 1, ..., m \tag{5}$$

It should be noted that a fixed relation between C_s and C_d has to be assumed, in order to make Eq. 3 a linear estimation, when both reflections are present:

$$C_s = \lambda \, C_d \qquad \text{with} \;\; 1 = C_d(1 + \lambda) + C_a \tag{6}$$

The condition on λ represents energy conservation and that the object surface is assumed to be opaque.

For this paper, λ is set to zero, or in other words, all objects are assumed to have no specular reflection component. In order to compute the reflection matrix G in Eq. 4, the attitude motion, that is the transformation from the inertial to the body frame has to be known, as the EGI representation of a rigid body is not rotation invariant. Lastly, the size of m is sought to be as high as possible to render the best representation of the polygon and capture all normal directions and associated areas as precisely as possible. The size of m is limited by the number of measurements that are available, in order to not render matrix G rank-deficient. A maximum total area constraint can be added to avoid any unrealistically large area values.

Shape Recovery: Solving for Adjacency Information

While the EGI is unique for a convex object, the EGI is not sufficient to reconstruct the polygon shape as the EGI only indicates the facet area a_s and its facing direction n_s. It is hence lacking the adjacency information, or equivalently, the distance of the facet to the center of the object. For a convex object, this distance is the shortest distance, and there is a unique vector that passes through the origin while being perpendicular to the facet, the so-called support of the surface area plane h_s. Its direction is the facet normal or equivalently the EGI sampling direction $\mathbf{n}_s$. The quantity

$h_s \cdot \mathbf{n}_s$ is the position vector of the point on each facet that is closest to the object center. By treating these closest points on every facet as vertices, it is possible to construct a convex hull, which is in fact, the dual polygon of the shape to be recovered. As a result, the final shape can be obtained by performing the dual transform on the convex hull formed using the closest points.

Based on Minkowski theorem, several methods exist [24, 25] to solve for the support h_s. For a uniform reflection with a fixed reflection coefficient, one can explicitly show, that Minkowski theorem still holds for the case when only albedo-areas a_s in Eq. 5 are available, C_d is a constant:

$$\sum_{s=1}^{m} a_s \cdot \mathbf{n}_s = C_d \sum_{s=1}^{m} A_s \cdot \mathbf{n}_s = 0. \tag{7}$$

The summation over a closed surface of a convex polygon $\sum_{s=1}^{m} A_s \cdot \mathbf{n}_s$ goes the same as in the original Minkowski formulation. The equation can also be revised to accommodate specular reflection, using the fixed relation stated in Eq. 6.

One method with a known and bounded error is the reconstruction of a convex hull and utilization of the Brunn-Minkowski theorem, while constraining the reconstructed object to stay on a constant hyperplane [25]. This leads to the formulation of a direction optimization problem [24] (8). Alternatively, one can treat the problem as finding the polygon given a set of half-spaces.

$$J = \frac{1}{3}\tilde{\mathbf{h}} \cdot \mathbf{a} \tag{8}$$

$$\text{with} \quad \tilde{\mathbf{h}} \cdot \mathbf{a} = \text{constant} \tag{9}$$

Known input quantity is the EGI area list, defined as $\mathbf{a}$ with elements a_s from Eq. 5, given in the (regular) home space where the albedo-area value is physically defined. The vector $\tilde{\mathbf{h}}$ is the vector of the corresponding support h_s. The tilde denotes the dual (scaled) space due to the hyperplane constraint Eq. 9. The hyperplane condition constrains the volume of the output shape. As a result, the output is out of scale by a factor. The re-scaling can be done by matching up one of the facet areas with the EGI value (from the previous EGI optimization step), leading to the actual support vector $\mathbf{h}$ defined in the home space with length h_s.

Measurement Error

Measurement data is affected by noise. To study the effect caused by noisy measurements, noise is sampled on top of the given reference light curve from the simulated measurements:

$$\tilde{\mathbf{L}} = \mathbf{L} + \nu, \tag{10}$$

When assuming optical observations with a CCD detector, the noise standard deviation is a mixture of various distributions [31], neglecting errors stemming from background estimation and ambiguous pixels:

$$\sigma_\nu = \sqrt{\mu_{\text{obj}} + \mu_{\text{noise}} + \sigma_{\text{U}}^2 + \sigma_{\text{read}}^2} \tag{11}$$

The signal of the object is best modeled as Poisson distribution, denoting the mean and variance as μ_{obj}. Celestial noise sources and detector dark noise are modeled as Poisson distributed with mean and variance μ_{noise}. The digitization error is uniformly distributed with a variance σ_{U}^2 and the read-out noise is a Gaussian distributed variable, with variance denoted by σ_{read}^2. It has to be noted that this is directly related to the quantity of signal to noise ratio on the image, defined as the mean of the signal over the standard deviation of the noise:

$$\text{SNR} = \frac{\mu_{\text{obj}}}{\sigma_\nu} \tag{12}$$

Using the central limit theorem, the combined distribution is modeled as a normally distributed variable $\nu \sim \mathcal{N}(0, \sigma_\nu^2)$ as a simplification in this paper with a fixed signal to noise ratio. Thus, it is the best possible scenario for the single inversion, for both, the cases on the single light curve (cases 1 and 2 outlined below) and also the case using the two light curves in a single inversion (the third case outlined below).

Multi-Hypothesis Approach: Hypothesis Creation and Best-Hypothesis Selection

For each measured light curve, only one sample of the distribution is available. As it will be shown in the next section, even small noise does have a significant impact on the shape inversion results because the problem is inherently under-determined. This means that the inversion is not a stable problem. In order to map out the possible solution space the noise is populated using a Monte Carlo approach. With an actual measured light curve, noise information can be readily extracted using the signal to noise ratio. As the sampling is of the noisy measurement rather than the true mean of the distribution, a bias is introduced that is neglected in this current approach. The bias is small and absorbed in the Gaussian assumption in the use of the central limit theorem. The different Monte Carlo samples are used to perform an inversion for each sample, leading to one final shape per sample. Those shapes are then treated as possible and equally weighted shape hypotheses. With a second, potentially much shorter second light curve, each shape hypothesis is then weighted. The second light curve is also affected by noise which is sampled in a similar fashion in order to compute the weights. The weights are computed based on the error between the noise-free light curve generated at the measurement period of the second light curve by the hypothesis shape, and the sample from the actually measured second light curve.

The comparison with the additional light curve is computed with all the shape hypotheses, as the solution of the Minkowski problem. Denoting $\mathbf{L}_{cand_j}$ as the light curve of the j-th hypothesis shape, and $\tilde{\mathbf{L}}_i$ as the i-th measurement sample from the noise sampled second light curve, the error per hypothesis shape from the first light curve and per sample from the second noisy light curve is determined as the absolute difference:

$$Error_{i,j} = |\tilde{\mathbf{L}}_j - \mathbf{L}_{cand_i}| \tag{13}$$

The weight w_j per j-th shape hypothesis is then computed as the inverse of the error combined over all n second light curve samples:

$$w_j = (Error_j)^{-1} = \left(\sum_i |Error_{i,j}| \right)^{-1} \tag{14}$$

The best hypothesis is the one with the highest weight. In the current application, two light curves are sufficient to generate selective weights. However, the methodology is easily extended for using additional light curves in case further data is needed to resolve closely related highest weight values.

As discussed above, in order to have sufficient observability, the number of observation has to be at least the number of facets on the EGI. As we see in the first case below, observability in those cases is not always ideal. The advantage of the hypothesis weighting is that the second light curve can be much shorter, not allowing for a full inversion itself, but still be used to compute weights. Secondly, as shown in the simulations below, the multi-hypothesis approach is outperforming a single inversion approach when taking all data of light curve one and two together in a single inversion. The reason is the under-determined nature of the inversion problem.

Simulation Result

Simulation Setup

Four simulation cases are presented to illustrate the effect of noise on the inversion and the performance of the multi-hypothesis method in comparison with a single inversion. All results use the reference objects of a cuboid (2 x 1 x 1 meter) and a house shape based off the cuboid shape with a roof height of 0.4 meters as shown in Fig. 1. A uniform Lambertian reflection of with a reflection coefficient $C_d = 0.8$ is assumed.

For all cases, an almost circular Medium Earth Orbit (MEO) at a height of 20000 km with a 40-degree inclination is used. In order to show the effect of observability of the object on the shape inversion, despite a seemingly sufficient amount of measurements (significantly larger than the number of EGI directions), two different attitude cases are studied. In the first case, the object spins about a space-fixed axis $(-0.95,1,0.11)$ at RPM of 2.2. This case is rank deficient (rank 282) [5, 6], because of the object attitude in combination with the observer geometry. For all other cases, three-axis torque-free motion with 30-degree nutation and 2.9 RPM precession rate is used. Full rank is reached for all these cases with the first light curve already [5, 6]. Standard orbit propagation techniques are used, including Earth spherical expansion up to degree and order 6, third body perturbations, and solar radiation pressure. Local horizon constraints, which limit the possible observation time intervals, were neglected but are easy enough to be incorporated. A second light curve is added in the third and the fourth case to act as an additional follow-up light curve measurement of the same object after one month. The second light curve has 100 observations less compared to the first one and they are not sufficient for an inversion by itself,

when using an EGI with 294 normal directions. Lower number of EGI directions are unable to even capture the simple shapes of house and cuboid in the noise free cases consistently. The setup of four simulation cases is summarized in Table 1. A constant SNR of 20 is also assumed. The measurement noise is sampled in a Monte Carlo approach. An illustration of the Monte Carlo noise sampling process for the second orbit is shown in Fig. 2, where the black dots are the collection of all the light curves with noise, and the red dots are the reference noiseless light curve, also representing the mean of the distribution in relative magnitude.

First Case: Circular Medium Earth Orbit, Simple Rotation about a Space Fixed Axis

Using the methodology described in Section "EGI Optimization Problem", as the first step in the inversion, the EGI is obtained. Two sampled results are presented

Table 1 Summary of the four simulation cases

1st case: simple rotation
- June-1-2018 0 AM to June-2-2018 0 AM
  - 350 observations evenly spread
- Spin about space fixed axis at 2.2 RPM
- 294 EGI directions
- Propagated orbit:
  - Circular Medium Earth Orbit
  - 6th order Earth spherical expansion
  - 3rd body perturbations
  - Solar radiation pressure

2nd case: three axis rotation
- June-1-2018 0 AM to June-2-2018 0 AM
  - 350 observations evenly spread
- 30° nutation, 2.9 RPM precession
- 294 EGI directions
- Propagated orbit:
  - Circular Medium Earth Orbit
  - 6th order Earth spherical expansion
  - 3rd body perturbations
  - Solar radiation pressure

3rd case: combined minimization
- June-1-2018 0 AM to June-2-2018 0 AM:
  - 350 observations evenly spread
- July-1-2018 0 AM to July-2-2018 4:10 AM:
  - 250 observations, 1 minute interval
- 30° Nutation, 2.9 RPM Precession
- 294 EGI directions
- Propagated Orbit:
  - Circular Medium Earth Orbit
  - 6th order Earth spherical expansion
  - 3rd body perturbations
  - Solar radiation pressure

4th case: N-by-m comparison
- June-1-2018 0 AM to June-2-2018 0 AM
  - 350 observations evenly spread
- 30° Nutation, 2.9 RPM Precession
- 294 EGI directions
- Propagated Orbit:
  - Circular Medium Earth Orbit
  - 6th order Earth spherical expansion
  - 3rd body perturbations
  - Solar radiation pressure
- N-by-m comparison:
  - Candidates from 2nd Case
  - July-1-2018 0 AM to July-2-2018 4:10 AM
  - 250 observations, 1 minute interval

Observer Location: New Mexico Skies Observatories, [32.903267,−105.529361]

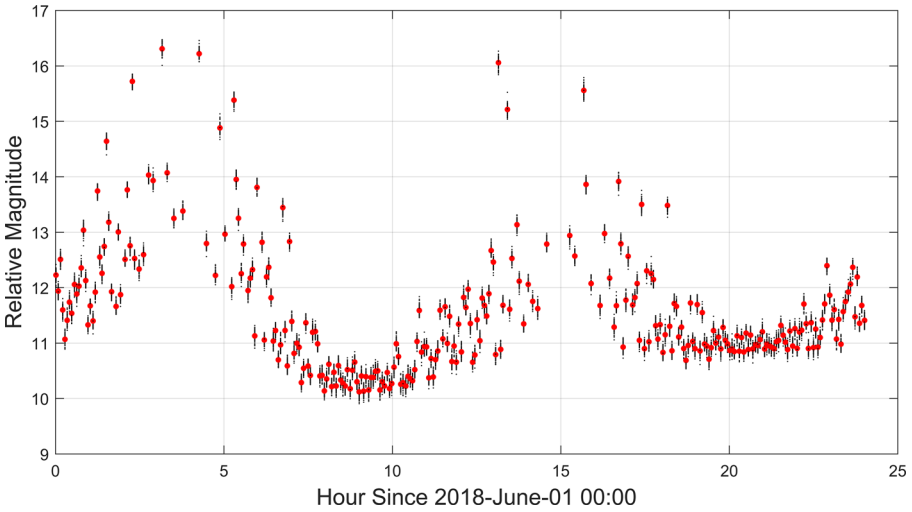

Fig. 2 Demonstration for noise sampling on reference light curve: Red dots: Reference light curve, Black dots: 100 noisy light curves sampled at SNR=20

here. Figs. 3 and 4 show the sampled cuboid and house inversion results, respectively. Figure 3a, c are the cuboid light curve comparison between the reference in red dots and the noise free light curve generated using the estimated EGI as input Fig. 3b, d. Figure 3b demonstrates the hand selected best output, matching the original EGI best, whereas Fig. 3d is the randomly selected sampled *average* output. It can be seen that the randomly selected ones, has significant area shifted to other normal

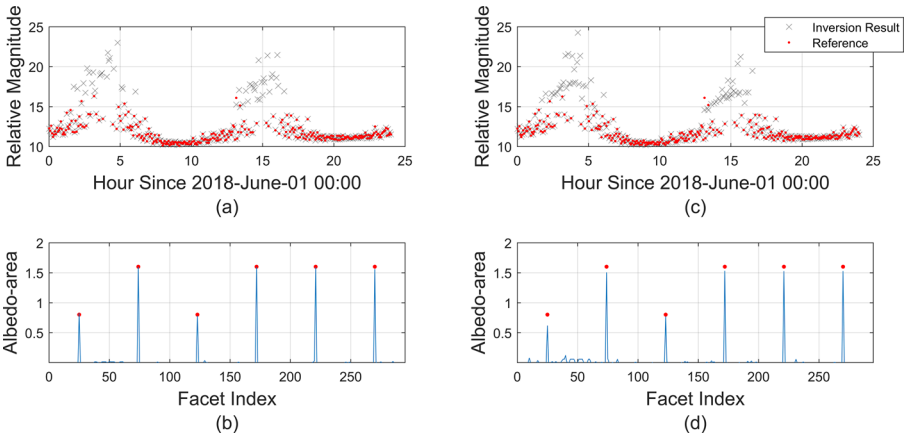

Fig. 3 EGI optimization result demonstration for the cuboid. Top row, noiseless perfect light curve in red and light curve generated from estimated EGIs in grey. Bottom row, areas associated with the normal directions. In red the truth, in blue the estimation results: **a** Best sample cuboid result light curve comparison, **b** Best sample cuboid EGI, **c** Random sample cuboid 1B (Fig. 6c, d) result light curve comparison, **d** Random sample cuboid 1B (Fig. 6c, d)

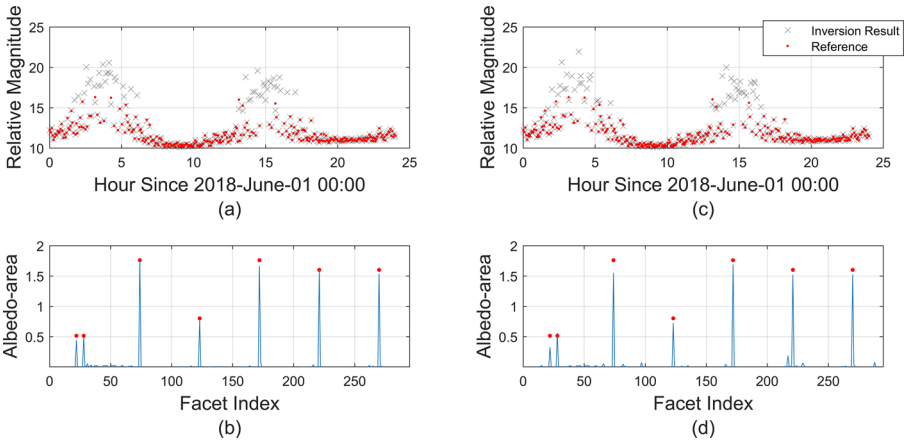

Fig. 4 EGI optimization result demonstration for the house. Top row, noiseless perfect light curve in red and light curve generated from estimated EGIs in grey. Bottom row, areas associated with the normal directions. In red the truth, in blue the estimation results: **a** Best sample house result light curve comparison, **b** Best sample house EGI, **c** Random sample house 1A (Fig. 6f) result light curve comparison, **d** Random sample house 1A (Fig. 6f) EGI. Truth in red dots

directions, and therefore missing area in the normal directions. The best sample is also not perfect but shows smaller deviations from the perfect solution.

Figure 4 show similar results for the house shape. We can observe in Fig. 3 that almost perfect results can be obtained which is not expected under close-to-full observability of all facets because the deficient rank entails some facets are never physically observed. The result for house shape is less accurate compare to the cuboid. It still captures all the facet normal directions correctly but with inaccurate area values.

Using 50000 samples populating the measurement noise, the Monte Carlo results for cuboid and house are illustrated in Fig. 5. Figure 5a, c show distributions of the direct geometric sum of all the elements in the EGI vector. The red dots show the reference values for the albedo-area sum. Figure 5b, d show distributions of the norm of the error between each EGI entry and the truth. It can be seen that the sum distribution is not close to Gaussian and the true values are far from both distributions. Interestingly, the albedo-area sum distribution for the cuboid is close to bimodal but converges to the same lump in its error distribution. This is most likely due to the symmetry of the cuboid. With the deficient matrix rank clearly degrades the optimization output. The spread of the distribution is significant. Therefore, distorted shape outcomes are expected for both, the house and cuboid shape.

Figure 6 shows several sampled shapes, completing the inversion process to solve for adjacency information after the EGI has been obtained. Table 2 shows values for the albedo-area sum and error for all the shapes shown in Fig. 6. The best cuboid result resembles very closely to Fig. 6a but it is not shown here specifically in order to closely illustrate another effect. Instead, what Fig. 6a, b show are two shapes that are derived from the same EGI (Fig. 3b). Similarly for Fig. 6c, d, both are derived from Fig. 3d. The existence of different shapes is a result of applying a different threshold

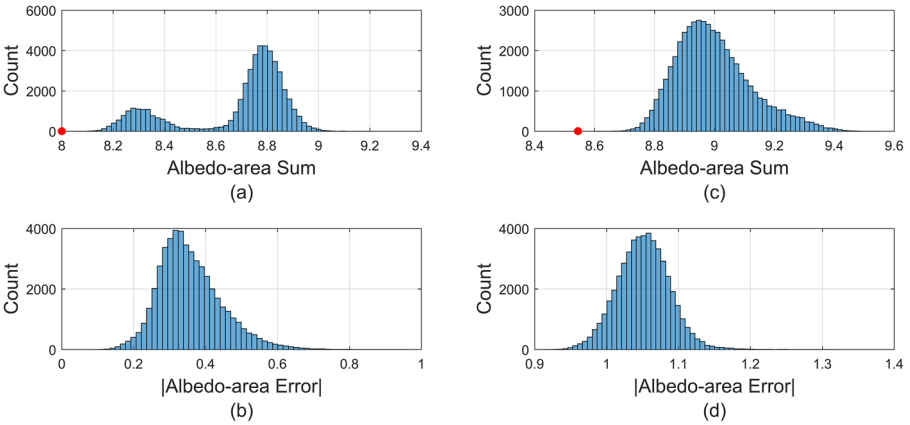

Fig. 5 Monte Carlo result from sampling the noise at SNR=20 and space-fixed axis rotation, 350 data points: **a** Cuboid albedo-area sum distribution, 50000 entries **b** Cuboid EGI error distribution, 50000 entries, **c** House albedo-area distribution, 23000 entries, **d** House EGI error distribution, 50000 entries; red dot indicates true albedo-area sum from reference shape

value on the EGI. Area values on the EGI below the threshold are ignored. This is often applied in asteroid shape inversion, suggested to reduce the effects of measurement noise. The threshold for one, *cleans up* the EGI, however also areas below the threshold are ignored, leading to a coarse inversion result. A low threshold, allowing for smaller true areas to be accurately captured, may lead to highly distorted results. For cuboid 1A, a very high threshold of 0.2 has been applied leading to an albedo-area error of 0.197 and cuboid 1A with 0.1 threshold can lead to unrecognizable shape by including more EGI entries; the shape constructed is not to scale here. It oversizes all the other results and if recalculated, the total surface area is several times larger than the sum of EGI entries in Fig. 3b. Currently, under the assumption of convex shapes, the use of a threshold only eliminates shape results that are clearly incorrect

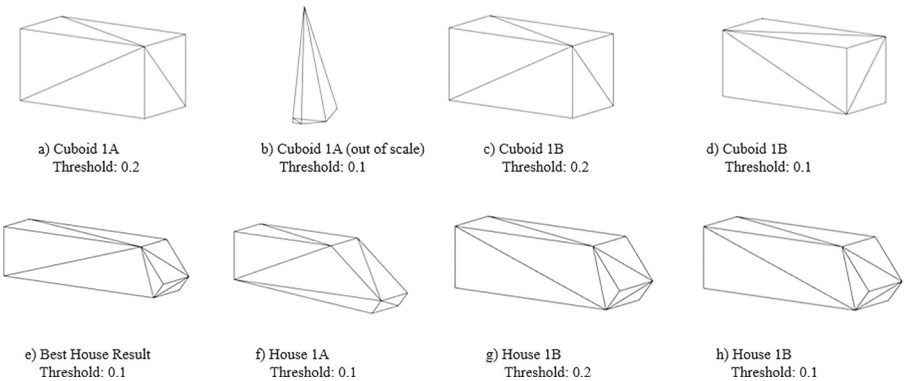

Fig. 6 Final shape retrieved for 1st case, **a**, **b**: Cuboid 1A with albedo-area error of 0.197, **c**, **d**: Cuboid 1B with albedo-area error of 0.368, **e**: Best house result with albedo-area error of 0.916, **f**: House 1A with albedo-area error of 1.059, **g**, **h**: House 1B with albedo-area error of 1.067

Table 2 Shape statistics for the first case

Shape (threshold)	Total Albedo-area	Albedo-area error
Cuboid 1A (0.2)	8.265	0.197
Cuboid 1A (0.1)	8.265	0.197
Cuboid 1B (0.2)	8.793	0.368
Cuboid 1B (0.1)	8.793	0.368
House 1A (0.1)	8.859	1.059
House 1B (0.2)	8.818	1.067
House 1B (0.1)	8.818	1.067

(can be checked by total surface area for example). When concavity is introduced, successful shape retrieval is expected for every EGI input. However, in Fig. 6g, h, both thresholds lead to comparable results. The problem is in selecting a threshold, *a priori* knowledge would be needed, to select a higher but correct threshold. In the cases here, the 0.2 threshold was handpicked to lead to the best results, whereas the 0.1 is preferred without *a priori* knowledge, only ignoring clearly distinct smallest features.

In comparing all shapes in Fig. 6, it should be noted that even with a large constant Gaussian sampled SNR setting of 20, seemingly small deviations in the EGI lead to resultant shapes with significantly different physical appearance (Fig. 6). Just to note, SNR 20 is by no means a high stress case, leading to clearly distinguishable object detections over the background of the image. However, the similar features shown in Fig. 6 also suggest that the human eye may also not be the best judge for resemblance in results, as even the only slightly distorted house shape of the best result result raises a significantly different impression to the human observer.

Second Case: Circular Medium Earth Orbit, Three Axis Rotation

The Monte Carlo results for the second case are shown in Fig. 7. Similar to the first case, the albedo-area sum and error values for all shapes in Fig. 8 are collected in Table 3. Compared to the first case, full rank condition on the G matrix is met via the more diverse attitude motion. The first observation is that the error in albedo-area is significantly lower by almost a full magnitude compared to the result from the first case; the cuboid as the simpler shape, has less overall error than the house shape. This means that the EGI results obtained for this case would be expected to be in better agreement with the true EGI, and consequently the final shape as well. However, it should also be noted, clearly visible in Fig. 7a,c that the mean of the albedo-area sum distribution is not coinciding with the truth. Next, a few EGI results were hand picked from the distribution including the least error result, to go through the Minkowski minimization and determine their shape appearance in the three dimensional space.

Figure 8 shows the shape outcomes for sampled cuboid and house EGI results. Due to the overall smaller error and shape simplicity, cuboid results are, in general,

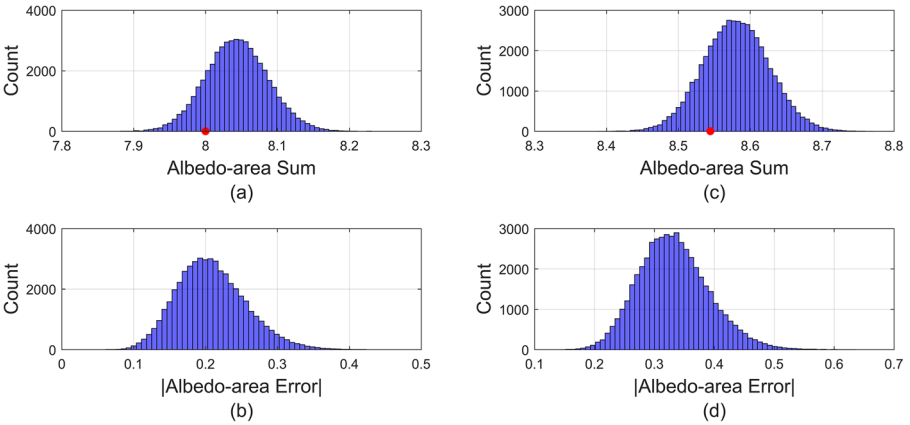

Fig. 7 Monte Carlo result from sampling the noise at SNR=20, 350 data points: **a** Cuboid albedo-area sum distribution, 50000 entries (mean: 8.044), **b** Cuboid EGI error distribution, 50000 entries, **c** House albedo-area sum distribution, 50000 entries (mean: 8.580), **b** House EGI error distribution, 50000 entries; red dot indicates true albedo-area sum from reference shape

closer to the original shape. For the house shape results, the roof feature for the house shape is distinct but not precise. It can be observed that the house shape results generally have elongated main body, where the truth should have been the same as the cuboid. This is mainly due to the shape reconstruction process. In order to form a closed shape with facet area as close to the input EGI area as possible, facet area deficiency is introduced in almost all cases. Figure 8g in particular also shows, that a high threshold of 0.2 is not a safe choice, even in the case of full rank G matrix and hence full observability. Figure 8h shows that being placed well in the middle of the error distribution, still leads to a significantly distorted shape with elongated body.

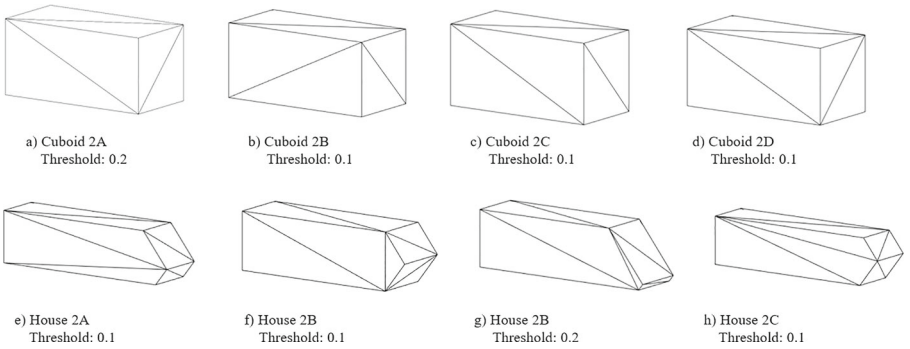

Fig. 8 Final shape retrieved for 2nd case, **a** Cuboid 2A with albedo-area error of 0.232, **b** Cuboid 2B with albedo-area error of 0.253, **c** Cuboid 2C with albedo-area error of 0.285, **d** Cuboid 2D with albedo-area error of 0.182, **e** House 2A with albedo-area error of 0.343, **f** House 2B with albedo-area error of 0.253, **g** House 2B with albedo-area error of 0.253, **h** House 2C with albedo-area error of 0.214

Table 3 Shape statistics for the 2nd case

Shape (threshold)	Total Albedo-area	Albedo-area error
Cuboid 2A (0.2)	7.947	0.232
Cuboid 2B (0.1)	7.982	0.253
Cuboid 2C (0.1)	8.010	0.285
Cuboid 2D (0.1)	8.029	0.182
ine House 2A (0.1)	8.636	0.343
House 2B (0.1)	8.642	0.253
House 2B (0.2)	8.642	0.253
House 2C (0.1)	8.597	0.214

Third Case: Circular Medium Earth Orbit, Three Axis Rotation, Combined Minimization Including the Second Light Curve

An extension from the second case is, when there are more observations available and the same inversion process is performed with the combined data set. In addition to the same 350 data points in the first light curve, a second set of brightness observations are made 30 days after the first. The second light curve includes 250 measurements with a one-minute interval spacing. The same EGI sampling number of 294 is used as before. As more measurements are available and full rank is already reached with the first set of measurements alone, improved results are expected compared to the first case.

In Fig. 9b, d, the albedo-area error distribution, the overall size of the error is smaller compared to the second case. Combining with the trend in the albedo-area

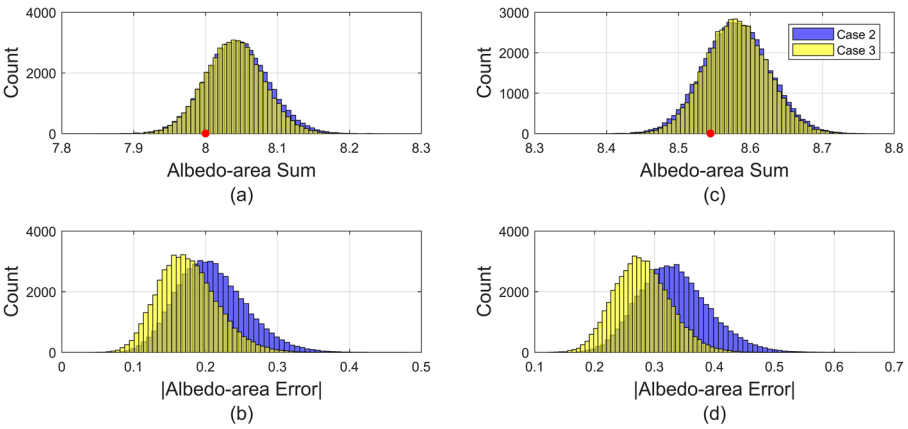

Fig. 9 Monte Carlo result from sampling the noise at SNR=20, 600 data points: **a** Cuboid albedo-area sum distribution, 50000 entries (mean: 8.040), **b** Cuboid EGI error distribution, 50000 entries, **c** House albedo-area sum distribution, 50000 entries (mean: 8.580), **d** House EGI error distribution, 50000 entries; red dot indicates true albedo-area sum from reference shape

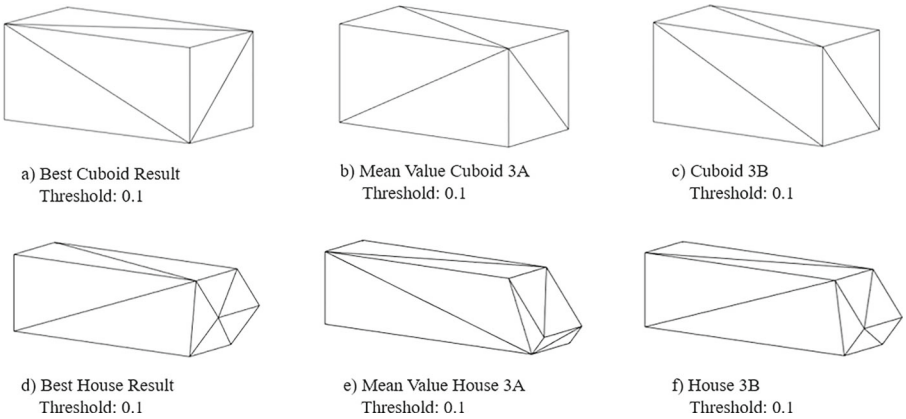

Fig. 10 Final shape retrieved for 3rd case, **a** Best cuboid result with albedo-area error of 0.048, **b** Mean value cuboid 3A with albedo-area error of 0.168, **c** Cuboid 3B with albedo-area error of 0.106, **d** Best house result with albedo-area error of 0.122, **e** Mean value house 3A with albedo-area error of 0.314, **f** House 3B with albedo-area error of 0.278

sum distribution, this means that the optimizer managed to associate the values in EGI area list better with its vector list when there is more data. However, it can be observed that the improvement of the albedo-area sum distribution results for both objects is minor, with almost the same mean and only minimally decreased standard deviation. It should be noted, that without the ground truth, only Fig. 9a,c (without the red truth dot) is available. As the distributions have not shifted, the true value still has a significant offset from the mean of the distribution.

As before, some selected shapes are illustrated in Fig. 10. The cuboid and house results are of similar quality than the ones in the second case. Despite the addition of the data, significant deviations from the true shape occur, most prominently with the non-primitive house shape. The best cuboid and house case, Fig. 10a, d are hand-selected. When computing the mean value of the albedo-area distribution, it leads to cases Fig. 10b, e, cuboid 3A and house 3A. When comparing both mean value EGIs in Table 4, both EGIs show a significantly larger albedo-area error than the best case. Shapes cuboid 3B and house 3B show the shapes for the bin next closest to the mean

Table 4 Shape statistics for the 3rd case

Shape (threshold)	Total Albedo-area	Albedo-area error
Best Cuboid 3rd Case (0.1)	8.061	0.048
Mean Value Cuboid 3A (0.1)	8.040	0.168
Cuboid 3B (0.1)	8.040	0.106
ine Best House 3rd Case (0.1)	8.588	0.122
Mean Value House 3A (0.1)	8.580	0.314
House 3B (0.1)	8.581	0.278

value, they also lead to a larger error value. For each of the sample results, the lower threshold has been used, that does not require *a priori* knowledge.

Fourth Case: Circular Medium Earth Orbit, Three Axis Rotation, Multi-Hypothesis Comparison Including the Second Light Curve

For this case, the multi-hypothesis methodology using two light curves has been performed. The shape hypotheses are formed based on the Monte Carlo samples of the first light curve consisting of 350 measurements, where a full inversion is performed for each sample (identical to the second case). The hypothesis are then one by one compared to each sample of the noisy second light curve, containing the 250 observations. Hence, the identical observations are used for the third and the fourth case. The weights are computed according to Eq. 14. This way, a single best hypothesis is selected.

110 Monte Carlo Samples were used in the second light curve, to populate its measurement noise. By summing up the error using Eq. 14 for each shape candidate, the specific cuboid (Fig. 11a) and house (Fig. 11b) are the highest weighted hypothesis. In the analysis it also turns out, that the hypothesis selection was very robust. The hypothesis with the next small weights in both cases, house and cuboid, were far off: if counting the number of individual light curves out of the 110 light curves, this specific cuboid candidate has the least error 52.3% of the time. The number is 100% for the best house shape candidate. Table 5 quantifies the quality of the best hypothesis shape for cuboid and house in comparison with the third case, where the same amount of data in a single inversion was used. In a real scenario, where the truth is unknown, shape 3As & 3Bs, representing the mean of the distribution, may be the shape of choice considering the sum of their EGI area entries lie at the mean and next closest to the mean of the albedo-area sum distribution (Cuboid 3A: 8.040, Cuboid 3B: 8.040, House 3A: 8.580, House 3B: 8.581), but Table 5 shows that the best hypothesis shape outperforms the mean value and next to mean value shapes in the previous cases in all (one tie) parameters including overall area error, maximum area error, the error in the direction of the normal directions (tie for the cuboid) and the distance in the support function absolute and relative. Overall, the worst parameter in shape inversion is naturally the distance to the area, or in other words the

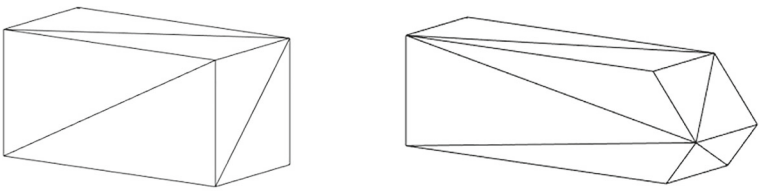

Fig. 11 Highest weighted shapes retrieved in the 4th case, **a** Highest weighted cuboid result using multi-hypothesis approach, **b** Highest weighted house result using multi-hypothesis approach

Table 5 Result statistics comparing to the truth

Best candidates	Area error (%)	Max area error (%)	Distance error (%)	Max distance error (%)	Max angle error (°)
	$\frac{\sum \lvert a_i - A_i \rvert}{\sum A_i}$	$\max \frac{\lvert a_i - A_i \rvert}{A_i}$	$\frac{\sum \lvert h_i - H_i \rvert}{n \sum H_i}$	$\max \frac{\lvert h_i - H_i \rvert}{H_i}$	$\max(h_i \cdot H_i)$
Best hypothesis cuboid 4th case	0.107	0.028	10.598	2.679	0.000
Mean value cuboid 3A	3.370	1.004	11.996	2.901	0.000
Next closest cuboid 3B	1.982	0.533	11.107	2.438	0.000
Best hypothesis house 4th case	8.557	2.814	14.520	2.671	14.768
Mean value house 3A	12.837	3.972	16.763	3.836	14.898
Next closest house 3B	13.362	4.252	18.537	3.798	18.843

support function error. The best shape hypothesis is for the cuboid just about 10 percent and for the house only 14.5 percent with a maximum error distance on a single support function for just 2.7 percent for both cases. The overall error can easily be decreased with higher Monte Carlo sampling in the first light curve.

Conclusions

This article showed a direct light curve inversion approach in the presence of measurement noise that is capable of robustly inverting given light curve observation data in order to retrieve shape. Its effectiveness under noise is studied. Two different shapes are used for the simulation, a cuboid, and a house shape. The shapes are assumed to be uniform Lambertian reflectors. In this study, two different attitude motion cases have been studied using the same medium Earth orbit: attitude motion that is either stable around the main inertia axis and a nutation attitude motion. The stable attitude case is rank deficient for the observation setup and resolution of the shape inversion result chosen. The nutation attitude motion leads to full rank condition in all of the cases. The noise is simulated with Gaussian white noise and constant high signal-to-noise ratio.

Two different scenarios are used. First the inversion results of a single light curve is studied, using Monte Carlo simulation to populate the noise of the light curve with samples. The process consists of first an optimization process to obtain Extended Gaussian Image, followed by a process solving Minkowski problem to obtain the shape for each of the samples. The research in this paper shows that in the presence of noise the inversion results from a single light curve can lead to highly distorted shapes. This is an indicator that the problem is highly sensitive to individual observation conditions. It has been shown that implementing a simple threshold to counteract the effect of measurement noise does not guarantee a good shape inversion result.

Two different scenarios have been investigated, using a shorter second light curve which is not sufficient to lead to a full rank shape inversion by itself. The first is the third case, the measurements of the first and second light curve have been combined and then used in a single inversion. While the absolute error in the albedo-area distribution in the Monte Carlo analysis decreased, the distribution in the albedo-area sum, which is available without knowledge of the ground truth, did not converge closer to the true solution. The second is the forth case, a multi-hypothesis scenario that has been developed in this paper is used: utilizing the first light curve to create sample hypothesis shapes, samples of the second noisy light curve are used to compute weights for the each of the aforementioned hypothesis shapes. In the investigated case, a clear highest weight is found. Comparing the mean in the albedo-area distribution and the second closest to the mean resultant shapes of the single inversion using the combined light curve data with the highest weighted hypothesis using the newly developed method, the latter clearly outperforms the former two in being significantly closer to the true shape. In absolute terms, the best hypothesis is very close to the true shape, with a maximum error of 10 percent for the cuboid and 15 percent for the house in area distances to the object center. The absolute error is only a function of the Monte Carlo sampling.

Acknowledgements This works was supported via AFOSR BAA Grant FA9550-18-1-0154 DEF.

References

1. Armstrong, J.T., Hindsley, R.B., Restaino, S.R., Benson, J.A., Hutter, D.J., Vrba, F.J., Zavala, R.T., Gregory, S.A., Schmitt, H.R.: Observations of a geosynchronous satellite with optical interferometry. In: Adaptive Coded Aperture Imaging, Non-Imaging, and Unconventional Imaging Sensor Systems, Volume 7468 of Proceedings of the SPIE, p. 74680K (2009)
2. Cowardin, H., Abercromby, K., Barker, E., Seitzer, P., Mulrooney, M., Schildknecht, T.: An assessment of GEO orbital debris photometric properties derived from laboratory-based measurements. In: Advanced Maui Optical and Space Surveillance Technologies Conference, p. E25 (2009)
3. Cowardin, H., Lederer, S., Liou, J.-C., Ojakangas, G., Mulrooney, M.: Optical signature analysis of tumbling rocket bodies via laboratory measurements. In: Advanced Maui Optical and Space Surveillance Technologies Conference, p. 61 (2012)
4. Eapen, R.T., Frueh, C.: Averaged solar radiation pressure modeling for high area-to- mass ratio objects in geosynchronous orbits. Adv. Space. Res. **62**(1), 127–141 (2018)
5. Friedman, A.M., Fan, S., Frueh, C.: Light curve inversion observability analysis. In: AIAA/AAS Astrodynamics Specialist Conference. AIAA Press (2019)
6. Friedman, A.M., Frueh, C.: Determining characteristics of artificial near-earth objects using observability analysis. Acta. Astronaut. **144**, 405–421 (2018)
7. Früh, C., Kelecy, T., Jah, M.: Coupled orbit-attitude dynamics of high area-to-mass ratio (hamr) objects: Influence of solar radiation pressure, earth's shadow and the visibility in light curves. Celest. Mech. Dyn. Astron. **117**(4), 385–404 (2013)
8. Furfaro, R., Linares, R., Gaylor, D., Jah, M., Walls, R.: Resident space object characterization and behavior understanding via machine learning and ontology-based Bayesian networks. In: Advanced Maui Optical and Space Surveillance Technologies Conference, p. 35 (2016)
9. Gaylor, D., Anderson, J.: Use of hierarchical mixtures of experts to detect resident space object attitude. In: Advanced Maui Optical and Space Surveillance Technologies Conference, p. E70 (2014)
10. Hall, D., Hamada, K., Kelecy, T., Kervin, P.: Satellite surface characterization from non-resolved multi-band optical observations. In: Advanced Maui Optical and Space Surveillance Technologies Conference, p. 24 (2012)
11. Hejduk, M.: Specular and diffuse components in spherical satellite photometric modeling. In: Advanced Maui optical and space surveillance technologies conference, p. E15 (2011)
12. Horn, B: Sequins and Quills Representations for Surface Topography AI Memo 536. Massachusetts Institute of Technology, Artificial Intelligence Laboratory (1979)
13. Kaasalainen, M.: Asteroid models from photometry and complementary data sources. In: American Institute of Physics Conference Series, Volume 1732 of American Institute of Physics Conference Series, p. 020003 (2016)
14. Kaasalainen, M., Lamberg, L., Lumme, K., Bowell, E.: Interpretation of lightcurves of atmosphereless bodies. I - General theory and new inversion schemes. A&A **259**, 318–332 (1992)
15. Kaasalainen, M., Torppa, J.: Optimization methods for asteroid lightcurve inversion. I shape determination. Icarus **153**, 24–36 (2001)
16. Kaasalainen, M., Torppa, J., Muinonen, K.: Optimization methods for asteroid lightcurve inversion. II the complete inverse problem. Icarus **153**, 37–51 (2001)
17. Kaasalainen, M., Torppa, J., Piironen, J.: Models of twenty asteroids from photometric data. Icarus **159**, 369–395 (2002)
18. Linares, R., Crassidis, J.: Dynamic observability analysis for attitude, angular velocity, shape, and surface parameters. In: 26th AAS/AIAA Space Flight Mechanics Meeting, pp. 2016–515 (2016)
19. Linares, R., Crassidis, J.L.: Space-object shape inversion via adaptive hamiltonian Markov chain Monte Carlo. J. Guid. Control Dyn, **41**(1), 47–58, 1 (2018)
20. Linares, R., Crassidis, J., Jah, M., Kim, H.: Astrometric and photometric data fusion for resident space object orbit, attitude, and shape determination via multiple-model adaptive estimation. In: AIAA Guidance, Navigation, and Control Conference, p. 8341 (2010)
21. Linares, R., Jah, M., Crassidis, J.: Inactive space object shape estimation via astrometric and photometric data fusion. Adv. Astronaut. Sci. **143**, 217–232, 01 (2012)

22. Linares, R., Jah, M., Crassidis, J., Leve, F.A., Kelecy, T.: Astrometric and photometric data fusion for inactive space object mass and area estimation. Acta. Astronaut. **99**, 1–15 (2014)
23. Little, J.J.: An iterative method for reconstructing convex polyhedra from extended gaussian images. In: Proceedings of the Third AAAI Conference on Artificial Intelligence, AAAI'83, pp. 247–250. AAAI Press (1983)
24. Little, J.J.: Extended gaussian images, mixed volumes, shape reconstruction. In: Proceedings of the First Annual Symposium on Computational Geometry, SCG '85, pp. 15–23. ACM, New York (1985)
25. Little, J.J.: Recovering Shape and Determining Attitude from Extended Gaussian Images. University of British Columbia, PhD thesis (1985)
26. Lynch, D., Russell, R., Rudy, R., Gutierrez, D., Turpin, M., Crawford, K., Dotan, Y., Kim, D., Skinner, M.: 3 - 13 μm spectra of geosynchronous satellites. In: The Advanced Maui Optical and Space Surveillance Technologies Conference, p. E81 (2006)
27. McMahon, J.W., Scheeres, D.J.: New solar radiation pressure force model for navigation. J. Guid. Control Dyn. **33**(5), 1418–1428 (2010)
28. Minkowski, H.: Allgemeine Lehrsätze über die konvexen Polyeder, pp. 121–139. Springer, Vienna (1989)
29. Minkowski, H.: Volumen und Oberfläche, pp. 146–192. Springer, Vienna (1989)
30. Payne, T.E., Gregory, S.A., Dentamaro, A., Ernst, M., Hollon, J., Kruchten, A., Chaudhary, A.B., Dao, P.D.: Development and evaluation of new methods for estimating albedo-area for stable GEOs. In: Advanced Maui Optical and Space Surveillance (AMOS) Technologies Conference, p. 24 (2017)
31. Sanson, C., Frueh, F.: Noise quantification in optical observations of resident space objects for probability of detection and likelihood. In: AIAA/AAS Astrodynamics Specialist Conference. AIAA Press (2016)
32. Schildknecht, T., Koshkin, N., Korobeinikova, E., Melikiants, S., Shakun, L., Strakhova, S., Linder, E., Silha, J., Hager, M.: Photometric monitoring of non-resolved space debris and databases of optical light curves. In; Advanced Maui Optical and Space Surveillance Technologies Conference, p. 25 (2015)
33. Schildknecht, T., Musci, R., Fruh, C.P., Color, M.: Photometry and light curve observations of space debris in GEO. In: Advanced Maui Optical and Space Surveillance Technologies Conference, p. E51 (2008)
34. Schildknecht, T., Vannanti, A., Krag, H., Erd, C.: Reflectance spectra of space debris in GEO. In: Advanced Maui Optical and Space Surveillance Technologies Conference, p. E24 (2009)
35. Scott, R., Wallace, B.: Satellite characterization using small aperture instruments at DRDC Ottawa. In: Advanced Maui Optical and Space Surveillance Technologies Conference, p. E36 (2008)
36. Seitzer, P., Abercromby, K., Barker, E., Rodriguez, H.: Optical studies of space debris at GEO - survey and follow-up with two telescopes. In: Advanced Maui Optical and Space Surveillance Technologies Conference, p. E37 (2007)
37. White, R.A., Stemwedel, S.W.: The quadrilateralized spherical cube and quad-tree for all sky data. In: Worrall, D.M., Biemesderfer, C., Barnes, J. (eds.) Astronomical Data Analysis Software and Systems I, vol. 25, p. 379. Astronomical Society of the Pacific Conference Series (1992)

MULTI-HYPOTHESIS LIGHT CURVE INVERSION SCHEME FOR CONVEX OBJECTS WITH MINIMAL OBSERVATIONS

S. Fan and C. Frueh

School of Aeronatuics and Astronautics, Purdue University, West Lafayette IN 47906, USA,
Email: {fan11, cfrueh}@purdue.edu

ABSTRACT

Knowing the exterior shape forms an important piece of information for space debris in the near-Earth region. It has been demonstrated in the past that the photometric measurements, also known as the light curve, contains the shape information. Previous work by the authors has established a shape estimation framework that is capable of generating high accuracy candidates for simple objects. For this work, an alternative multi-hypothesis framework is proposed based on a kind of particle filter using sequential importance resampling. Under realistic measurement noise setting, the simulation result has shown that likely candidates can be obtained up to satisfactory recognition with quantitative measure provided.

Keywords: Light Curve; Shape Estimation; Inversion Problem; Extended Gaussian Image; Multi-Hypothesis; Particle Filter; Convex Objects; Minkowski Problem.

1. INTRODUCTION

Traditionally, the orbit information (dynamic states) for objects in space has been of interest and it is obtained by solving the orbit determination problem. In recent years, it has been realized that knowing the exterior shape also forms an important piece of information, especially for space debris. The shape is coupled with the object's orbit via non-conservative forces, which is integral to orbital predictions as they pose a significant influence on Earth-orbiting human-made objects. Additionally, future missions involving close-up investigation of these objects have also promoted the necessity of characterizing their shapes.

Although RADAR system has been used to monitor space debris with good potential in resolution during direct imaging [7, 15]. Due to the relatively flexible deployment and robust operation, an effective way to observe the space debris population is the use of ground-based optical sensors.

Optical observation for objects in GEO has been conducted by Schildknecht et al. [17, 18], which brings awareness to the explosion events that happened in geostationary transfer orbits (GTO). Silha et al. [19] conducted a similar space debris survey in medium Earth orbits (MEO) and concluded that one uncorrelated object could be identified for every 100 minutes of observations. The National Aeronautics and Space Administration (NASA) and the Air Force Maui Optical and Supercomputing Site (AMOS) together conduct the debris measurement program focusing on the LEO and GEO region in both visible and infrared spectrum.

An information gathered during optical observation beyond the angular position, is the object's brightness. The so-called light curve refers to the change of brightness as a function of time. When the object is not illuminating by itself, the brightness is dependent on solar activity, orbits, attitude motion, exterior shape, material, atmosphere, and other attenuating factors. In the past, it has been shown that the shape information can be extracted from photometric measurements under assumptions [8, 10, 11, 12, 9].

At the scale of space debris, however, the measurement can be heavily influenced by noise given their sheer size, altitude, and reflection property. An approach that is capable of estimating shapes in this scenario is required. The authors had previously proposed using Monte Carlo simulation and a direct multi-hypothesis scheme to explore the solution space when assuming an object's orbit and attitude motion [4]. The main advantage of a multi-hypothesis framework is that it provides a conclusive statement on shape candidate's likelihood. In this article, particle filtering is implemented to sequentially update candidates while incorporating follow-up observations.

2. THEORY

This section first introduces the typical light curve inversion problem described by Kaasalainen et al. [10, 11], which takes observation data as input and produce a shape candidate as output after going through the two-step inversion process. The Monte Carlo noise sampling

$$\Lambda_{n-plate}(t_j) = \sum_{\lambda}\sum_{i=1}^{n}\frac{A_i}{\pi r_{topo,i,j}^2}(\hat{N}_{i,j}\cdot\hat{S}_{i,j})\mu'_{0,i,j}\left[C_{d,i}(\lambda)(\hat{N}_{i,j}\cdot\hat{O}_{i,j})+\pi\tau_{i,j}\beta_{i,j}\frac{C_{s,i}(\lambda)d_{Sun}^2}{a_{Sun,i,j}^2}\right] \quad (2)$$

$$\mu'_{0,i,j} = \begin{cases} 1, \text{ if } (\hat{N}_{i,j}\cdot\hat{O}_{i,j})\geq 0 \\ \quad \text{and } (\hat{N}_{i,j}\cdot\hat{S}_{i,j})\geq 0 \\ 0, \text{ else} \end{cases} \quad (3)$$

$$\tau_{0,i,j} = \begin{cases} 1, \text{ if } 1-\cos(0.25^{\text{o}}) \leq \frac{\hat{O}+\hat{S}}{|\hat{O}+\hat{S}|}\cdot\hat{N} \leq 1+\cos(0.25^{\text{o}}) \\ 0, \text{ else} \end{cases} \quad (4)$$

process which establishes the initial set of candidates, is then briefly explained. For a more detailed description of the method, the reader can refer to the previous publication by the authors [4]. Finally, the particle filter application is proposed along with detailed treatment on the Extended Gaussian Image (EGI). Part of the treatment leverages a quantitative measure that bounds the deviation among convex objects by Oliker and Frueh [16].

2.1. Light Curve Simulation

All light curves used in this article are simulated measurement. The simulation framework is proposed by the authors. The derivation and operation detail is described in [3]. A brief overview is provided here.

$$mag = m_{\text{Sun}} - 2.5log_{10}\Lambda \quad (1)$$

The unit of relative magnitude is used in this study and the absolute magnitude of the Sun m_{Sun} is taken to be -26.74. Λ is referred to as the phase function which refers to the ratio of brightness (in irradiation) between the object and the Sun. The phase function function can be computed in an finite-element fashion for convex objects as Equation 2.

Equation 2 sums through the surface of convex object and wavelength λ, at each time index j. The convex object is consisted of n number of facets, each with area A_i and unit normal vector $\hat{N}_i$. The Lambertian and specular reflection coefficient is denoted by C_d and C_s. The vector $\hat{S}$ and $\hat{O}$ points towards the Sun and the observer respectively. Coefficient β refers to the ratio of the Sun disk to the reflective surface. The distance between facet and the Sun is d_{Sun}, and Solar radius is a_{Sun}. The topological distance is given by r_{topo}. Lastly, the parameter μ'_0 and τ_0 refers to the illumination and specular reflection condition for each facet per time.

2.2. Two-Step Inversion Process

The basic light curve inversion problem starts with a least square minimization problem as Equation 5.

$$Min \quad J = |L-\mathbf{G}a|^2 \quad (5)$$

$$Subject\ to \quad a_i \geq 0, \quad i=1,...,m \quad (6)$$

Column vector L refers to the series of photometric measurements of the size l-by-1. It is also the input of the equation. The output of the problem is the column vector a of the size m-by-1. Each element of a represents the albedo-area value associated with a certain normal-facing direction, where the list of normal directions is pre-sampled thus known. When assuming full knowledge on orbits and attitude motion, $\mathbf{G}$ matrix (size l-by-m) can be computed with known normal facing directions. A minor assumption here is that the distance between the object center of mass and support location, is ignored as they form part of the shape information.

An important remark here lies on the observability, or the rank condition on the matrix $\mathbf{G}$. A full rank matrix guarantees a unique answer to the least square problem. For the shape estimation problem, however, the rank condition is dependent on the observation geometry, namely, the orbit and the attitude motion. If a side of the object is not observed, the albedo-area associated is subsequently not subject to data but other conditions (like constraints for example). Friedman et al. [5] has shown that it is possible to arrange an observation plan for the purpose of shape estimation such that it guarantees full observability. For preliminary studies using computer simulations, implementing torque-free motion often suffice.

After obtaining the albedo-area vector a and associating it with the list of pre-sampled normal vectors, it forms the so-called Extended Gaussian Image (EGI). The EGI is referred to as a shape descriptor, which describes a closed three-dimensional surface in an alternative space. In our case where a numerical process is performed and data is discrete, a discrete EGI is used to represent a polyhedron or a 3-dimensional polytope.

Under the assumption of uniformity, a convex object is represented uniquely by an EGI. Assuming an object to be convex, to obtain the shape in three-dimensional Euclidean space from the EGI input is referred to as the shape reconstruction process. The process can be summarized as first solving the EGI optimization problem to obtain the support, and perform half-space intersection to bound the dual object. The shape is finally retrieved after applying the dual transform. An important note here is its sensitivity. Theoretically, the EGI input has to satisfy the condition of closeness and convexity. If a small disturbance is present in the input, the reconstruction process will be forced to add a small piece of non-zero area fac-

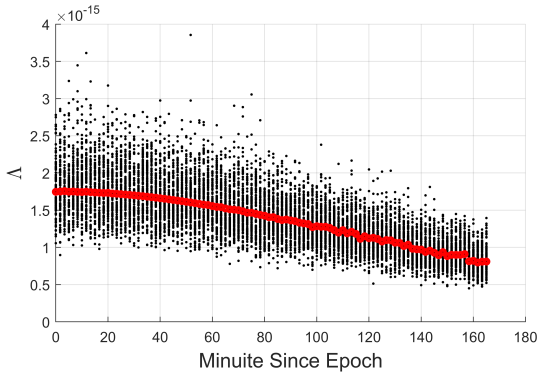

Figure 1. Demonstration of the noise sampling process, red dots: reference light curve simulated using setup from Section 3 on July-1-2018; black dots: 100 noisy light curves sampled at a signal-to-noise ratio of 5.

ing some direction and causes skewness to the result. A thresholding and smoothing stage can be added prior to this stage in order to reduce the problem's stiffness. They can are discussed in Section 2.4.

2.3. Monte Carlo Noise Sampling

When treating light curve data L as reference, noise can be sampled on top of the given data as the following.

$$\tilde{L} = L + \nu \tag{7}$$

For the scope of this article, noise ν is modeled as Gaussian noise with zero mean and constant standard deviation over all exposures. In reality, the noise will vary and is dependent on the signal itself. As noise is sampled and arbitrary number of noisy light curves are obtained, an equal number of EGIs are output by solving Equation 5. The noise sampling process is demonstrated in Figure 1

2.4. EGI Thresholding and Smoothing

For the least square problem (Equation 5) to be linearly independent, a full rank $\mathbf{G}$ matrix is ideal and the number of rows is greater than the number of columns, i.e. $l \leq m$. For non-trivial objects, one would expect there is a sufficient number of pre-sampled normal vectors such that the resolution of shape outcomes can be guaranteed. In practice, due to the discrete nature of the problem setup as well as different sources of noise, vector a will be obtained in a fashion that hardly has any zero entry. This poses a challenge for shape reconstruction as the process is highly sensitive to input.

Thresholding refers to the operation of discarding entries if they are below some fixed level. It is an effective way to suppress an overwhelming number of shape outcomes by focusing on the significant entries in vector a. It has to be emphasized that thresholding can be exercised at different levels of stringency during different operations. During the sequential importance resampling where the EGI is being constantly updated at each step according to new observations, the thresholding can be applied to include only the top 20 to 30 significant peaks for example. Whereas if there is a most likely EGI, a wider search would be more reasonable.

As mentioned in Section 2.2, the closeness and convexity condition is required for perfectly honest shape reconstruction. Since EGI lacks the information on support, it is difficult to perform a thorough check on the necessary conditions as far as the authors know. To reduce the stiffness when subject to input error, a smoothing stage is proposed as Equation 8 which aims to satisfy the necessary condition for closeness.

$$Min \qquad J = \| \sum_{i=1}^{m} \vec{n}_i (a_i + d_i) \| \tag{8}$$

$$Subject\ to \qquad 0 \leq d_i \leq u_i, \quad i = 1, ..., m \tag{9}$$

Equation 8 seeks the appropriate change in entries of vector a such that the expression is close to 0. The change in each entry is represented by d_i and it is bounded by upper limit u_i. The problem remains, as to if the post smoothing EGI is closer to the true EGI. However, the primary objective here is to let the reconstructed result honestly reflects the EGI input, at the cost of possibly losing some accuracy in terms of EGI.

2.5. C_2

Oliker and Frueh [16] proposed the following inequality to bound the deviation between two convex objects T_0 and T_1.

$$\sigma(\tilde{T}_0, \tilde{T}_1) \leq C\{\frac{V_1(T_0, T_1)}{V^{2/3}(T_0)V^{1/3}(T_1)} - 1\}^{1/3} \tag{10}$$

$$C = 2(\frac{R_0}{r_0})^2(\frac{R_0}{r_0} + \frac{R_1}{r_1}) \tag{11}$$

$$C_2 = C\{\frac{V_1(T_0, T_1)}{V^{2/3}(T_0)V^{1/3}(T_1)} - 1\}^{1/3} \tag{12}$$

The volume of T_0 is represented by $V(T_0)$ and $V_1(T_0, T_1)$ refers to the mixed volume of the two objects. R is the radius of smallest sphere that can enclose the object, and r is the radius of the largest sphere respectively. Here, the overall number on the right hand side is denoted by C_2. The quantity only bounds the difference and therefore should only be viewed as a general guideline.

2.6. Sequential Importance Resampling

From previous work [4], it has been established that shape estimation is possible for simpler objects with a

relatively lower number of EGI directions, thus observations. For more complex objects, as to be seen in Section 3, the size of vector a is required to be at least on the level of thousands. When examining the problem from an estimation point of view, particle filtering [2] was recognized as an option.

Conventional estimation filters like Kalman filter and Markov model, has the advantage of mathematical tractability when applying assumptions [20]. When the noise is non-Gaussian and the analytical model is not possible with high dimensionality, different estimation schemes were proposed. A class of method is called Sequential Monte Carlo (SMC) method [14]. The center idea is to draw samples from a predicted distribution before new observations become available. It is sometimes called a simulated-based method which has flexible implementation.

When it is not convenient to draw such samples, a classical method called the importance sampling can be used [6] which aims to translate between the so-called importance distribution and the posterior distribution. Lastly, resampling stage is often mentioned to avoid degeneracy and improve efficiency [14, 13, 1].

In this work, the method of sequential importance resampling is thought to be viable for two main reasons. The first is the problem's dimension. For arguably complex objects, thousands of albedo-area entries are to be found as mentioned above. Limited by the computation resources today, to directly sample these entries will not be possible. The second is the sheer complexity when creating samples of vector a directly.

In fact, the Monte Carlo noise sampling process already solves part of the problem by operating on the light curve and then optimize for the albedo-area vector. The white noise in Equation 7 can be viewed as equal likely perturbed light curves, and the EGI obtained will be of equal importance as well. This has to do with the difficulty of inverting the $\mathbf{G}$ matrix in essence, where the observation matrix is basically of inclusion.

Particle filtering is also capable of incorporating new observations and updating particles. Both features are important for the light curve inversion problem. The operation with particle filtering application is summarized in Figure 2.

The process is initialized with the same Monte Carlo noise sampling process described in Section 2.3 as step 1, where N candidate shapes (particles) with equal importance are produced. Note that one shape is constructed from one EGI and a corresponding threshold, this number is therefore caused by both the number of EGI from light curve optimization as well as the thresholding process. In case of new observation, full knowledge of the orbit and attitude motion is also assumed. The light curve can be predicted for each particle at the time and location of y_2. Then the sequential process can start to incorporate further follow-up observation. The operation is outlined as the following:

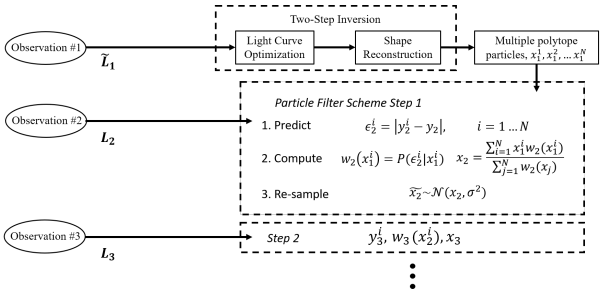

Figure 2. Sequential Importance Resampling Flow Chart

1. Particles from Monte Carlo noise sampling process, $x_1^1, \ldots x_1^N$.
2. Predict light curve at follow-up location for previous particles, $y_2^1, \ldots, y_2^N$.
3. Compare predicted light curve with the given follow-up light curve (y_2) and produce residue $\epsilon_2^1, \ldots, \epsilon_2^N$.
4. Compute residue distribution and fit non-parametric probability distribution function, and compute importance (likelihood) of each particle based on their residue in the distribution.

$$w_2(x_1^i) = P(\epsilon_2^i | x_1^i) \tag{13}$$

$$w_2^0 = \sum_{i=1}^{N} w_2(x_1^i) \tag{14}$$

5. After applying normalizing factor w_2^0, a single EGI candidate (x_2) will be formed through a weighted mean of all previous particles and their updated importance.

$$x_2 = \frac{1}{w_2^0} \sum_{i=1}^{N} w_2(x_1^i) x_1^i \tag{15}$$

6. Re-sample x_2 in each of the EGI direction by adding Gaussian noise (with some standard deviation up to user specification), and create a new set of particles, $x_2^1, \ldots x_2^M$.
7. Predict light curve at follow-up location for new particles, $y_3^1, \ldots, y_3^M$.
8. Go to step 3 and repeat the process for next follow-up observations $y_3, y_4, \ldots$, where M does not necessarily equal to N and varies at each iteration.

3. SIMULATION RESULTS

To demonstrate the effectiveness of the proposed method, a simulation scenario is established. An object is placed in orbit. Its light curve is simulated for the duration of the proposed observation period. The noise-affected light

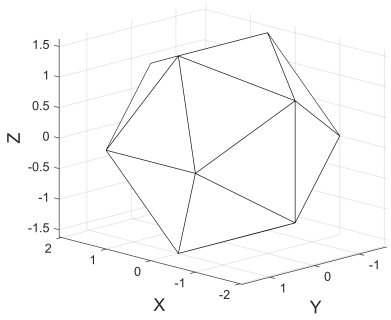

Figure 3. Icosahedron used for simulation, edge length: 2 m, surface area: 34.6 m^2

curve act as input to the inversion framework and the methodology is then carried out to examine the output.

A regular polyhedron of icosahedron is used which means the three-dimensional object consists of 20 identical faces. Each edge has a length of 2 m, and the total volume is 34.6 m^2. The object is assumed to have a uniform Lambertian reflection coefficient of 0.7 with specular component ignored.

A 60-degree inclined medium Earth orbit (MEO) at 20,000 km altitude is propagated. The first observation period is from June-1-2018 0 AM for 24 hours, 1350 evenly-spaced observations at a constant signal-to-noise (SNR) of 10 are assumed. The follow-up observation is set to take place a month later from July-1-2018 0 AM and lasts for 123 minutes. During this period, there are 5 sets of observations at a 10-minute separation from each other. Each set has 100 observations with a constant SNR of 5. A torque-free attitude motion is assumed which guarantees full observability. The ground observer is placed at the Purdue Optical Ground Station (POGS) located in New Mexico, USA.

Before demonstrating particle filtering, Figure 4 shows a collection of most likely EGIs. The reference EGI is plotted in red arrows. The 8 most likely EGIs are obtained by directly comparing with a noise sampled follow-up light curve (100 measurements at similar spacing) and the top 8 candidates with the least error are selected. Thus, all candidates are straight from the light curve optimization using the identical initial observation without any updating process.

It can be seen that only partial agreement is possible between candidate EGIs and the truth in terms of the density of arrows. Even with multiple follow-up noisy observations, the quality of individual candidate does not abet the characterization unless the information is combined in a meaningful way. Next, the update process with particle filtering is examined.

Figure 5 and Figure 6 shows candidates obtained after in-

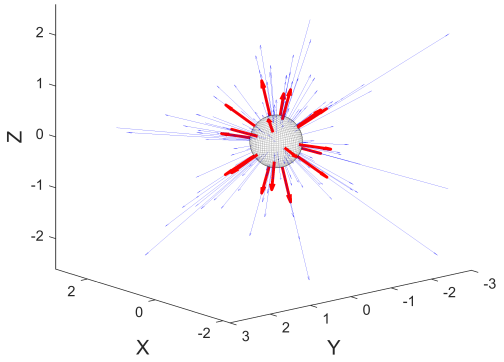

Figure 4. Simulation result after incorporating the first set of follow-up observation, 8 candidates (due to thresholding) are shown. C_2 value is computed with respect to the truth.

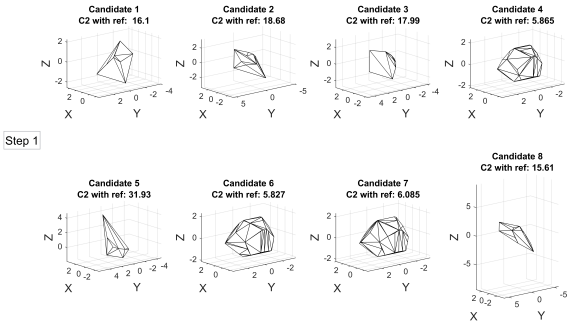

Figure 5. Simulation result after incorporating the first set of follow-up observation, 8 candidates (due to thresholding) are shown. C_2 value is computed with respect to the truth.

corporating the first and the fifth follow-up observation. Within the same figure, different shape candidates are constructed according to the same EGI at different thresholds, where the EGI leverages the proposed sequential importance resampling technique and therefore contains all the information up to the specific iteration.

Since C_2 is computed with respect to the truth, the quality of results is thus directly implied. Figure 6 shows that the list of candidates obtained in the last step is more likely to be closer to the truth. Several candidates also appear to be in the better aspect via visual inspection. In a real application, the knowledge about the truth can not be assumed. An alternative method is proposed here. That is for a specific likely EGI, to compute the C_2 value for each candidate with respect to all other candidates and form a matrix of C_2 values.

Table 1 prints an example C_2 table for all candidates shown in Figure 6. Note that candidate 3, 6, 7, and 8 coincide with the four shapes that have the lowest C_2 with respect to the reference. Here, a hypothesis which remains

Table 1. Example cross C_1 matrix printed according to the 8 candidates in Figure 6, rounding to decimal, colored column indicate likely candidates.

C_2	T_1	T_2	T_3	T_4	T_5	T_6	T_7	T_8
T_1	0.0	80.5	201.5	303.6	421.5	209.0	213.0	217.5
T_2	38.7	0.0	193.5	293.3	408.5	200.8	204.7	209.1
T_3	34.1	34.5	0.0	29.8	45.5	12.7	13.8	14.8
T_4	218.5	220.1	123.8	0.0	159.2	128.8	132.0	135.6
T_5	662.1	666.2	393.7	342.7	0.0	408.6	416.8	426.0
T_6	29.8	30.2	3.8	25.2	39.9	0.0	6.8	8.8
T_7	31.4	31.8	4.8	26.5	42.1	3.3	0.0	7.5
T_8	33.7	34.2	5.7	28.4	45.5	4.5	3.6	0.0

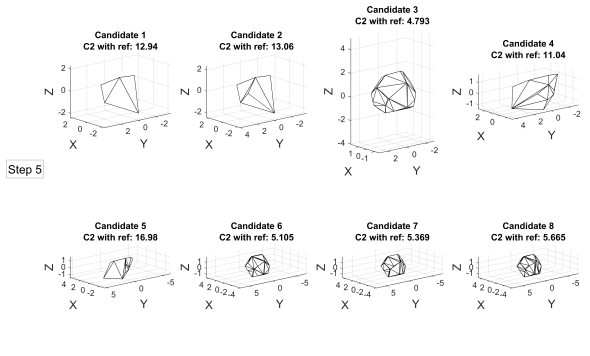

Figure 6. Simulation result after incorporating the fifth set of follow-up observation, 8 candidates (due to thresholding) are shown. C_2 value is computed with respect to the truth.

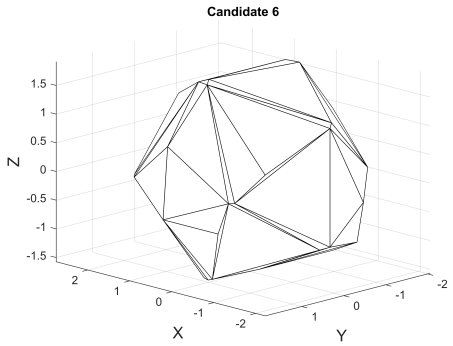

Figure 7. Best shape candidate after incorporating the fifth set of follow-up observation, selection according to C_2 matrix.

to be verified is that, a specific candidate that resembles closely to all other candidates is also the shape closest to the truth. For a more thorough investigation of a most likely candidate, the search is expanded to a wider range of thresholds. The final candidate is shown in Figure 7.

Since the order of convex objects does not commute for C_2 computation, the lower value should be used when comparing C_2 values between two objects. Among the four likely candidates, candidate 6 appears to be closer to all other candidates and is therefore selected as the winner.

4. CONCLUSION

A new light curve inversion method is proposed by applying particle filtering technique to the problem. Similar to the previous method proposed by the authors, the framework assumes no additional information on the object's shape beyond its orbit and attitude motion, and is capable of offering a quantitative conclusion on the candidate's likelihood. The new method, however, has the advantage of being sequential and updating candidates as new observations are being taken in. Based on the simulation results, the method is capable of outputting shape candidates up to satisfactory recognition, subject to noisy observations. Additionally, a selection criterion based on C_2 is proposed to further differentiate among candidates due to different thresholds.

ACKNOWLEDGMENTS

The work was supported via AFOSR BAA Grant FA9550-18-1-0154DEF.

REFERENCES

1. DOUCET, A. On sequential simulation-based methods for bayesian filtering.
2. DOUCET, A., AND JOHANSEN, A. M. A tutorial on particle filtering and smoothing: Fifteen years later. *Handbook of nonlinear filtering 12*, 656-704 (2009), 3.
3. FAN, S. The Light Curve Simulation and Its Inversion Problem for Human-Made Space Objects. Thesis.
4. FAN, S., AND FRUEH, C. A direct light curve inversion scheme in the presence of measurement noise. *The Journal of the Astronautical Sciences 67*, 2 (2020), 740–761.

5. FRIEDMAN, A., FAN, S., FRUEH, C., AND SCHILDKNECHT, T. Observability of light curve shape inversion based on optical data. In *First International Orbital Debris Conference* (2019).

6. GEWEKE, J. Bayesian inference in econometric models using monte carlo integration. *Econometrica: Journal of the Econometric Society* (1989), 1317–1339.

7. GOLDSTEIN, R., GOLDSTEIN, S., AND KESSLER, D. Radar observations of space debris. *Planetary and Space Science 46*, 8 (1998), 1007 – 1013.

8. HUDSON, R. S., AND OSTRO, S. J. Shape of asteroid 4769 castalia (1989 pb) from inversion of radar images. *Science 263*, 5149 (1994), 940–943.

9. KAASALAINEN, M. Asteroid models from photometry and complementary data sources. In *American Institute of Physics Conference Series* (May 2016), vol. 1732 of *American Institute of Physics Conference Series*, p. 020003.

10. KAASALAINEN, M., AND TORPPA, J. Optimization Methods for Asteroid Lightcurve Inversion. I. Shape Determination. *Icarus 153* (Sept. 2001), 24–36.

11. KAASALAINEN, M., TORPPA, J., AND MUINONEN, K. Optimization Methods for Asteroid Lightcurve Inversion. II. The Complete Inverse Problem. *Icarus 153* (Sept. 2001), 37–51.

12. KAASALAINEN, M., TORPPA, J., AND PIIRONEN, J. Models of Twenty Asteroids from Photometric Data. *Icarus 159* (Oct. 2002), 369–395.

13. KITAGAWA, G. Monte carlo filter and smoother for non-gaussian nonlinear state space models. *Journal of computational and graphical statistics 5*, 1 (1996), 1–25.

14. LIU, J. S., AND CHEN, R. Sequential monte carlo methods for dynamic systems. *Journal of the American statistical association 93*, 443 (1998), 1032–1044.

15. MORSELLI, A., DI LIZIA, P., BIANCHI, G., BORTOLOTTI, C., MONTEBUGNOLI, S., NALDI, G., PERINI, F., PUPILLO, G., ROMA, M., SCHIAFFINO, M., MATTANA, A., SALERNO, E., MAGRO, A., ADAMI, K. Z., ARMELLIN, R., SERGIUSTI, A. L., VILLADEI, W., DOLCE, F., REALI, M., AND PAOLI, J. A new high sensitivity radar sensor for space debris detection and accurate orbit determination. In *2015 IEEE Metrology for Aerospace (MetroAeroSpace)* (2015), pp. 562–567.

16. OLIKER, V., AND FRUEH, C. Stability of the Solution of the Minkowski Problem and its Application to Light Curve Inversion. in preparation.

17. SCHILDKNECHT, T., HUGENTOBLER, U., AND PLONER, M. Optical surveys of space debris in geo. *Advances in Space Research 23*, 1 (1999), 45 – 54.

18. SCHILDKNECHT, T., MUSCI, R., PLONER, M., BEUTLER, G., FLURY, W., KUUSELA, J., [DE LEON CRUZ], J., AND [DE FATIMA DOMINGUEZ PALMERO], L. Optical observations of space debris in geo and in highly-eccentric orbits. *Advances in Space Research 34*, 5 (2004), 901 – 911. Space Debris.

19. SILHA, J., SCHILDKNECHT, T., HINZE, A., FLOHRER, T., AND VANANTI, A. An optical survey for space debris on highly eccentric and inclined meo orbits. *Advances in space research 59*, 1 (2017), 181–192.

20. SMITH, A. *Sequential Monte Carlo methods in practice*. Springer Science & Business Media, 2013.

AAS 22-574

LIGHT CURVE INVERSION FOR RELIABLE SHAPE RECONSTRUCTION OF HUMAN-MADE SPACE OBJECTS

Liam Robinson [*], Carolin Frueh [†]

Characterizing unknown space objects is a growing field of study in Space Domain Awareness. Light curves, time histories of unresolved electro-optical brightness measurements, are one such tool used for characterization. If the attitude profile and material properties are known, an object's shape can be estimated through light curve inversion. We present advances in shadowing computation for light curve simulation and the robustness of convex shape inversion using the Extended Gaussian Image. These improvements are realized with standard tools from computer graphics and geometry processing. We also propose an extension to the inversion of simple non-convex objects using an error vector already available in the convex scheme. Good results are obtained for shapes with large and unilateral concavities.

INTRODUCTION

Characterizing unknown space objects is an essential capability for Space Domain Awareness. Object attitude, material properties, and shape hold actionable information for conjunction analysis, proximity operations, and long term orbit propagation. Collecting this information with minimal sensor utilization is of interest given the exponential increase in trackable space objects in recent years.[1] One efficient measurement for characterization is an object's light curve: a set of passive electro-optical brightness observations collected over time. A light curve is known to contain sufficient information to reconstruct prominent convex shape features.[2–8]

Light curve simulation methods differ between approaches and the object class under study. Kaasalainen and Torppa[3] employ a Lambertian model for convex objects with a facetwise ray tracing scheme for non-convex objects. Fan, Friedman, Kobayashi, and Frueh[2,4,9–11] use a nearly identical scheme for human-made objects. Allworth et al. developed a ray traced simulator for light curves in Blender, accounting for photorealistic shadowing and motion blur.[12,13] Many deep learning approaches including Furfaro et al.[14] and Cabrera and Bradley[5,15] use a simple Lambertian model with no self-shadowing. Linares and Crassidis[8] apply a more specialized approach with a non-Lambertian Bidirectional Reflectance Distribution Function (BRDF) for lighting. McNally et al.[16] use a Phong BRDF without shadowing, citing the computational intensity of shadow calculations. Blacketer[17] implemented a Cook-Torrance BRDF for lighting with a plane stacking method for self-shadowing.

Methods for shape inversion generally fall into one of three categories: Extended Gaussian Image (EGI), statistical estimation, and deep learning based methods. Each approaches the problem from a different perspective.

Direct light curve inversion with the EGI uses a series of optimization problems to fit a convex shape to measurements. These methods were pioneered by Kaasalainen and Torppa for asteroids in[3] with simultaneous attitude inversion in.[18] While natural space objects like asteroids are largely convex, nearly all human-made space objects are highly non-convex, highlighting the need for a robust inversion scheme for both convex and non-convex space objects. The work of Kaasalainen et al. was extended by Chng et al.[19] to find

[*]Undergraduate Student, Purdue University School of Aeronautics and Astronautics, robin502@purdue.edu
[†]Associate Professor, School of Aeronautics and Astronautics cfrueh@purdue.edu

globally optimal spin pole and area vector solutions for convex objects. Calef et al.[20] were early adopters of Kaasalainen and Torppa's EGI methods for human-made objects, focusing on multispectrum measurements. Bradley and Axelrad[15] applied EGI methods to recover convex approximations of representative GEO objects. Fan and Frueh[4,21,22] used the EGI with a multi-hypothesis scheme to recover human-made object shapes under measurement noise. Friedman[2,23] studied the observability of EGI inversion to inform sensor tasking schemes. Cabrera et al.[5] studied the effects of area regularization on Fan and Friedman's methods to achieve more accurate reconstructions.

A second approach leverages statistical estimation to retrieve shape information. Linares et al.[24] applied an unscented Kalman filter to estimate attitude and convex shape simultaneously, representing shape with vertex displacement on a sphere. Linares et al.[7] used a Multiple-Model Adaptive Estimation (MMAE) algorithm to predict the truth geometry and attitude by comparing observations with a bank of reference objects. Linares and Crassidis[8] used an Adaptive Hamiltonian Markov Chain Monte Carlo scheme to estimate shape and other characteristics simultaneously.

A third approach relies on deep learning. Linares and Furfaro[25] used a deep convolutional neural network to classify novel light curves as rocket bodies, payloads, or debris. Furfaro et al.[14] used similar methods classify novel light curves into four truth object classes. Kerr et al.[26] adapted the architecture developed by Furfaro et al. to classify object shape and size in an extended training set. McNally et al.[16] use AI and differential approaches to identify satellites from simulated and real light curves. Allworth et al.[13] applied transfer learning to simulated and real measurements to classify object type.

Various other unique methods have been applied to the light curve shape inversion problem. Hall et al.[27] investigated methods for independently solving shape parameters in isolation without attitude information. Fulcoly et al.[6] used measurements from different sensor locations to determine shape under various attitude profiles. Yanagisawa and Kurosaki[28] fit an analytical light curve model for a tri-axial ellipsoid to derive the shape and attitude profile of a Cosmos rocket body. Kobayashi applied compressed sensing to recover shape information from light curves by taking advantage of shadowing geometry.[10,29]

Shape inversion for non-convex objects — mainly asteroids — has been studied by others in the past. Durech and Kaasalainen[30] determined a relationship between concavity size and the minimum solar phase angle where self-shadowing impacts the light curve. Viikinkoski et al.[31] investigated recovering large concavities from adaptive optics imagery, noting the fundamental non-uniqueness of any solution. Notably, they discuss how a single large concavity may produce identical scattering behavior to multiple smaller concave features.[31] Cabrera et al.[5] studied convex solutions for non-convex objects, concluding that the convex fit diverges from the true shape as the relative concavity size increases.

We approach the shape inversion problem with the foundational EGI optimization and object reconstruction methods of.[3,4] The EGI optimization processes of[3–5] are improved using novel resampling and merging steps. These improvements circumvent the need for the regularization terms explored by Cabrera et al.[5] We also address the reconstruction scaling issues present in Fan's work[4] with an objective function proposed by Ikeuchi et al.[32] in place of Little's.[33] The support optimization procedure is accelerated and strengthened with a preconditioning term proposed for a different geometric optimization problem by Nicolet et al.,[34] enabling the rapid reconstruction of more detailed convex objects than previously feasible.

Our approach has a number of general advantages. We do not require *a priori* information about the truth geometry. Thus, unlike MMAE methods,[7] we do not require a bank of reference models to recover shape information. Unlike deep learning methods, our method does not rely on the diversity of a training set to achieve realistic results.[14,26] Our light curve simulation method improves on the facetwise ray traced shadows of[3,4,11] with shadow mapping, increasing shadow fidelity per unit computation time.

A procedure for detecting, locating, and creating large and unilateral concave features is proposed and implemented using an error vector determined in the EGI optimization process. This method is shown to be naturally compatible with the convex inversion scheme. Opposing or detailed concave features and variable optical properties will require more *a priori* information about the object of interest.

LIGHT CURVE SIMULATION

Extending the direct inversion schemes of[2,4,21] requires both accurate light curve simulation and reliable shape inversion algorithms. We rely on model-driven simulations to generate light curve data. In this way, the ground truth geometry is always known, isolating the accuracy of the reconstruction algorithm. Shape inversion from real-world data is out of the scope of this work due to complex atmospheric, optical, and sensor interactions that must be modeled.[4] Paradigms for light curve simulation can be separated into techniques for convex and non-convex objects, which we now consider in turn.

Convex Objects

Light curve simulation for convex geometry can be solved semi-analytically as the contribution of each facet to the measured irradiance can be computed individually.[3] Determining whether a face is illuminated requires two horizon checks to determine visibility from the Sun and to the observer. For a facet i at timestep j these horizon checks are expressed by the shadowing condition μ_{ij}.

$$\mu_{ij} = \begin{cases} 1 \text{ if } \left(\hat{O}_j \cdot \hat{n}_i\right) > 0 \text{ and } \left(\hat{S}_j \cdot \hat{n}_i\right) > 0 \text{ and } \delta_{ij,\text{ss}} = 0 \text{ and } \delta_{ij,\text{os}} = 0 \\ 0 \text{ otherwise} \end{cases} \tag{1}$$

The unit vectors $\hat{O}$ and $\hat{S}$ point from the center of mass of the object to the observer and Sun, respectively. We choose the outward-pointing facet normal unit vector $\hat{n}$ for all mesh operations. The self-shadowing and observer-shadowing conditions, $\delta_{ij,\text{ss}}$ and $\delta_{ij,\text{os}}$, are always zero for convex polyhedra but are crucial for accurately simulating non-convex geometry. For objects with concavities, self-shadowing refers to shadows cast by an object onto itself and observer-shadowing refers to otherwise visible faces blocked by other portions of the geometry.

The irradiance I received by the observer at timestep j is the sum of the received irradiance from all facets, composed of specular and diffuse contributions. We express each contribution as the product of the light curve function L — the received irradiance per unit incident irradiance — multiplied by the Sun's irradiance at the object's position, nominally $I_{\text{Sun}} = 1361\ \text{W/m}^2$ at 1 AU.

$$I_j = I_{\text{Sun}} \left(L_{j,\text{diffuse}} + L_{j,\text{specular}}\right) \tag{2}$$

The diffuse component is expressed as:

$$L_{j,\text{diffuse}} = \sum_{i=1}^{m} \frac{\mu_{ij} C_{d,i} A_i}{\pi r_j^2} \left(\hat{O}_j \cdot \hat{n}_i\right) \left(\hat{S}_j \cdot \hat{n}_i\right). \tag{3}$$

In Eq. 3, r_j is the Euclidean distance from the observer to the object center of mass at time j. Each facet i has area A_i and diffuse reflection coefficient $C_{d,i}$. If specular effects are taken into account, the contribution to the light curve function is represented:

$$L_{j,\text{specular}} = \sum_{i=1}^{m} \frac{\nu_{ij} C_{s,i} A_i}{\pi r_j^2} \left(\hat{S}_j \cdot \hat{n}_i\right) \frac{d_{j,\text{Sun}}^2}{a_{\text{Sun}}^2}. \tag{4}$$

The term $\frac{d_{j,\text{Sun}}^2}{a_{\text{Sun}}^2}$ in Eq. 4 accounts for the relative angular size of the Sun's disk, with C_s representing the specular reflection coefficient.[4] The specular glint condition ν_{ij} for facet i at timestep j is defined for a glint offset angle of γ, commonly approximated as $0.25°$.[4] Note that $\hat{R}_{ij}$ is the normalized reflected Sun vector, where $\vec{R}_{ij} = 2\left(\hat{n}_i \cdot S_j\right)\hat{n}_i - \hat{S}_j$.

$$\nu_{ij} = \begin{cases} 1 \text{ if } |\hat{R}_{ij} \cdot \hat{O}_j| < \cos\gamma \\ 0 \text{ otherwise} \end{cases} \tag{5}$$

This work uses a uniform diffuse reflection model with $C_d = 1$ and $C_s = 0$ for ease of simulation. Forfeiting specular effects makes shape inversion more challenging as glints contain precise information about facet orientation. A BRDF may be implemented in the future for more realistic rendering.

Non-Convex Objects

Many existing light curve simulation methods for non-convex objects rely on ray tracing schemes like Möller and Trumbore's ray-triangle intersection algorithm.[4,35] This computation is necessarily complex as there may be significant self-shadowing at large phase angles. As a result, we cannot assume $\delta_{ij,\text{ss}} = 0$ and $\delta_{ij,\text{os}} = 0$.[4,11] In the absense of a bounding volume hierarchy or other techniques to reduce the number of rays cast, ray traced shadows generally require $\mathcal{O}(n^2)$ ray-triangle intersections per timestep for n facets. For this reason, facetwise ray traced shadows quickly become infeasible for complex reference geometries without GPU parallelization. The limitations of ray-triangle intersections for light curve simulation is discussed at length by Frueh et al in.[11]

For faster and more accurate simulated light curves, we use shadow mapping computed on the GPU. Shadow mapping is a well understood, if dated, technique in computer graphics.[36] Although modern ray traced shadowing may be more computationally efficient, shadow mapping was selected for its ease of implementation, once the inherent aliasing or 'shadow acne' was addressed using standard remedies.[36] Because shadow mapping shades individual pixel fragments instead of entire facets, it offers increasing shadow quality over facetwise ray tracing as the number of mesh faces falls.

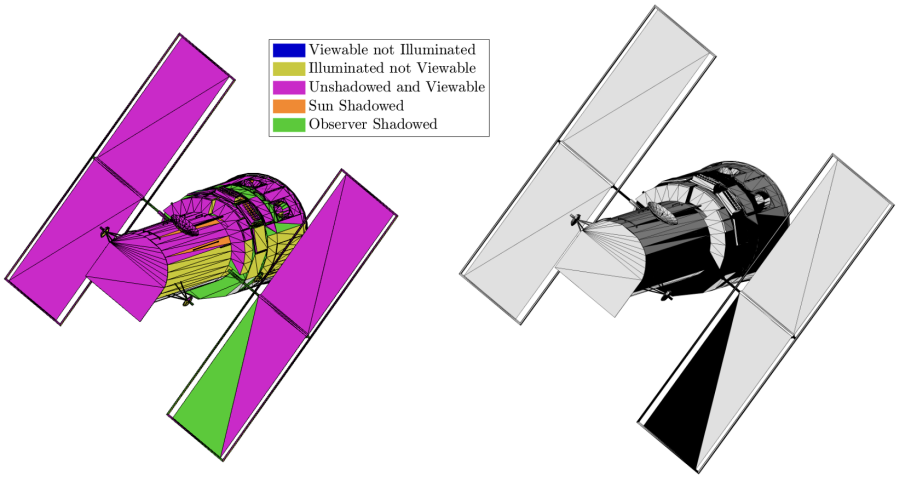

Figure 1. Hubble Space Telescope ray traced shadow categorization and shading. Models from[37]

Importance of Self-Shadowing for Human-Made Objects

To motivate the importance of accurate shadowing computation for human-made space objects, consider the error introduced by neglecting shadows for different types of objects. Kaasalainen and Torppa's work on asteroids reasonably assumed that shadowing was a negligible contribution to the measured light curve. Human-made objects do not afford the same luxury. Figure 2 displays light curves for the asteroid Bennu and the Hubble Space Telescope with and without accurate shadows under a single-axis attitude profile with inertially fixed Sun and observer vectors. Without accurate shadowing, the light curve's magnitude and time derivatives are both dramatically effected. The normalized light curve in Figure 2 is simply Eq. 2 with $r = 1\text{m}$

and $I_{\text{Sun}} = 1\,\text{W}/\text{m}^2$. Doing so preserves the information content of the light curve without introducing biases due to specific orbital geometries.

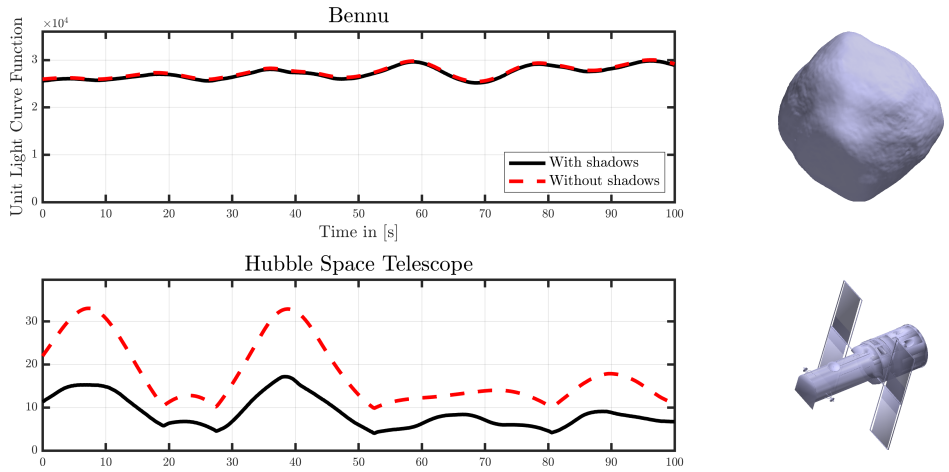

Figure 2. Errors introduced by neglecting shadows for Bennu and HST. Models from[37]

Shadow Mapping for Light Curve Simulation

Given an observer and Sun vector in the body frame of the object, shadow mapping proceeds in a four step process. In step one, a camera is positioned along the Sun vector and a perpendicular depth texture is computed. In the second step, depth values in Sun camera space are transformed to observer camera space, forming a second depth texture. This second texture is used to find the closest fragment along each ray to the Sun, determining the self-shadowing condition.[38] Self-shadowed fragments are classified as those further from the Sun than the closest fragment along the same ray, indicated in red in Figure 3. Fragments that do not pass the convex shadowing condition are horizon shadowed, indicated in blue in Figure 3. All remaining fragments are shaded with using the same Lambertian reflection model in 3. Computing the light curve function for the final rendered image requires summing all pixel values and dimensionalizing the result by the observer camera's field of view area and the current distance to the observer. The light curve simulation environment used in this work was implemented in C and OpenGL with the raylib library.[39]

LIGHT CURVE INVERSION

Traditionally, direct light curve inversion involves two distinct steps: a linear batch least squares problem to fit an EGI to the measured light curve, and a second optimization to produce accurate vertex positions and face adjacency information.[4] The first step uses data-driven estimation to yield a valid and accurate EGI through a linear optimization. The second step is highly nonlinear and scales badly with facet count and geometric asymmetry, as discussed by Fan in.[21]

The Extended Gaussian Image

The discrete EGI $\vec{E} \in \mathbb{R}^{m\times 3}$ is composed of m unit vectors $\hat{n}$ by nonnegative scalars $a \in \mathbb{R},\ a_i \geq 0$.[40]

$$\vec{E}_i = a_i \hat{n}_i \tag{6}$$

In the context of shape inversion, we choose the m vectors $\hat{n}$ to be a tessellation on the unit sphere as we have no knowledge of the true facet normal orientations in the body frame. A convex polytope can be uniquely represented by an EGI of facet normal vectors scaled by each facet's area. The set of normal vectors in an EGI is denoted $\mathcal{N}$ with the set of areas denoted $\mathcal{A}$. The vector of facet areas is denoted $\vec{a} \in \mathbb{R}^{m\times 1}$. In this paper, we take the norm of the EGI to be $\|\vec{E}\| = \sum \vec{a}$ with the 'size' of the EGI $|\vec{E}| = m$.

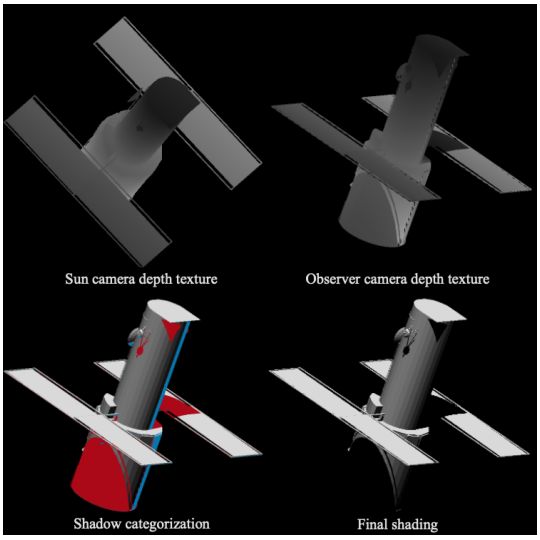

Figure 3. Hubble Space Telescope shadow mapping with self (red) and horizon (blue) shadows rendered. Models from[37]

The solution to the Minkowski problem proves the existence and uniqueness of a convex polytope for an EGI that satisfies the closure condition in Eq. 7.[41] Equivalently, an EGI uniquely represents a closed, convex polyhedron — a polytope — with no open boundaries, up to a translation.

$$\sum_{i=1}^{m} \vec{a}_i \hat{n}_i = [0, 0, 0] \tag{7}$$

While a given EGI uniquely represents a polytope, it is shared by an infinite number of non-convex and open geometries. An example of this extended family is depicted in Figure 4 where larger circles indicate greater relative areas assigned to a given normal vector.

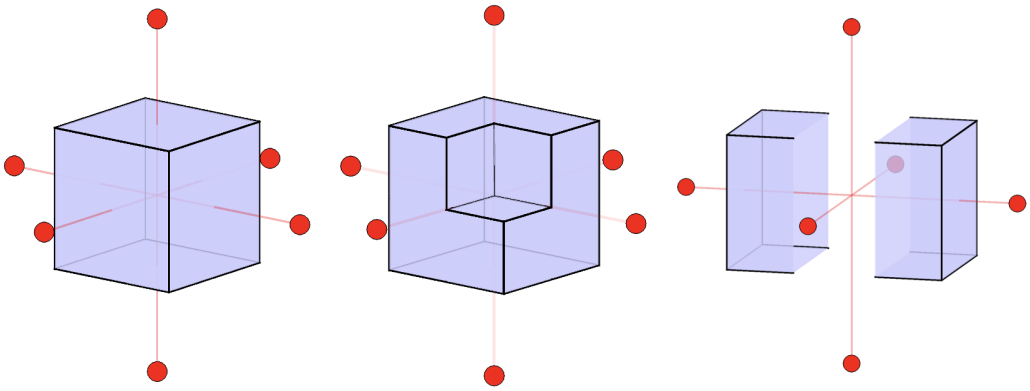

Figure 4. Simplified convex, non-convex, and open EGI nonuniqueness

EGI Optimization

The EGI fulfills two important criteria when applied to light curve inversion: it can be estimated directly from the light curve, attitude profile, and material properties, and uniquely represents a convex object.[3] Fur-

thermore, convex geometry can be reconstructed from the EGI and vice versa through computing the dual transform[33] and solving the Minkowski problem.[41]

Once a light curve is obtained, direct shape inversion schemes sample m candidate normal vectors $\hat{n}$ on the unit sphere to fit an EGI to the observed light curve $\vec{L}_{\text{ref}} \in \mathbb{R}^{n\times 1}$.[2,4] This is accomplished by solving an optimization problem to distribute the area vector $\vec{a}$ across the sampled normals to minimize the residual between the observed and modeled light curves. In practice, this is a constrained nonnegative least squares problem and can be solved efficiently for large numbers of normal vectors and light curve data points:

$$\min_{\vec{a}} \|\vec{L}_{\text{ref}} - G\vec{a}\|_2 \quad \text{subject to } \vec{a}_i \geq 0, \sum_{i=1}^{m} \vec{a}_i \hat{n}_i = [0,0,0]. \tag{8}$$

It is important to note that the area estimated with Eq. 8 is necessarily *albedo-area* due to the diffuse reflectivity coefficient C_d in Eq. 3. If the value of C_d is uniform but unknown, the recovered geometry will incorrectly scaled without impacting the face adjacency or relative feature sizes.

The convex reflection matrix $G \in \mathbb{R}^{n\times m}$ with ijth entries $[g]_{ij}$ defined at time i for each facet j is defined as the normalized received facet irradiance per unit facet area:

$$[g]_{ij} = \frac{I_{ij}}{I_{\text{Sun}} a_j}. \tag{9}$$

The facetwise contribution I_{ij} may be computed with a combination of diffuse and specular components as in Eq. 3 and Eq. 4 or a BRDF. This relationship between the object irradiance and area defines the normalized convex light curve $\vec{L}_{\text{convex}}$, that produced by a convex object of facet areas $\vec{a}$ under the attitude profile and lighting conditions that yield G.

$$\vec{L}_{\text{convex}} = G\vec{a} \tag{10}$$

EGI Optimization Results

The optimization in Eq. 8 produces a coarse approximation of the true EGI as m is finite. Increasing m necessarily improves the quality and sparsity of the estimated EGI, but at the cost of computational resources. The estimation was performed using a synthetic light curve input from $n = 500$ Sun and observer vectors uniformly sampled on the sphere in the body frame, producing a full rank G matrix. $m = 500$ candidate normal vectors were sampled using a spherical Fibbonaci mapping described by Keinert et al. in.[42] Results are visualized for an icosahedron in the body frame in Figure 5. Reconstructing the object at this stage is difficult due to the quantity of faces present in the estimated EGI.

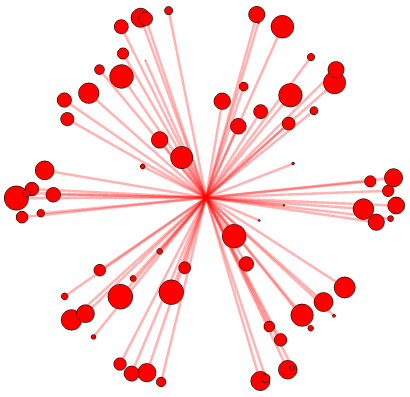

Figure 5. Initial icosahedron EGI optimization before resampling

EGI Resampling

We propose a normal vector resampling step to promote a more accurate and sparse EGI. The normal vectors used in Eq. 5 are generally correct, with each group clustering around a normal vector of the truth geometry. This clustering behavior occurs when none of the candidate normal vectors are sufficiently close to the truth. Resampling in a cone centered on each initial EGI normal vector provides more accurate candidates for EGI estimation. This process mimics a single optimization step with a much larger m, where the coarse EGI is used to exclude areas on the sphere with little or no normal area.

Uniformly sampling a cone of half-angle ϕ is accomplished by strategically sampling points on the unit sphere.

$$\hat{n}_{cone} = \begin{bmatrix} \sqrt{1-z^2}\cos\theta \\ \sqrt{1-z^2}\sin\theta \\ z \end{bmatrix} \tag{11}$$

In Eq. 11 we choose two coordinates $z \in [\cos\phi, 1]$ and $\theta \in [0, 2\pi)$, yielding a point uniformly distributed on a cone of half-angle ϕ about the central axis $[0, 0, 1]^T$.[43] These points are then rotated using a direction cosine matrix to center the cone on an axis of interest.

The number of new candidates sampled per initial solution vector and the cone half-angle should be adjusted on a case-by-case basis depending on the compute power available and the observability of the problem as discussed by Friedman in.[2]

EGI Resampling Results

Existing EGI optimization schemes like those of Fan,[4] Friedman,[2] and Cabrera[5] are limited by a single normal vector sampling step, leading to a lack of accuracy and sparsity in the optimized EGI. High-density normal vector sampling in regions known to contain non-zero area leads to EGI solutions that are generally more sparse and cluster more tightly about true normal vectors.

This process is shown in Figure 6 for the same icosahedron with a half-angle $\phi = \frac{\pi}{20}$ and sampling density of 50 candidate vectors per cone.

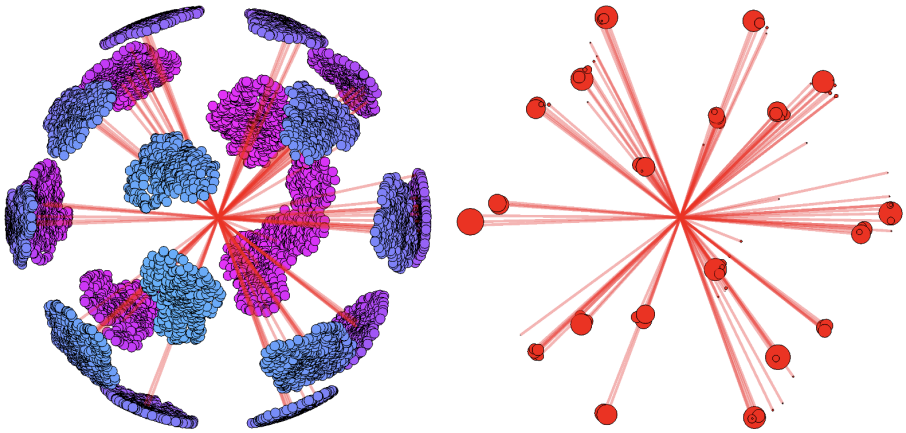

Figure 6. Resampled normal vectors (left) with reoptimized EGI (right)

EGI Merging

After resampling and reoptimizing with Eq. 8, the reestimated EGI is merged by computing all groups $\mathcal{G}$ of EGI vectors within an angular offset α:

$$\mathcal{G}_k = \left\{ \vec{E}_i \in \vec{E} \,|\, \cos^{-1}\left(\frac{\hat{E}_i \cdot \hat{E}_k}{|\vec{E}_i||\vec{E}_k|} \right) < \alpha \right\}. \tag{12}$$

Groups are merged by summing all group members, yielding a single EGI vector $\vec{E}_m$ without loss of total area or closure.

$$\vec{E}_m = \sum_{\vec{E} \in \mathcal{G}_k} \vec{E} \tag{13}$$

In practice, the choice of α is dependent on the user's tolerance for discretization, as merging will approximate smooth geometry by discrete faces with normal vectors offset by 2α.

EGI Merging Results

Merging the resampled EGI using Figure 6 with $\alpha = \frac{\pi}{10}$ produces a final sparse EGI fit for object reconstruction, shown in Figure 7.

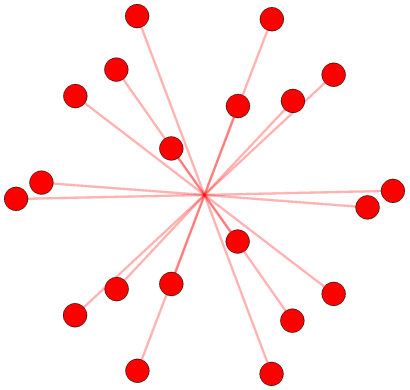

Figure 7. Merged icosahedron EGI

Convex Geometry Recovery from the EGI

At this stage, we have recovered a sparse EGI representing a convex approximation of the underlying object with no guarantee of the closure of this EGI. The EGI closure constraint Eq. 7 motivates a simple procedure to correct an invalid EGI by adding the mean closure error to each entry:

$$\vec{E}_{\text{closed}} = \vec{E}_{\text{open}} - \sum_{i=1}^{m} a_i \hat{n}_i. \tag{14}$$

This step is not a novel contribution. Fan used a more complex optimization problem to adjust the EGI towards closure.[4] We improve on that process with a simpler analytical correction. In practice, this process should be performed before each reconstruction to accelerate convergence. Failing to correct non-closed EGIs will cause convergence to a nonzero minimum in the reconstruction objective function as there is no corresponding convex object with the given EGI.

The unique convex object encoded by each closed EGI is reconstructed by solving for the polytope's set of vertices $\mathcal{V}$ and faces $\mathcal{F}$ encoding the adjacency relations between vertices. This is accomplished following the procedure introduced by Little in[40] through the dual transformation. The dual set $\mathcal{D}$ are vertices in $(A, B, C) \in \mathbb{R}^3$ that satisfy the following plane condition for a point (x, y, z) on each facet of the object:

$$Ax + By + Cz + 1 = 0 \tag{15}$$

If (x, y, z) are chosen to be the closest points in the object's planes to the origin, the dual set $\mathcal{D}$ can be expressed in terms of the EGI and a support vector $\vec{h} \in \mathbb{R}^{|F|\times 1}$. The support vector is the perpendicular distance of each facet's coincident plane to the origin.

$$\mathcal{D} = \frac{\vec{E}}{|\vec{E}|\vec{h}} \tag{16}$$

The object's vertices $\vec{v}$ are found by intersecting the faces defined by the dual set's convex hull. Each triplet of dual vertices $[\nu_i, \nu_j, \nu_k] \in \text{convhull}(\mathcal{D})$ solves for a single real vertex:

$$v = \begin{bmatrix}\nu_i & \nu_j & \nu_k\end{bmatrix}^{-1} \begin{bmatrix}1\\1\\1\end{bmatrix}. \tag{17}$$

Convex face adjacency information is found by triangulating the convex hull of all recovered vertices. The accuracy of the recovered geometry is dependent on the correctness of the support vector $\vec{h}$ used to produce the dual set. Finding the true support vector is the challenge of the final optimization problem in direct convex shape inversion.

Support Vector Optimization

Prior work by Fan used Little's objective function for support vector optimization.[4,40]

$$f(\vec{h})_{\text{Little}} = \vec{h} \cdot \vec{a} \tag{18}$$

The support optimization problem is expressed with a hyperplane constraint to hold the mixed volume of the polytope constant to reconstruct the convex object corresponding to the optimized EGI $\vec{E}_{\text{opt}}$.[4]

$$\min_{\vec{h}} f(\vec{h})_{\text{Little}} \text{ subject to } \vec{h} \cdot \|\vec{E}_{\text{opt}}\| = \text{const.} \tag{19}$$

Initial conditions for the support vector is set to $\vec{h}_0 = [1, ..., 1]^T$ to ensure that all faces have non-zero area in the resulting reconstruction. Minimizing this objective function is linear but can produce scaling errors in the reconstruction as noted by both Fan and Little.[4,40] Little's objective functions was adapted via programming duality by Gardner et al.[44] yielding improved performance with similar drawbacks. Generally, if a support is reduced too far with respect to its neighbors, its face is absorbed underneath the convex hull and will have no corresponding reconstructed EGI vector. This issue is not tackled by Little or Gardner's schemes, and generally requires all attempted steps that change the face count to be discarded in favor of a smaller step.

This work improves on this step through a modification of an early method by Ikeuchi et al.[32] by preconditioning gradients with a Laplacian term from Nicolet et al.[34] Ikeuchi's method proposes a gradient descent scheme where the object is first reconstructed from the unit supports. The method then uses the objective function $f(\vec{h})_{\text{Ikeuchi}}$ in place of that in Eq. 18 to compute the area error in the reconstructed object. We denote the reconstructed EGI as $\vec{E}_{\text{rec}}$ and the reference EGI we seek to construct $\vec{E}_{\text{ref}}$. This objective function is convex with respect to the areas of the reconstructed EGI, ensuring a global minimum of $f(\vec{h}) = 0$ for correctly chosen supports.

$$f(\vec{h})_{\text{Ikeuchi}} = \sum_{i\in|\vec{E}_{\text{rec}}|} \left(\|\vec{E}_{\text{rec},i}\| - \|\vec{E}_{\text{ref},i}\|\right)^2 \tag{20}$$

Using Ikeuchi's objective function, we may simply solve an unconstrained and convex — yet still highly nonlinear — minimization problem for the correct supports.

$$\min_{h} f(\vec{h})_{\text{Ikeuchi}} \tag{21}$$

Each iteration updates the support vector by computing its gradient ∇f via finite differencing with step size η.

$$h \longleftarrow h - \eta \, \nabla f(\vec{h}) \tag{22}$$

The mesh-blind method using Eq. 20 in combination with Eq. 22 is functional, but leads to slow convergence and bad coordination between nearby faces. The coordination problem stems from the fact that the objective function gradient with respect to a single support may not capture the true global gradient in that component due to coupling with adjacent faces. Locally, it may minimize the objective function for a face to move outwards, increasing its support, when optimally all neighboring faces would move inwards together. Nicolet et al. propose the preconditioning term $(I + \lambda \mathcal{L})^{-p}$ based on the cotangent Laplacian matrix $\mathcal{L}$ which proves to be effective for this optimization, yielding the iterative update:

$$h \longleftarrow h - \eta (I + \lambda \mathcal{L})^{-p} \, \nabla f(\vec{h}) \text{ for } \lambda > 1, p \geq 1. \tag{23}$$

The discrete mesh Laplacian with cotangent weights is a ubiquitous tool in geometry processing for mesh augmentation and optimization.[45,46] Wardetzky et al. expand on the weights of this Laplacian in.[46] We compute the cotangent Laplacian for the dual set convex hull so that the gradients of nearby faces become increasingly coupled as their normal vectors coincide. This preconditioning strategy has the effect of diffusing gradients over nearby normal vectors, promoting cooperation between neighboring faces for faster convergence.

We propose an additional improvement over Ikeuchi's method by altering the choice of initial supports. Instead of naïvely choosing $\vec{h}_0 = [1, 1, ..., 1]^T$, knowledge of the estimated merged EGI enables us to more accurately initialize:

$$\vec{h}_0 = \sqrt{\frac{|\vec{E}_{\text{opt}}|}{4\pi}}. \tag{24}$$

Eq. 24 sets the support of each facet to the radius of the sphere with surface area equal to the total EGI area. This avoids unnecessary iterations for objects with supports much larger or smaller than unity while still ensuring that all facets will have nonzero area in the reconstruction.

CONVEX OBJECT RECONSTRUCTION RESULTS

Figure 8 displays the support vector optimization convergence for a variety of preconditioning levels. The EGI used for this study is $m = 50$ randomly sampled unit vectors on the sphere, assigned randomly distributed areas $a_i \in [0, 1]$. The control case with no preconditioning converges slower rate than all other cases. Convergence is generally fastest for $\lambda = 1$, $p = 3$, although the optimal p is a function of the input EGI.

Results from example inversion scenarios are shown in Figure 9. For each truth object, $n = 500$ light curve measurements are simulated from an initial angular velocity and orientation. The attitude profile of the object is integrated with Euler's equations of motion for a rigid body in a torque-free environment. We choose an arbitrary inertially fixed observer vector with a Sun vector slowly rotating to vary the solar phase angle. Each convex object is faithfully reconstructed and scaled; the truth object used to produce the synthetic light curve is recovered from that light curve and attitude profile alone. Some finer details lost for the cylinder and beveled rectangular prism.

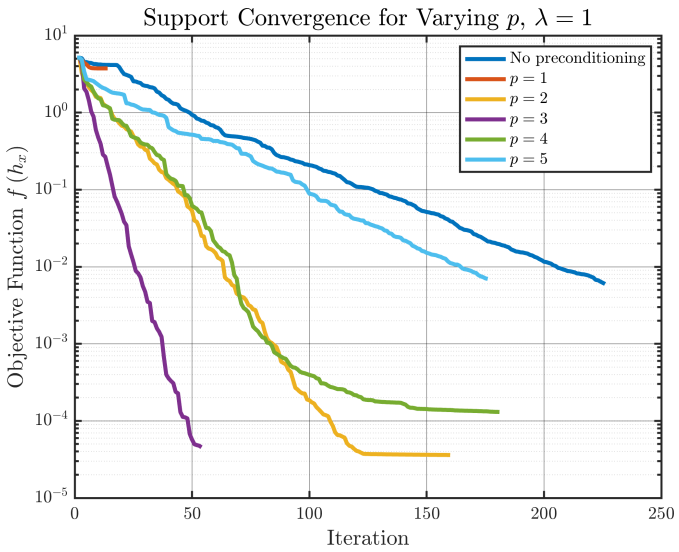

Figure 8. Ikeuchi objective function convergence for varying levels of preconditioning

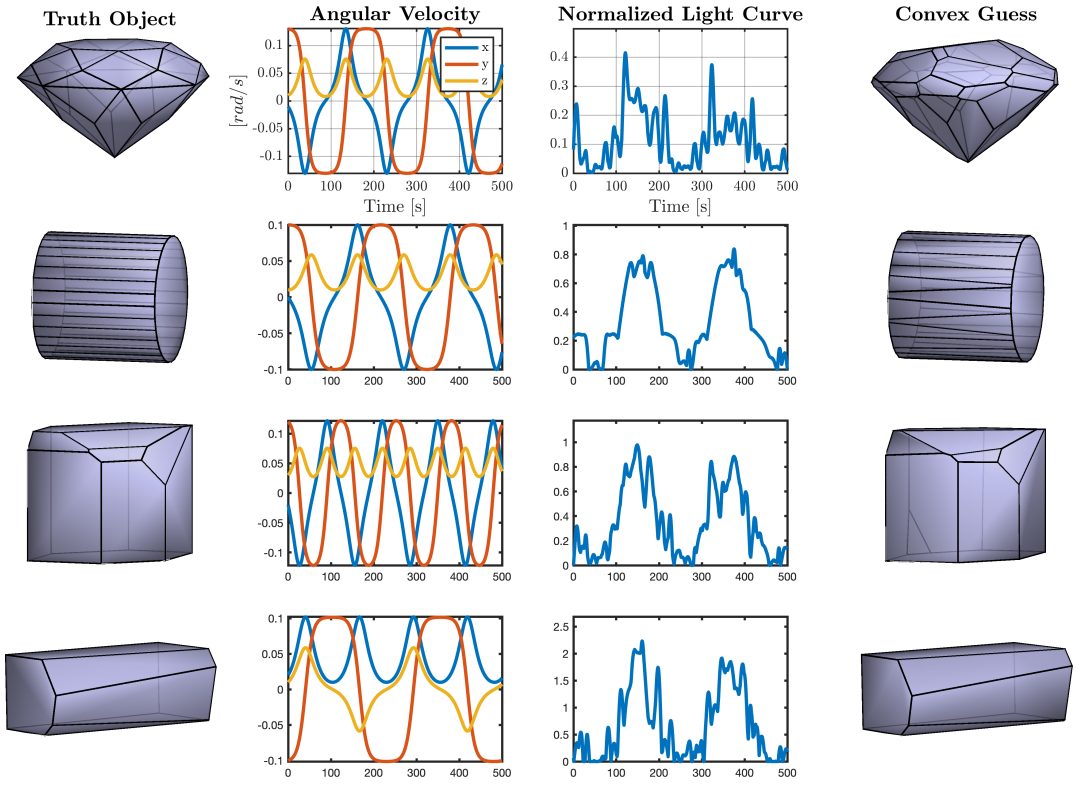

Figure 9. Convex shape inversion examples

NON-CONVEX FEATURE INVERSION

Non-Convex Feature Detection and Location

Many human-made space objects are, as highlighted in Figure 2, highly non-convex. As a result, their shape inversion is plagued by the fact that the Minkowski problem-driven reconstruction methods of Eq. 19

and Eq. 21 cannot recover non-convex features. Instead of beginning from the ground up, we can leverage the convex shape guess to detect and locate concavities, if they are present.

We can retain information about large, unilateral object concavities during EGI estimation in Eq. 8 by relaxing the EGI closure constraint. This unconstrained form is also generally functional for most convex objects and can be used without loss of detail in the final reconstruction as long as closure correction in Eq. 13 is still employed.

By measuring the divergence of the optimized EGI from a closed object with the magnitude of the closure error $\vec{e}_{EGI}$, we can determine the mean axis of prominent concave features.

$$\vec{e}_{EGI} = -\sum_{i=1}^{m} a_i \hat{n}_i. \tag{25}$$

This EGI closure error vector represents the missing area on each body axis that could be added to close the object. The addition of the minus sign transforms the vector from expressing the presence of excess area to the absence of missing area. The closure error will be negligable if there are no concavities present. The closure error may also be negligable if there is no self-shadowing is present over the sampled attitude profile, therefore the closure error merely quantifies the self-shadowing that is occuring, not whether there may be self-shadowing in other orientations.

Under the strong assumption that the concavities present are major and unilateral, this EGI error vector points along the mean axis of the concavity.

After locating the concave feature through the direction of the EGI error vector, the magnitude of the same vector is used to recover a more accurate non-convex guess for the object geometry. We have found that the ℓ^2-norm of the EGI error vector — the total missing area required to close the object — scales quadratically with object scale. A quadratic relationship is expected as geometrically scaling vertex positions by a factor c increases object area by a factor c^2, leading to an identical light curve and estimated EGI with c^2 as much area assigned to each facet, scaling $\vec{e}_{EGI}$ identically.

It can be shown empirically that for simple, unilateral concave features, the internal angle ψ between shadowing faces scales linearly with the quantity $\sqrt{\frac{\|\vec{e}_{EGI}\|}{\|\vec{E}_m\|}}$ where $\vec{E}_m$ is the estimated EGI after merging. We can estimate the internal angle as a function of the optimized EGI, its error, and an unknown slope c.

$$\psi_{\text{est}} = \pi - c\sqrt{\frac{\|\vec{e}_{EGI}\|}{\|\vec{E}_m\|}} \tag{26}$$

Eq. 26 diverges from the true internal angle for high aspect ratio objects and is therefore not entirely robust. We hope to remedy this with a more reliable approximation in future work. This relationship is displayed in Figure 10 for two different object geometries, each with prominent and unilateral concavities.

Concavity Location Results

The slope c has been shown through simulation to be independent of object geometry, with $5 \leq c \leq 8$ being accurate for a majority of simulated objects with large and unilateral concavities. Operators should choose smaller values of c for more conservative, smaller concavities and larger values for more pronounced — potentially overestimated — concavities. This solution is not unique,[30] and is best interpreted as finding the simplest non-convex object that would result in the same EGI closure error vector.

Concavity Creation

Our process for creating an accurate concavity in the reconstructed convex guess proceeds in four major steps. The model is first subdivided to add more faces and vertices. Subdivided vertices are then classified by their proximity to the EGI error vector, indicating whether their positions should be updated. Boundary

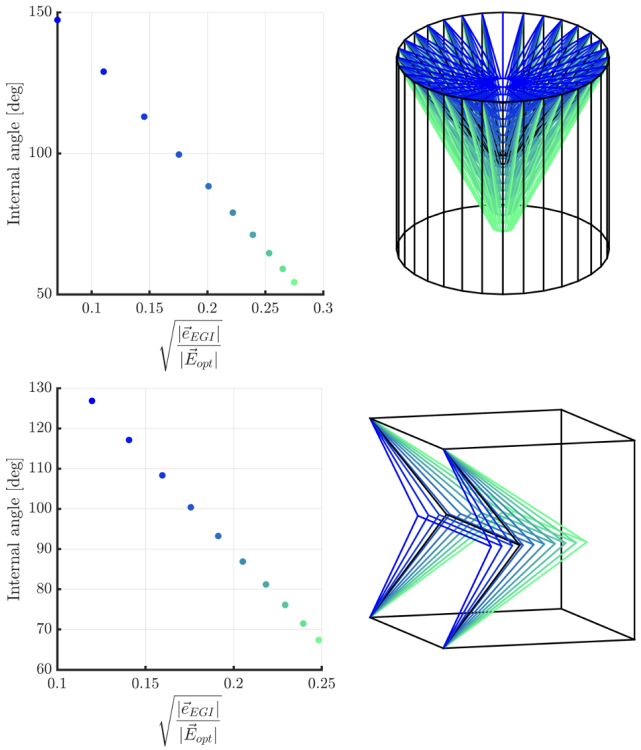

Figure 10. Concave cylinder and house EGI error relationship to internal angle

vertices are identified, and vertex positions are updated based on the estimated internal angle computed via Eq. 26.

Model Subdivision Subdividing the initial convex object guess is essential for retaining object detail during concavity creation. We use a combination of geometry processing algorithms for linear subdivision, Loop subdivision, and remeshing. Linear subdivision is advantageous when object faces are equally sized and boundary edges must be maintained. Loop subdivision is preferable when there are numerous vertices so that subdivisions do not drastically diverge from the initial boundary surface. Loop subdivision softens sharp edges as it relies on B-splines to interpolate new vertex positions.[47] The specific type and resolution of subdivision used depends on the level of detail the user needs to maintain in the introduced concavity, although linear subdivision followed by Loop subdivision is a useful baseline. Varying combinations of subdivision are shown in Figure 11 to illustrate the available configurations.

Vertex Classification When introducing a concavity, it is important to classify which vertices are likely part of the concave feature — and therefore need to be updated — and which vertices should remain unaffected. This is accomplished by measuring the angle from each face normal to the EGI error vector, where faces with normal vectors within an angle of $\pi/2$ to the error vector must be updated. In reality, all face normals and areas are impacted by the presence of the concavity in the area optimization Eq. 8 and EGI correction step Eq. 14. We select the angle defect $\pi/2$ to update all faces above the horizon from the EGI error vector, a bound which tends to produce visually accurate concavities. Faces requiring an update are termed *free* faces, with all others termed *root* faces.

Vertex Displacement For all vertices on free faces, we can further distinguish *root-adjacent* and *free* vertices. Root-adjacent vertices are part of at least one root face, whereas free vertices belong to only free faces. Classifying vertices in this way results in a border of root-adjacent vertices around the interior free vertices, visualized in Figure 12.

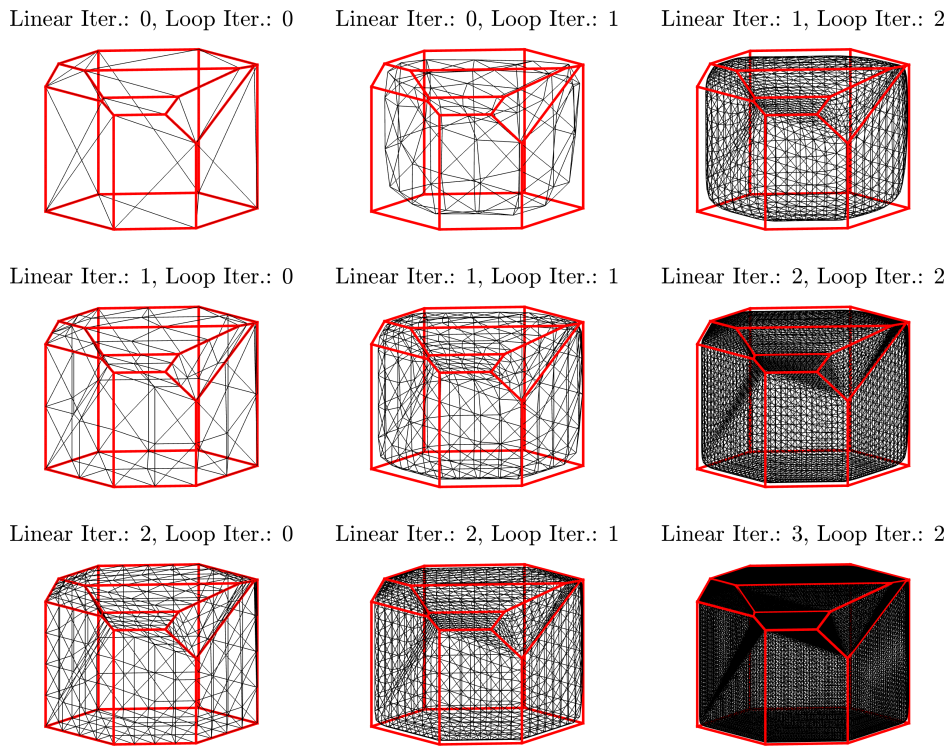

Figure 11. Subdivided object (black) with reference (red) with various levels of subdivision

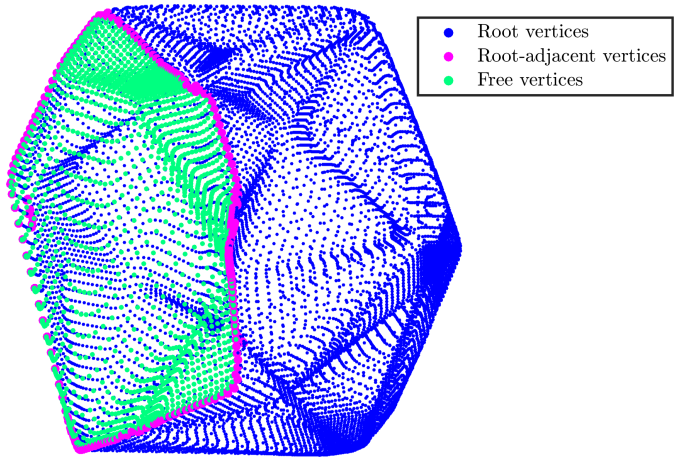

Figure 12. Root-adjacent and free vertices

Given the estimated internal angle ψ_{est} and the error vector $\hat{e}_{EGI}$, each ith free vertex is displaced to introduce a geometrically accurate concavity by moving each a distance d_i in the direction of $-\hat{e}_{EGI}$:

$$d_i = p_i \sqrt{\csc^2 \frac{\psi_{\text{est}}}{2} - 1}, \tag{27}$$

where p_i is the distance from each ith free vertex to the nearest root-adjacent vertex.

NON-CONVEX OBJECT RECONSTRUCTION RESULTS

Displacing free vertices in the EGI error vector direction by d_i yields accurate concavities for objects whose concave boundaries lie in a plane. The result of applying this process to a set of representative convex objects is shown in Figure 13 using the same attitude profiles and inertial Sun and observer vectors as in Figure 9.

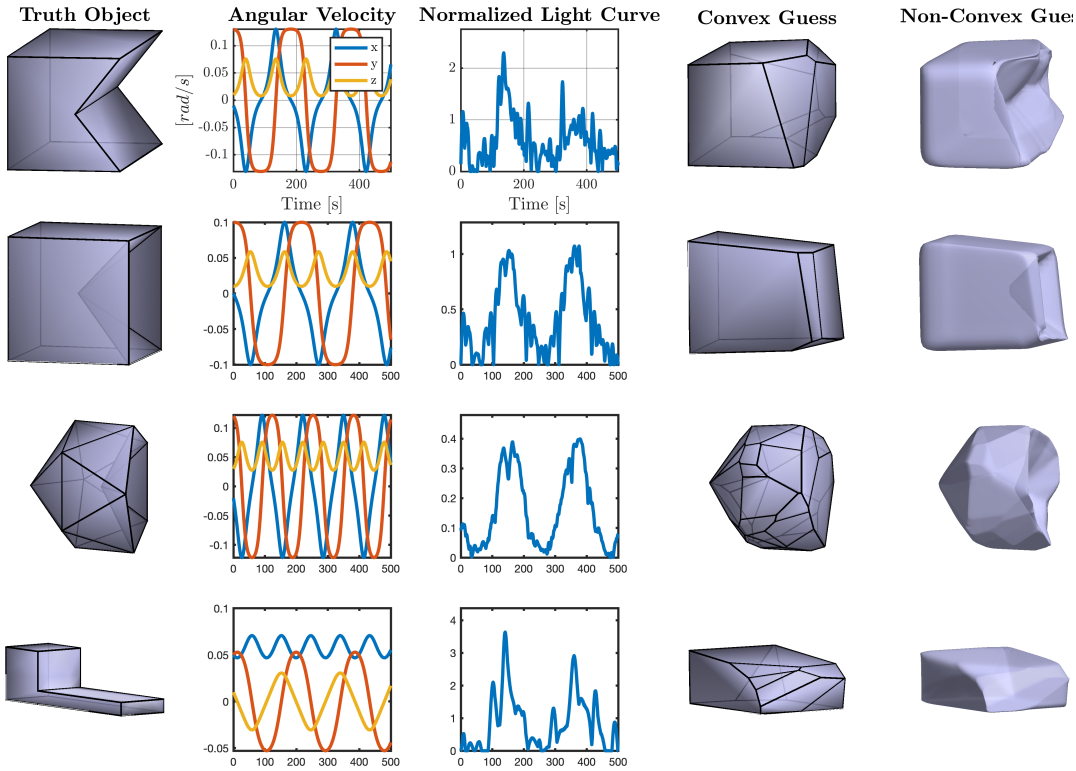

Figure 13. Collapsed house, cube, icosahedron, and box-wing satellite reconstructions using vertex displacement

The collapsed cube and icosahedron in Figure 13 are recovered effectively, but the collapsed house and box-wing satellite expose two limitations of the vertex displacement technique. In the case of the house where the concavity boundary is not constrained to a plane, the edges of the created concave feature are incorrect. The box-wing satellite's shadowing geometry leads the convex guess to be a poor approximation of the geometry outside of the concavity while also inheriting the same problem as the house.

This vertex displacement scheme will negligibly impact the convex guess if the truth object is also convex. A convex truth object will produce a small $\|\vec{e}_{EGI}\|$, causing the vertex update depth d_i to trend towards zero as the estimated internal angle approaches $\psi_{\text{est}} = 180°$. This is illustrated in Figure 14 using the same input convex objects and attitude profiles as in Figure 9.

Figure 14 clearly displays the compatibility of vertex displacement with truly convex objects. All objects are reconstructed faithfully in both their convex and non-convex inversions, with the same caveats noted in the discussion following Figure 9. Some truly sharp edges are rounded during mesh subdivision as seen in the gem or rectangular prism. That said, others like the cylinder become more accurate as subdivision reintroduces continuity lost to discretization in EGI merging.

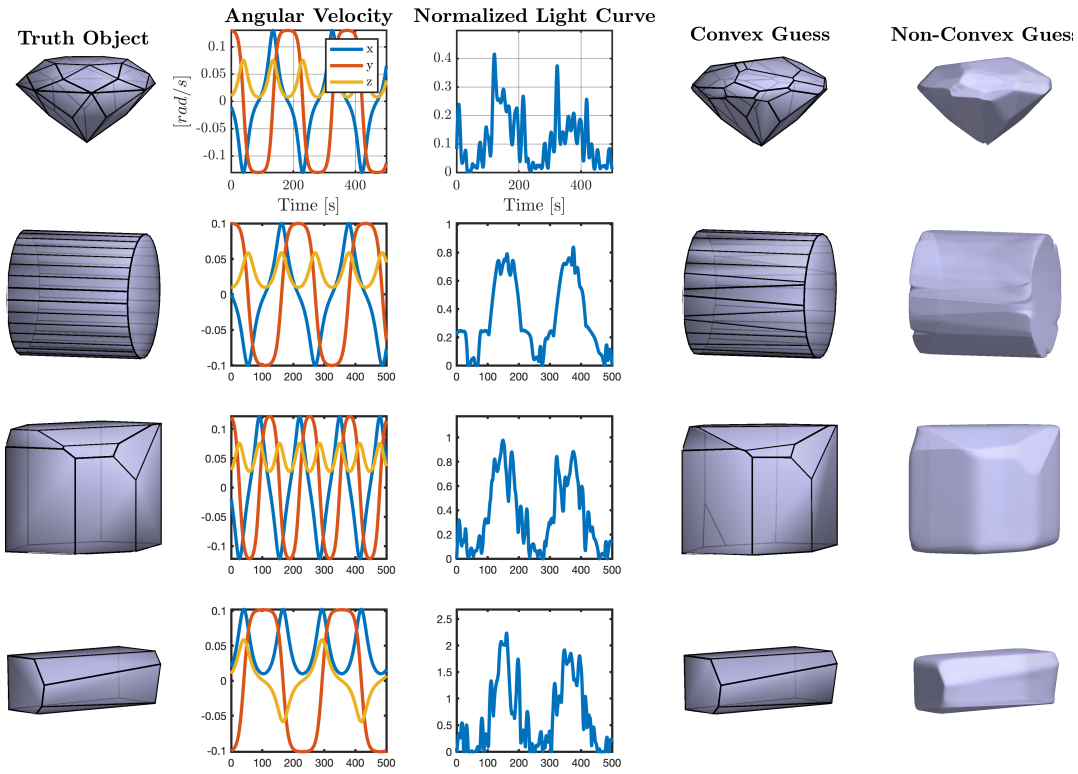

Figure 14. Convex objects under vertex displacement procedure

CONCLUSION

Characterization is an important capability for Space Domain Awareness. Light curves are an economical and information-dense measurement type that admits a wide array of characterization approaches.

In this paper, we present a variety of methods to improve and extend direct light curve shape inversion. All inversion methods must be built on the foundation of fast and physically accurate light curve simulations. We propose shadow mapping over facetwise ray tracing for rapid light curve simulation for non-convex objects, producing highly accurate shadow boundaries at low computational cost. For convex objects, the EGI resampling and merging procedures we introduce promote sparsity for more reliable and rapid reconstructions. As many human-made space objects have significant concavities, we derive a vertex displacement method for concavity creation using the EGI closure error vector. This procedure is shown to accurately recover simple, unilateral concavities if the concavity boundary lies in a plane. Our method is applicable for objects like rocket nozzles, but not box-wing satellites.

Satellite concavities pose a separate challenge to concave feature detection due to bilateral or mirror symmetry in shadowing. In these cases, the EGI error vector will account for multiple interfering shadowing sources, obscuring information about each in the process. Developing new methods to locate and quantify multiple independent concavity locations in the body frame will be a necessary step towards resolving the shape of such objects.

REFERENCES

[1] ESA Space Debris Office, "ESA's Annual Space Environment Report," tech. rep., European Space Agency, 04 2022.

[2] A. M. Friedman, *Observability Analysis for Space Situational Awareness*. PhD thesis, Purdue University, Apr 2020, 10.25394/PGS.12196863.v1.

[3] M. Kaasalainen and J. Torppa, "Optimization Methods for Asteroid Lightcurve Inversion: I. Shape Determination," *Icarus*, Vol. 153, No. 1, 2001, pp. 24–36, https://doi.org/10.1006/icar.2001.6673.

[4] S. Fan, *The Light Curve Simulation and Its Inversion Problem for Human-Made Space Objects*. PhD thesis, Purdue University, Aug 2020, 10.25394/PGS.12749570.v1.

[5] D. V. Cabrera, J. Utzmann, and R. Förstner, "Inversion of the shape of space debris from non-resolved optical measurements within SPOOK," *Proceedings of the 22nd Advanced Maui Optical and Space Surveillance Technologies Conference*, 2021, pp. 1–18.

[6] D. O. Fulcoly, K. I. Kalamaroff, and F. K. Chun, "Determining Basic Satellite Shape from Photometric Light Curves," *Journal of Spacecraft and Rockets*, Vol. 49, 2012, pp. 76–82.

[7] R. Linares, M. K. Jah, J. L. Crassidis, and C. K. Nebelecky, "Space Object Shape Characterization and Tracking Using Light Curve and Angles Data," *Journal of Guidance Control and Dynamics*, Vol. 37, 2014, pp. 13–25.

[8] R. Linares and J. Crassidis, "Space-Object Shape Inversion via Adaptive Hamiltonian Markov Chain Monte Carlo," *Journal of Guidance, Control, and Dynamics*, Vol. 41, 09 2017, pp. 1–12, 10.2514/1.G002296.

[9] S. Fan, C. Frueh, and A. Buzzoni, "A Light Curve Simulation of The Apollo Lunar Ascent Module," *AIAA/AAS Astrodynamics Specialist Conference*, 2016, pp. 1–10, 10.2514/6.2016-5504.

[10] D. Kobayashi and C. Frueh, "Compressed Sensing for Satellite Characterization," *Proceedings of the 20th AAS/AIAA Astrodynamics Specialist Conference*, 08 2020, pp. 1–20.

[11] C. Früh and M. K. Jah, "Coupled orbit attitude motion of high area-to-mass ratio (HAMR) objects including efficient self-shadowing," *Acta Astronautica*, Vol. 95, 2014, pp. 227–241, https://doi.org/10.1016/j.actaastro.2013.11.017.

[12] J. Allworth, L. Windrim, J. Wardman, D. Kucharski, J. Bennett, and M. Bryson, "Development of a High Fidelity Simulator for Generalised Photometric Based Space Object Classification using Machine Learning," *Proceedings of 70th International Astronautical Congress*, International Astronautical Congress, 2019, pp. 1–14, 10.48550/ARXIV.2004.12270.

[13] J. Allworth, L. Windrim, J. Bennett, and M. Bryson, "A transfer learning approach to space debris classification using observational light curve data," *Acta Astronautica*, Vol. 181, 01 2021, pp. 301–315, 10.1016/j.actaastro.2021.01.048.

[14] R. Furfaro, R. Linares, and V. Reddy, "Shape Identification of Space Objects via Light Curve Inversion Using Deep Learning Models," *Proceedings of the 20th Advanced Maui Optical and Space Surveillance Technologies Conference* (S. Ryan, ed.), Sept. 2019, p. 17.

[15] B. K. Bradley and P. Axelrad, "Lightcurve Inversion for Shape Estimation of GEO Objects From Space-Based Sensors," *Proceedings of the International Symposium on Space Flight Dynamics*, 2014, pp. 1–20.

[16] K. McNally, D. Ramirez, A. M. Anton, D. Smith, and J. Dick, "Artificial Intelligence For Space Resident Objects Characterisation With Lightcurves," *Proceedings of the 8th European Conference on Space Debris*, ESA Space Debris Office, 2021, pp. 1–12.

[17] L. D. J. Blacketer, *Attitude Characterisation of Space Objects using Optical Light Curves*. PhD thesis, University of Southampton, March 2022.

[18] M. Kaasalainen, J. Torppa, and K. Muinonen, "Optimization Methods for Asteroid Lightcurve Inversion: II. The Complete Inverse Problem," *Icarus*, Vol. 153, No. 1, 2001, pp. 37–51, https://doi.org/10.1006/icar.2001.6674.

[19] C.-K. Chng, M. Sasdelli, and T.-J. Chin, "Globally optimal shape and spin pole determination with lightcurve inversion," *Monthly Notices of the Royal Astronomical Society*, Vol. 513, 01 2022, pp. 311–332, 10.1093/mnras/stac198.

[20] B. Calef, J. Africano, B. Birge, D. Hall, and P. Kervin, "Photometric signature inversion," *Unconventional Imaging II* (V. L. Gamiz, P. S. Idell, and M. S. Strojnik, eds.), Vol. 6307, International Society for Optics and Photonics, SPIE, 2006, pp. 141 – 150, 10.1117/12.683015.

[21] S. Fan and C. Frueh, "A Direct Light Curve Inversion Scheme in the Presence of Measurement Noise," *The Journal of the Astronautical Sciences*, Vol. 67, 08 2019, 10.1007/s40295-019-00190-3.

[22] S. Fan and C. Frueh, "Multi-Hypothesis Light Curve Inversion Scheme for Convex Objects with Minimal Observations," *Proceedings of the 8th European Conference on Space Debris*, ESA Space Debris Office, 2021, pp. 1–7.

[23] A. M. Friedman and C. Frueh, "Observability of Light Curve Inversion for Shape and Feature Determination Exemplified by a Case Analysis," *Journal of the Astronautical Sciences*, Vol. 69, Apr. 2022, pp. 537–569, 10.1007/s40295-021-00293-w.

[24] R. Linares, M. Jah, and J. Crassidis, "Inactive space object shape estimation via astrometric and photometric data fusion," *Advances in the Astronautical Sciences*, Vol. 143, 01 2012, pp. 217–232.

[25] R. Linares and R. Furfaro, "Space Object Classification Using Deep Convolutional Neural Networks," *19th International Conference on Information Fusion*, 07 2016, pp. 1–8.

[26] E. Kerr, G. P. Elisabeth, P. Talon, and D. Petit, "Using AI to Analyse Light Curves for GEO Object Characterisation," *Proceedings of the 22nd Advanced Maui Optical and Space Surveillance Technologies Conference*, 2021, pp. 1–9.

[27] D. Hall, B. Calef, K. Knox, M. Bolden, and P. Kervin, "Separating Attitude and Shape Effects for Non-resolved Objects," *AMOS 2007 Proceedings*, 2007, pp. 1–12.

[28] T. Yanagisawa and H. Kurosaki, "Shape and motion estimate of LEO debris using light curves," *Advances in Space Research*, Vol. 50, No. 1, 2012, pp. 136–145, https://doi.org/10.1016/j.asr.2012.03.021.

[29] D. Kobayashi and C. Frueh, "Compressed Sensing for Satellite Characterization: Shadowing as a Sensing Matrix," *8th European Conference on Space Debris*, Vol. 8, 04 2021, 10.13140/RG.2.2.30685.33765.

[30] J. Ďurech and M. Kaasalainen, "Photometric signatures of highly nonconvex and binary asteroids," *Astronomy and Astrophysics*, Vol. 404, 06 2003, pp. 709–714, 10.1051/0004-6361:20030505.

[31] M. Viikinkoski, J. Hanuš, M. Kaasalainen, F. Marchis, and J. Ďurech, "Adaptive optics and lightcurve data of asteroids: twenty shape models and information content analysis," *Astronomy and Astrophysics*, Vol. 607, 11 2017, pp. 1–14, 10.1051/0004-6361/201731456.

[32] K. Ikeuchi, "Recognition of 3-D Objects Using the Extended Gaussian Image.," *IJCAI*, 1981, pp. 595–600.

[33] J. J. Little, "Extended Gaussian Images, Mixed Volumes, Shape Reconstruction," *Proceedings of the First Annual Symposium on Computational Geometry*, SCG '85, New York, NY, USA, Association for Computing Machinery, 1985, pp. 15–23, 10.1145/323233.323236.

[34] B. Nicolet, A. Jacobson, and W. Jakob, "Large Steps in Inverse Rendering of Geometry," *ACM Transactions on Graphics (Proceedings of SIGGRAPH Asia)*, Vol. 40, Dec. 2021, 10.1145/3478513.3480501.

[35] T. Möller and B. Trumbore, "Fast, Minimum Storage Ray-Triangle Intersection," *Journal of Graphics Tools*, Vol. 2, 08 2005, 10.1145/1198555.1198746.

[36] H. Kolivand and M. S. Sunar, "Survey of Shadow Volume Algorithms in Computer Graphics," *IETE Technical Review*, Vol. 30, No. 1, 2013, pp. 38–46, 10.4103/0256-4602.107338.

[37] W. Keeter, "NASA 3D Models," `https://nasa3d.arc.nasa.gov/models/`, February 2013. Accessed: 2022-04-27.

[38] S. Brabec, T. Annen, and H.-P. Seidel, "Practical Shadow Mapping," *Journal of Graphics Tools*, Vol. 7, No. 4, 2002, pp. 9–18.

[39] R. Santamaria, "raylib," `https://www.raylib.com`, November 2021. Accessed: 2022-04-28.

[40] J. J. Little, "An Iterative Method for Reconstructing Convex Polyhedra from Extended Gaussian Images," *Proceedings of the Third AAAI Conference on Artificial Intelligence*, AAAI'83, AAAI Press, 1983, pp. 247–250.

[41] H. Minkowski, *Allgemeine Lehrsätze über die konvexen Polyeder*, ch. 22, pp. 121–139. Springer Vienna, 1909.

[42] B. Keinert, M. Innmann, M. Sänger, and M. Stamminger, "Spherical fibonacci mapping," *ACM Transactions on Graphics*, Vol. 34, No. 6, 2015, pp. 1–7.

[43] E. W. Weisstein, "Sphere Point Picking," `https://mathworld.wolfram.com/SpherePointPicking.html`, 2002. Accessed: 2022-07-03.

[44] R. Gardner and P. Milanfar, "Reconstruction of Convex Bodies from Brightness Functions," *Discrete and Computational Geometry*, Vol. 29, 07 2003, pp. 279–303, 10.1007/s00454-002-0759-2.

[45] U. Pinkall and K. Polthier, "Computing Discrete Minimal Surfaces and Their Conjugates," *Experimental Mathematics*, Vol. 2, 11 1996, 10.1080/10586458.1993.10504266.

[46] M. Wardetzky, S. Mathur, F. Kälberer, and E. Grinspun, "Discrete laplace operators: no free lunch," *Proceedings of the fifth Eurographics symposium on Geometry processing*, 2007, pp. 1–5.

[47] C. T. Loop, *Smooth Subdivision Surfaces Based on Triangles*. PhD thesis, University of Utah, August 1987.